A NANOPARTICLE LASER PATTERNING PROCESS TO FABRICATE FLEXIBLE ELECTRONICS

A Dissertation
Presented to
The Academic Faculty

by

Ji-Hyeon Song

In Partial Fulfillment
of the Requirements for the Degree
Doctor of Philosophy in the
George W. Woodruff School of Mechanical Engineering

Georgia Institute of Technology
May 2019

A NANOPARTICLE LASER PATTERNING PROCESS TO FABRICATE FLEXIBLE ELECTRONICS

Approved by:

Dr. Yan Wang, Co-Advisor
School of Mechanical Engineering
Georgia Institute of Technology

Dr. Sung-Hoon Ahn, Co-Advisor
Department of Mechanical and Aerospace Engineering
Seoul National University

Dr. Shreyes Melkote
School of Mechanical Engineering
Georgia Institute of Technology

Dr. Seung Hwan Ko
Department of Mechanical and Aerospace Engineering
Seoul National University

Dr. Suresh Sitaraman
School of Mechanical Engineering
Georgia Institute of Technology

Dr. Doo-Man Chun
Mechanical Engineering
University of Ulsan

Date Approved: [December 13, 2018]

TABLE OF CONTENTS

LIST OF TABLES **v**

LIST OF FIGURES **vi**

SUMMARY **x**

CHAPTER 1. Introduction **1**

CHAPTER 2. Background **7**
2.1 Review on aerosol jet printing process **8**
2.2 Review on printing system with laser **18**
2.3 Review on models for particle deposition and laser effect **22**
2.4 Review on fabrication process for applications **27**

CHAPTER 3. System design and integration **30**
3.1 Process configuration **30**
3.1.1 Printing process 32
3.1.2 Cleaning process 37
3.2 Process design and integration **38**

CHAPTER 4. Performance evaluation and analysis **40**
4.1 Printed results **41**
4.2 Printing performance with different printing parameters **42**
4.2.1 Resolution 43
4.2.2 Adhesion test 45
4.2.3 Effect of SoD 47
4.3 Printing performance with different laser conditions **48**
4.3.1 Morphology 49
4.3.2 Composition 54
4.3.3 Particle recycle test 56
4.4 Process-structure-property relationship **58**
4.4.1 Electrical property 58
4.4.2 Mechanical property 67

CHAPTER 5. Process modeling and analysis **75**
5.1 An overview of the multiscale framework **76**
5.2 Deposition mechanism **79**
5.2.1 Classical particle impact and bonding model 79
5.2.2 Temperature change of particles- Model of nanoparticle heated by laser 82
5.2.3 Mechanical properties of particles – Molecular dynamics model 86
5.2.4 Temperature change of substrate 95
5.2.5 Mechanical properties of substrate 97
5.2.6 Prediction of the deposition 98

5.2.7 Sensitivity analysis 102
5.2.8 Validation of the model 104
5.3 Morphology– cKMC model 107
5.3.1 Controlled kinetic Monte Carlo 107
5.3.2 cKMC model of the printing system 110
5.3.3 Simulation results 118
5.3.4 Validation 119

CHAPTER 6. Applications 124
6.1 Hydrophobic/Hydrophilic surface 125
6.2 Kirigami flexible/stretchable electronics 127
6.3 Conductive line integrated strain sensor 131

CHAPTER 7. Conclusion 136

REFERENCES 141

LIST OF TABLES

Table 1. Comparison of low temperature particle printing systems 16
Table 2. Comparison between laser based printing methods [43] 20
Table 3. Laser conditions 36
Table 4. Comparison of cleaning methods 37
Table 5. Energy loss of laser beam 39
Table 6. Selected examples of the resistivity of conductive copper electrode fabricated with various methods [142] 72
Table 7. MD results of particle's mechanical properties with different temperature conditions 89
Table 8. MD results of particle's mechanical properties with different particle size 90
Table 9. Experimental results of copper mechanical properties of nanocrystalline metal from literature [148, 149] 91
Table 10. Temperature dependent mechanical properties of PET film [153] 97
Table 11. Experimental results of deposition with different particle sizes and laser conditions 106
Table 12. Example events in FIB lithography process [155] 109

LIST OF FIGURES

Figure 1. State-of-Art of flexible electronics 2
Figure 2. Selected techniques for microscale direct printing [7] 4
Figure 3. Schematic diagram of ADM process [17] 9
Figure 4. Schematic diagram of CS process [22] 9
Figure 5. Fabrication envelop of low temperature particle deposition system [27] 11
Figure 6. Selected deposition results of NPDS [28] 11
Figure 7. System configuration of NPDS [27] 12
Figure 8. System configuration of direct laser assisted nanoparticle deposition system [43] 13
Figure 9. System configuration of indirect laser assisted nanoparticle deposition system [43] 13
Figure 10. Hardware schematic of the AFN printing [7] 14
Figure 11. History of low temperature deposition processes using particle [27] 15
Figure 12. Process envelop for low temperature particle direct printing processes 17
Figure 13. Schematic diagram of (a) selective laser sintering, (b) laser based deposition, and (c) laser engineered net shaping [46-48] 20
Figure 14. Simulation with nanomaterials across different scales [75] 24
Figure 15. Review on the researches of strain sensors [137] 29
Figure 16. The process sequence of NLP process 31
Figure 17. System configuration of NLP process 33
Figure 18. CAD model of chamber, nozzle, substrate holder and stage 34
Figure 19. CAD model of how substrate moves 34
Figure 20. Absorption coefficient of silver and copper particles 36
Figure 21. Cleaning methods for area without laser irradiation 37
Figure 22. Hardware setup of NLP process 38
Figure 23. Measured point of laser beam power 39
Figure 24. SEM image of raw (a) copper and (b) silver particles 41
Figure 25. Printed result of various patterns printed with copper particles on paper and PET substrate 42
Figure 26. Line width with respect to stage feed rate and laser scan speed on PET substrate 44
Figure 27. Line width with respect to stage feed rate and laser scan speed on paper substrate 44
Figure 28. Optical images and confocal result of adjacent lines 45
Figure 29. Adhesion test of printed results: Before detachment 46
Figure 30. Adhesion test of printed results: After twice of detachment tests 46
Figure 31. Experimental setup for direct printing on curved surface 47
Figure 32. Schematic diagram of direct printing on curved surface 48
Figure 33. Deposition results 48
Figure 34. SEM image of copper patterns surface 49
Figure 35. SEM image of copper patterns, cross section and surface image with different laser conditions 51

Figure 36. Optical and thermal penetration depth [139] 52
Figure 37. Calculation of laser irradiation number 53
Figure 38. Thickness changes with respect to laser energy density 53
Figure 39. SEM image of cross section in depth direction 54
Figure 40. XRD results of printed copper patterns with different laser conditions, (a) 0.31, (b) 0.76, (c) 1.40, (d) 2.62, and (e) 5.86 J/cm^2 55
Figure 41. XRD results of recycled particles with different laser conditions (a) Raw particle, (b) 0 J/cm^2, (c) 1.40 J/cm^2, (d) 2.62 J/cm^2, and (e) 5.86 J/cm^2 57
Figure 42. Cross section geometry of silver conductive line 59
Figure 43. Resistivity with different laser energy densities 59
Figure 44. Hardware setup for bending test 61
Figure 45. Bending test with 4 terminal sensing 61
Figure 46. Normalized resistance with different radius of curvatures 62
Figure 47. Bending test of different bending directions 63
Figure 48. Normalized resistance with different bending directions 63
Figure 49. Experiment setup for folding test 65
Figure 50. Folding test results: Outer folding 65
Figure 51. Folding test results: Inner folding 65
Figure 52. Folding repeat test: High laser power, outer folding 66
Figure 53. Folding repeat test: High laser power, inner folding 66
Figure 54. Cycle test 68
Figure 55. Strain with bending 68
Figure 56. SEM image of crack after 100 bending test 69
Figure 57. Resistance change with loading and crack initiation 70
Figure 58. Gauge factor with number of bending 70
Figure 59. The proposed multiscale adhesion model 77
Figure 60. Process flow for deposition mechanism model 78
Figure 61. Particle impact model for deposition 80
Figure 62. Absorption coefficient of copper particles 84
Figure 63. DSC results of (a) 5 μm and (b) 0.1 μm copper particles 85
Figure 64. Estimation of copper particle temperature with different laser conditions 85
Figure 65. (a) Single crystalline and (b) polycrystalline structure 87
Figure 66. Polycrystalline copper particle before and after uniaxial tension 87
Figure 67. Stress-strain curve of single crystalline and poly crystalline copper particle . 87
Figure 68. Stress-strain curve of different temperature of copper particle (particle diameter: 100nm) 89
Figure 69. Stress-strain curve of different size of copper particle (particle temperature: 300 K) 90
Figure 70. Simulated properties of copper nanoparticles by MD model [150] 92
Figure 71. Hall-Petch relationship for copper by several studies [151] 93
Figure 72. Effect of grain size on mechanical properties (particle diameter: 100 nm) 94
Figure 73. Effect of defects on mechanical properties (a) MD model and (b) real particle 94
Figure 74. IR camera (CX 320, COX) image with laser irradiation 95
Figure 75. Temperature change with regard to time 95
Figure 76. Temperature change with regard to laser power level 96

Figure 77. Adhesion condition without laser irradiation 100
Figure 78. Adhesion condition with laser irradiation of 400 mW 100
Figure 79. Projected radius of (a) elastic impact and (b) plastic-elastic impact [154] ... 101
Figure 80. Relationship between elastic yield limit and radius of plastic deformation .. 101
Figure 81. Sensitivity analysis of particle substrate adhesion: particle speed 102
Figure 82. Sensitivity analysis of particle substrate adhesion: Young's modulus 103
Figure 83. Sensitivity analysis of particle substrate adhesion: substrate temperature 103
Figure 84. SEM image of the (a) < 100 nm, (b) 0.5~1.5 μm, and (c) 3.25~5 μm sized copper particles 104
Figure 85. Printing results of different sized particles before cleaning process 105
Figure 86. Printing results of different sized particles after cleaning process 105
Figure 87. Optical image of the printing under condition (a) 0.5~1.5 μm, 1 bar, 5.86 J/cm^2, (b) 0.5~1.5 μm, 2 bar, 5.86 J/cm^2, (c) 3.25~5 μm, 1 bar, 5.86 J/cm^2, and (d) 3.25~5 μm, 2 bar, 5.86 J/cm^2 106
Figure 88. cKMC models for FIB [155] 109
Figure 89. System configuration of the LI-NPDS process modeled by cKMC [45] 110
Figure 90. Effect of laser power on size of clustered Al_2O_3 nanoparticles. [44] 112
Figure 91. Comparison of results with different laser treatment methods. (a) particles that are in steady state and (b) particles with kinetic energy moving along aerosol flow [45] 112
Figure 92. Examples of diffusion, laser treatment, and deposition events. (a) diffusion, (b) laser treatment, and (c) deposition events [45] 114
Figure 93. Illustrations of laser treatment and deposition with different laser power levels. (a) laser treatment and (b) deposition events [45] 114
Figure 94. Sensitivity analysis for (a) reverse rate and (b) deposition rate [45] 117
Figure 95. Cross section image of deposited film with (a) 0 mW and (b) 200 mW laser power for thickness analysis [45] 117
Figure 96. Image processing process for porosity analysis [45] 117
Figure 97. Visualization of the simulation result including (a) the complete system and (b) substrate [45] 119
Figure 98. Simulation and experimental results: Change of thickness of Al_2O_3 deposition layer with respect to laser power [45] 120
Figure 99. Simulation and experimental results: Change of porosity on Al_2O_3 deposition layer regarding to laser power [45] 120
Figure 100. GPR model for discrepancy [45] 123
Figure 101. Copper patterns on PET substrate (400, 100 μm) 125
Figure 102. Contact angle measurement system 125
Figure 103. Contact angle difference with regard to laser power and pattern size 127
Figure 104. Fabrication process for kirigami flexible/stretchable electronics (a) cut in the same side and (b) cut in the opposite side 128
Figure 105. Conductivity test of fabricated electronics using kirigami of paper with (a) bending and (b) stretching 130
Figure 106. Illustration of the deformation in (a) bending and (b) stretching motion 130
Figure 107. Unstable soldering issue near the bending area 132
Figure 108. Conductive line integrated strain sensor 133

Figure 109. Bending test of (a) strain sensor and (b) conductive line integrated strain sensor 133
Figure 110. Change of normalized resistance with bending in strain sensor and conductive line integrated strain sensor 134
Figure 111. Printed strain gauge pattern with the NLP process 134

SUMMARY

Flexible electronics are attractive for new applications because of their flexible forms as well as properties of light weight and portability. The circuits are usually printed on flexible substrates such as plastic, fabric, and paper, which are delicate and heat sensitive. Traditional photolithography with the use of high temperature and corrosive chemicals is not suitable for flexible substrates. The fabrication of flexible electronics requires fast and low-temperature printing processes in order to minimize the damage of the flexible substrates.

In this research, a high-throughput nanoparticle laser patterning process for flexible electronics is developed, where nanoparticles are sintered with low power laser while they are selectively deposited to enhance printing quality. Copper and silver particles are successfully deposited on paper and polyethylene terephthalate (PET) substrates. To study the process-structure-property relationship, the effects of process parameters on the deposition performance are assessed. The thermal effect of laser on the morphology and porosity of films is observed under scanning electron microscope. Chemical composition of printed pattern is also characterized using X-ray diffractometer. The sensitivity of electromechanical property with respect to the porosities, as a result of different laser power densities, is analyzed. In theoretical studies, a multiscale model of deposition mechanism is developed, where an analytical adhesion model predicts the deposition performance based on laser irradiation, particle size, temperature, elastic-plastic properties of particle and substrate, and deposition velocity. The mechanical properties of nanoparticles are predicted by molecular dynamics simulation to construct the structure-property linkage at

nanoscale. A controlled kinetic Monte Carlo simulation model is applied to build process-structure relationship to predict the morphologies of the printing results at mesoscale. The developed process is demonstrated and applied to fabricate hydrophobic and hydrophilic patterns with controlled oxidation levels on PET substrate, and flexible electronics on PET and paper substrate.

CHAPTER 1. INTRODUCTION

Flexible electronics are attractive for next-generation electronic products because of their flexible forms as well as properties of light weight and portability. With the ability to conform, bend or roll into any shape, flexible electronics have various industrial and medical applications such as electronic paper, rollable display, flexible mobile device, implantable sensor, etc. Despite the great potentials, flexible electronics are still confined to lab level experiments till today because of their poor durability. Crack within the printed circuit and weak bonding between the prints and substrate can cause detachment and delamination. Therefore, the fabrication of flexible electronics imposes new challenges on manufacturing processes. Figure 1 shows the state-of-the-art of flexible electronics fabricated with different processes. Flexible electronics are usually printed with the roll to roll, inkjet printing, or soft lithography processes.

Traditional photolithography can print high-resolution patterns and circuits with a small feature size. However, its use of high temperature and corrosive chemicals is not suitable for flexible substrates. Flexible substrates such as plastic, fabric, and paper are delicate and heat sensitive. The fabrication of flexible electronics requires low temperature printing processes in order to minimize the damage of the flexible substrates. In addition, the photolithography process requires complex steps for the fabrication of mask, deposition, and etching, which makes the process expensive.

Inkjet printing	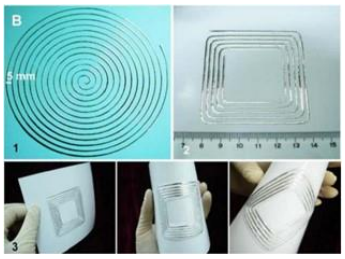	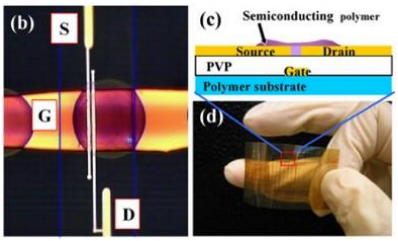
	(a) Functional components: inductance coil and radio-frequency identification antenna [1]	(b) Organic field-effect transistor on a polyimide substrate [2]
Photolitho-graphy	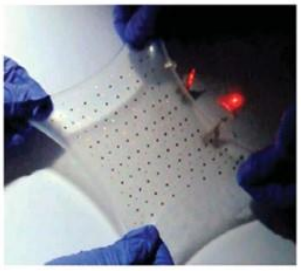	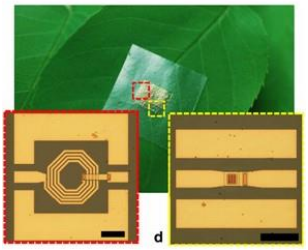
	(c) Stretchable lithium ion battery [3]	(d) Microwave passive elements and integrated circuit on cellulose nanofiber paper [4]
Etc.	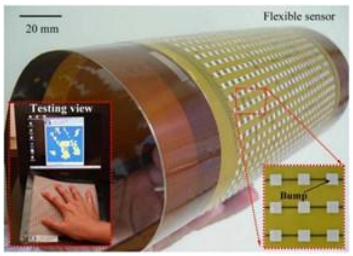	
	(e) Screen printed pressure sensors on large flexible polyimide films [5]	(f) Stretchable GaInSb antenna [6]

Figure 1. State-of-Art of flexible electronics

Direct writing technologies such as inkjet printing, direct pen writing, and screen printing avoid the need of masks as in the lithography. Figure 2 shows the available techniques for microscale direct printing [7]. Energy beam printing methods include focused ion beam (FIB), focused ion beam-chemical vapor deposition (FIB-CVD), and direct laser writing. These processes can print small features with high resolution. However,

the processes are complicated and expensive because high energy sources and a vacuum working environment are required. Physical contact methods include dip pen nano lithography, screen printing, gravure printing, and nano imprint. These processes are capable of fast and large scale printing. However, printed patterns can easily deteriorate, and substrate and tool damage often occurs. Liquid droplet methods such as ink-jet printing and electro-hydrodynamic jet printing can also print high resolution patterns. However, these processes have limitations such as clogging and limited feature sizes. The materials also need to be solvable to the chosen solvent, and suitable viscosity is required. Therefore the available material choice is limited. To avoid the use of solvent which is environmentally harmful and to broaden the range of material selection, research for printing dry particle deposition system has been conducted [8-10]. These methods can perform fast and large area printing with inexpensive and simple processes. Moreover, a wide selection of material type can be used. Despite the advantages, they have limitations in small feature printing with high resolution. Low durability of the print is the challenge that needs to be overcome. Among them, aerodynamically focused nanoparticle (AFN) printing allows to deposit various patterns in microscale [10]. However, the processing time is long, since the nozzle prints patterns serially, and the durability of prints is low because the structure has high porosity. Therefore, these processes also have limitations in printing flexible electronics.

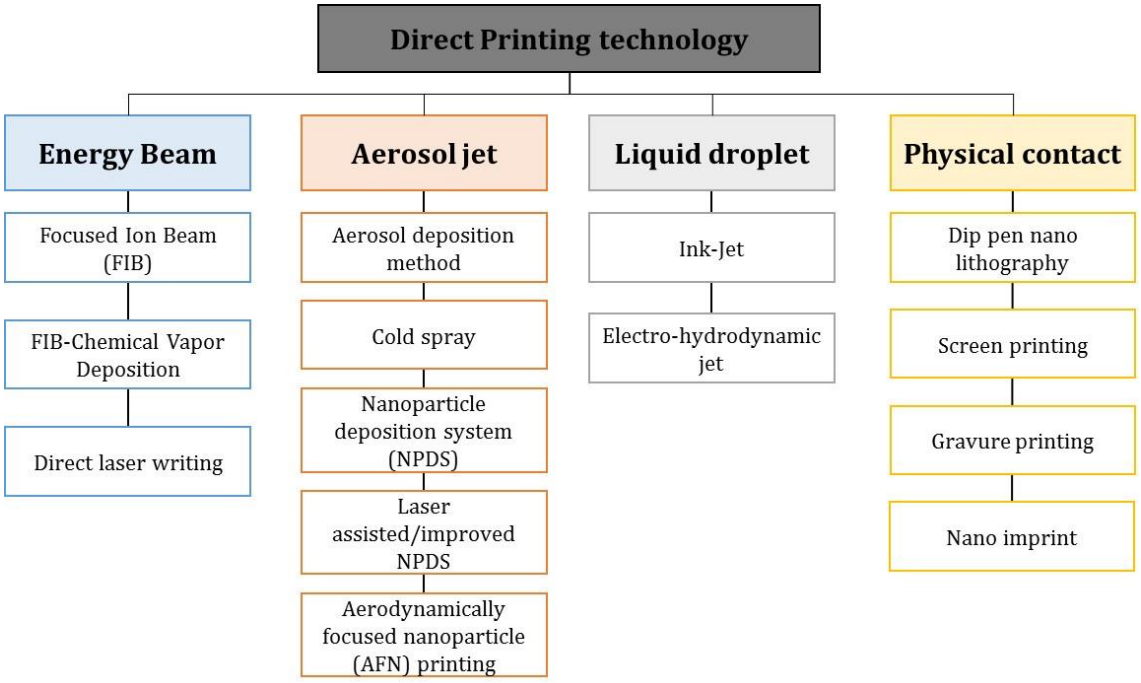

Figure 2. Selected techniques for microscale direct printing [7]

Auxiliary methods have been developed to enhance the performance of these direct writing processes. Especially, laser sintering is the most frequently used method to improve the performance of additive printing. For example, Chiolerio *et al.* [11] reported that inkjet printing combined with a laser system can improve the electrical properties of the printed silver lines. Ahn *et al.* [12] introduced laser in a nanoparticle deposition system to enhance the mechanical property of the deposited TiO_2 film. Likewise, there have been attempts to improve the deposition process with laser. The literature will be reviewed in detail in Section 2.2. However most of these processes have the issue of thermal damage. Since laser is either coaxially or eccentrically affecting the substrate directly, the use of high laser power increases the temperature of the substrate in heat affected zones. Damage is inevitable for flexible substrate which is vulnerable to heat. Therefore, developing manufacturing processes to print durable and high-performance flexible electronics with

low processing temperature is essential. In addition, there is an absence in the study of deposition mechanism with particle impact and heat annealing of low temperature. The lack of understanding of printing mechanisms as well as process-structure-property relationships makes the quality control difficult.

In this research, a nanoparticle laser patterning (NLP) process for high throughput direct writing of flexible electronics is developed. Nanoparticles are sintered with laser while they are selectively deposited. As a proof of concept, copper and silver particles were successfully deposited on paper and polyethylene terephthalate (PET) substrates. The use of low laser power, low aerosol pressure, and non-vacuum environment makes the proposed process a low-cost and large-area deposition method. Small particles around 100 nm are used so that laser energy could effectively transfer to particles, while thermal damage induced by laser system is minimized. With different laser conditions, porosity and chemical composition of the deposition can be controlled and localized, which could improve the performance of printed patterns.

To characterize the thermal effect of laser, chemical composition of particles has been analyzed using X-ray diffractometer (XRD). The extent of oxidation with different laser power levels is quantified. Electromechanical property is also analyzed for the purpose of sensing applications. It is shown that the property is sensitive to the porosity difference caused by different levels of laser irradiation. The microscopic images taken by scanning electron microscope (SEM) allow us to measure porosity after sintering. In nanomanufacturing, microstructural evolution and mechanical deformation mechanism are essential for elucidating physical phenomena [13]. Furthermore, process modeling and analysis expand the knowledge on the adhesion mechanism and process-structure-property

relationship for the hybrid process of direct printing and laser system. A multiscale adhesion model is developed to evaluate the impact of process parameters and understand the physical phenomenon. The deposition mechanism is modeled with an analytical model as well as molecular dynamics (MD) and controlled kinetic Monte Carlo (cKMC) simulations to understand the physics related to nanoparticles. The developed process has been used to fabricate novel patterns on flexible substrates such as hydrophobic and hydrophilic surfaces using different oxidation levels, kirigami electronics on papers, and durable strain sensors.

In the remainder of the dissertation, Chapter 2 provides the literature review of relevant work. Chapter 3 introduces system design and integration of the NLP process. In Chapter 4, performances of the printing are evaluated. The printing performances with different printing parameters as well as laser conditions are studied to build process-structure-property relationship. In Chapter 5, process modeling and analysis are provided. A multiscale model is developed to study deposition mechanism of the printing process. In addition, a cKMC model is built to analyze and predict the morphological changes in mesoscale. Chapter 6 introduces possible applications fabricated with the NLP process. Finally, in Chapter 7, conclusion including future works and contributions is addressed.

CHAPTER 2. BACKGROUND

This chapter provides the basic background information associated with printing processes including aerosol jet printing process and deposition process with laser. In addition, study on the model for deposition and laser effect on particles will be reviewed as well as applications with their fabrication methods. Aerosol jet printing processes including aerosol deposition method (ADM), cold spray (CS), and nanoparticle deposition system (NPDS), which have been developed and studied in the Innovative design and integrated manufacturing lab. (IDIM) in Seoul National University (SNU) since 2008, will be reviewed in Section 2.1. Auxiliary methods have been developed to enhance the performance of the deposition process as a hybrid approach [14]. Especially, laser sintering is the most frequently used method to improve the performance of additive nanomanufacturing. Both dry and wet deposition methods with laser process will be reviewed in Section 2.2. Furthermore, models for particle deposition will be reviewed. There are many researchers studying particle deposition by analytical and computational models. These will be reviewed in detail and their limitations will be discussed in Section 2.3. In addition, models of nanoparticles with laser treatment will be covered. In Section 2.4, applications developed with direct printing methods and their fabrication methods will be discussed.

2.1 Review on aerosol jet printing process

Nanoparticle deposition is an important additive nanomanufacturing process for thin film coating, which has been applied to lithium ion batteries, gas sensors, electrode, electronic devices, water splitting, dye sensitized solar cell, and others. Compared to other processes such as atomic layer deposition (ALD) or chemical vapor deposition (CVD) to produce thin films, direct nanoparticle deposition provides reduced process time. Well studied nanoparticle deposition processes are aerosol deposition method and cold spray deposition. Aerosol deposition method was first developed by Akedo *et al*. [15, 16] in the late 1990s. Figure 3 shows the schematic diagram of the process [17]. This process sprays aerosol of initial bulk particles at room temperature to produce ceramic films [18]. Successful depositions of ceramic particles such as Al_2O_3, TiO_2, $BaTiO_3$, and $Pb(Zr, Ti)O_3$ with few micrometers to tens of micrometers thickness were reported [19-21]. These films have been utilized as sensors, fuel cells, batteries, etc. [9].

Figure 4 shows the schematic diagram of cold spray process [22]. Cold spray process normally accelerates metal particles with supersonic velocity in a heated gas stream through converging-diverging nozzle [23]. When particles hit the substrate with high velocity, plastic deformation of the particle causes deposition. Metal particles such as Cu, Ti, Zn, and Al of typical diameter of 50 μm have been successfully coated. The temperature of heated gas is around 500°C which is under the particle melting point, therefore the deposition is in the solid state [24]. Thermally induced stress is lower than laser engineered net shaping process which completely melts the particles. This will be discussed in Section 2.2. In addition, because of low process temperature, compositions and phases of initial materials remain steady [13]. Cold spray coatings can be used in various industrial

applications. For example, copper coating can improve heat conductivity between electronic devices. Aluminum coating can be used as a corrosion protection, and stainless steel coating can protect the surface from wear and corrosion [25].

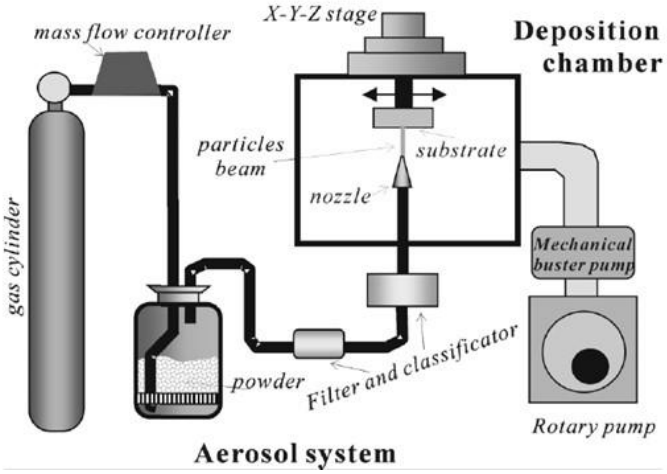

Figure 3. Schematic diagram of ADM process [17]

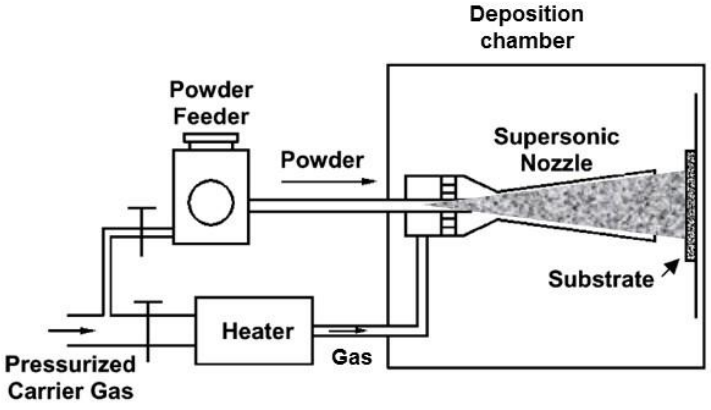

Figure 4. Schematic diagram of CS process [22]

Recently, a dry spray process which can deposit metal and ceramic particles at room temperature, called NPDS, was developed by Chun *et al*. [8, 26] in 2008. It is a solvent-free and direct printing process of inorganic nanoparticles. Figure 5 shows the fabrication envelop of low temperature particle deposition systems comparing cold spray method, aerosol deposition method, and NPDS [27]. ADM typically prints ceramic particles, whereas CS method normally prints metal particles. However, using higher velocity than ADM and using smaller diameter particle than CS method, multi-material deposition is available in NPDS. Figure 6 shows the selected deposition results of NPDS [28]. Ceramics, metals, or mixed particles can be deposited on ceramic, metal, or polymer substrate. For example, TiO_2, Al_2O_3 [29-31], and Ni particles [32, 33] were deposited. Multi-layer deposition was also studied [34]. Figure 7 shows the system configuration [27]. The NPDS system is composed of a compressor, particle feeder, nozzle, vacuum chamber, vacuum pump, and controller. Dry raw particles are stored in the particle feeder without any pre-treatment. Compressed air from the compressor carries particles to the nozzle. After passing the nozzle, the particles impact on the substrate and deposit because of a kinetic energy. This process is in a low vacuum and room temperature environment. Deposition mechanism has been investigated [35]. Computational fluid dynamics was used to study micro nozzle with supersonic particle deposition [36]. The deposited films were used for energy applications such as dye sensitized solar cell (DSSC) [12, 37, 38] and electrochromic window (ECW) [39-42].

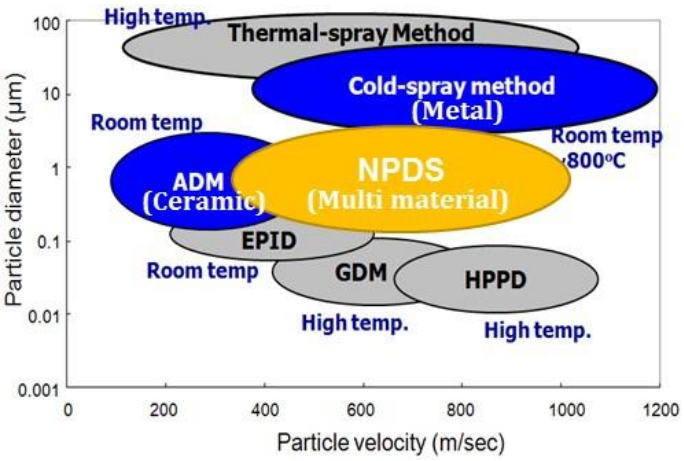

Figure 5. Fabrication envelop of low temperature particle deposition system [27]

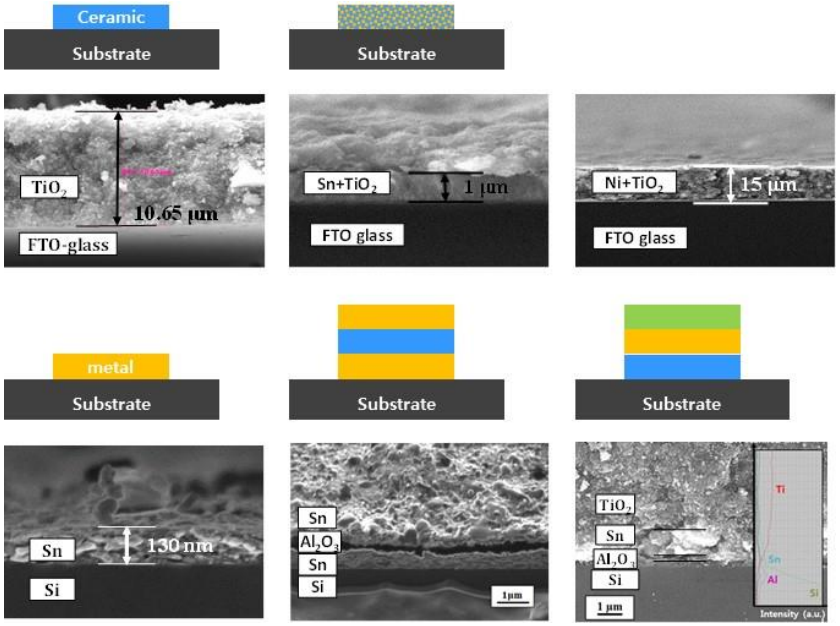

Figure 6. Selected deposition results of NPDS [28]

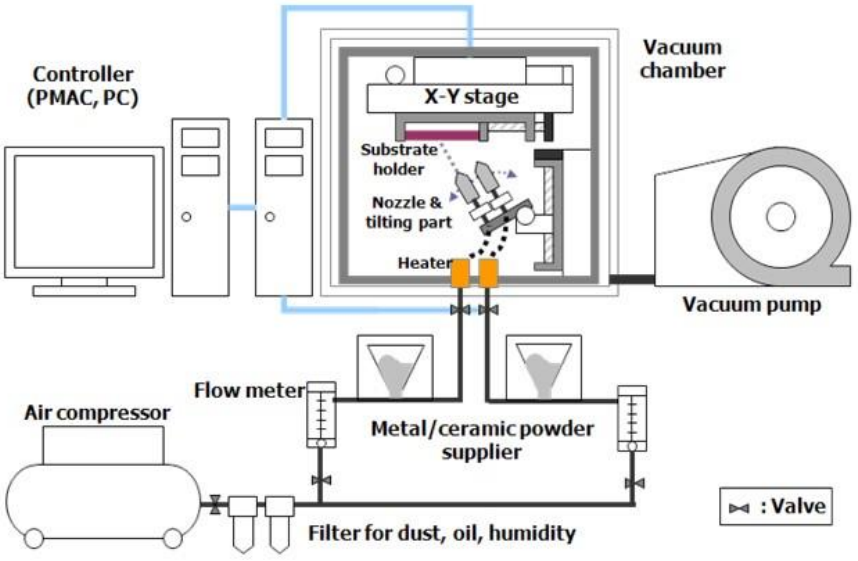

Figure 7. System configuration of NPDS [27]

The major challenges of NPDS process include low adhesion force, low density, and high surface roughness, which potentially lead to low quality and low durability of the films. Recently laser irradiation, as an auxiliary method to enhance the performance of the deposition process, was developed in the laser assisted nanoparticle deposition system (La-NPDS) [12]. Figure 8 shows the system configuration of La-NPDS [43]. In this system, laser is directly applied through the nozzle to the deposited particles to improve the particle bonding and adhesion with substrate using the sintering effect. The introduction of laser enables a broad range of materials to be deposited, which also increases the quality of the films. With laser irradiation, mechanical property and morphology of the deposited films can be improved. However, thermal damage on the substrate is inevitable with the direct irradiation method. Therefore, a new method for laser sintering was developed to solve this problem. Laser improved nanoparticle deposition system (LI-NPDS) uses indirect laser irradiation [44]. Figure 9 shows the system configuration of LI-NPDS [43]. Laser is applied

on the path of nanoparticles so that sintering occurs while particles are flying. While avoiding the substrate damage, morphology of the deposited film was improved [44, 45].

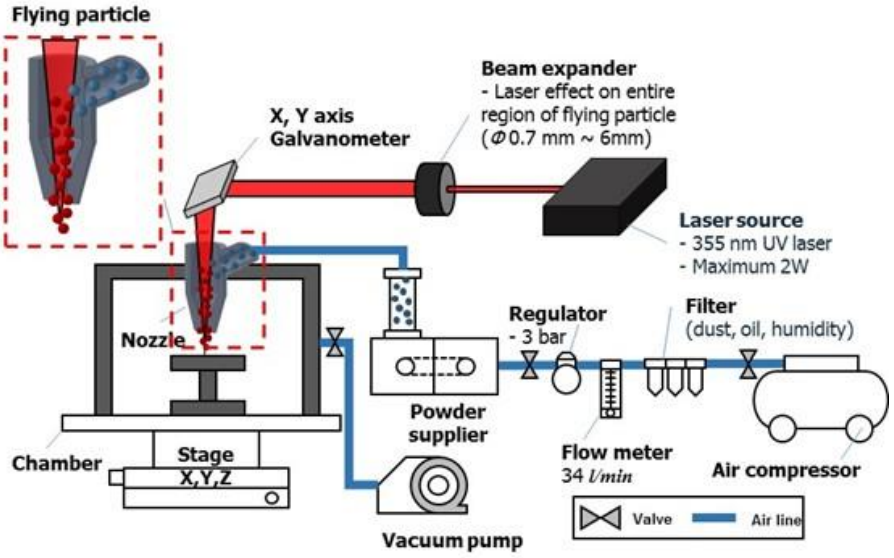

Figure 8. System configuration of direct laser assisted nanoparticle deposition system [43]

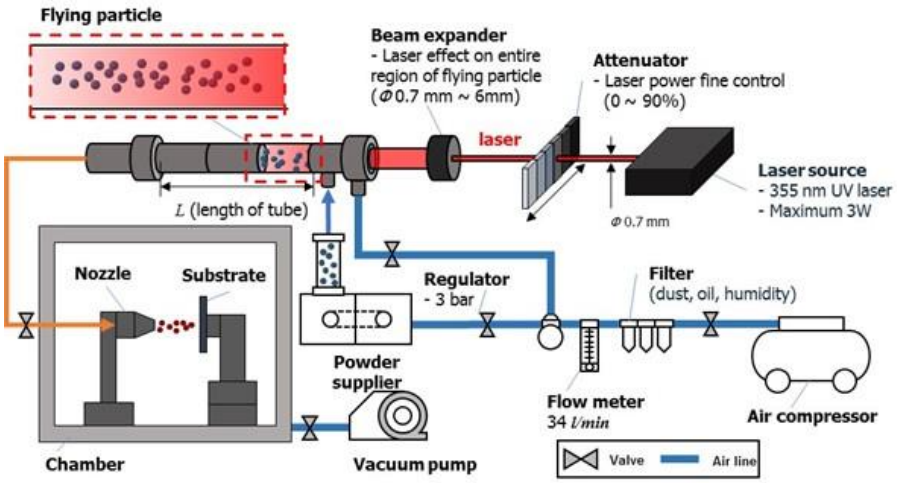

Figure 9. System configuration of indirect laser assisted nanoparticle deposition system [43]

To improve the patterning capability, AFN printing was developed by Lee *et al*. [10] for direct patterning of dry nanoparticles. Figure 10 shows the hardware schematic of the AFN printing system [7]. This process uses the similar deposition mechanism as NPDS. With a smaller nozzle outlet than that of NPDS and fast excitation-purge control, this process can aerodynamically focus nanoparticles. Therefore, it can print patterns onto the flexible and inflexible substrates with high resolution of 50 μm. Patterns can be controlled by opening and closing the valve for aerosol flow and x, y directional stage movement. However, the printing speed of AFN printing is slow, since the nozzle prints patterns serially. For large area deposition, the requirement of a vacuum state and slow process time can be a drawback. In addition, by spraying the particles, the edge of the printing is not clear. Therefore, when developing applications that include narrow gaps between patterns, such as a capacitor, complete separation of the patterns is not realized. Furthermore, durability of the deposited film is low because of high porosity.

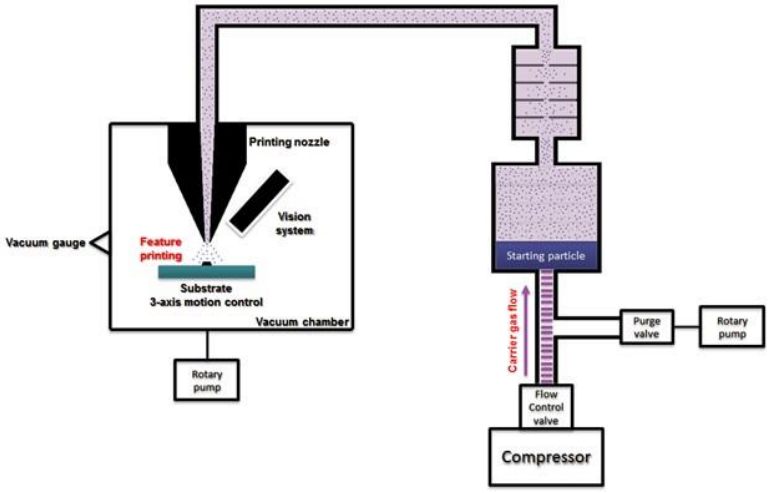

Figure 10. Hardware schematic of the AFN printing [7]

In summary, Figure 11 shows the history of low temperature deposition processes using particle [27]. Cold spray method was developed in 1980s for metal particle deposition and various methods to enhance the process were studied. In late 1990s, aerosol deposition method was developed. Auxiliary methods such as plasma and laser were added to improve the process. In 2008, NPDS was developed. After that, AFN and LaNPDS was developed to improve the process. The nanoparticle laser patterning process is developed in this research in order to overcome the limitation and improve these processes further.

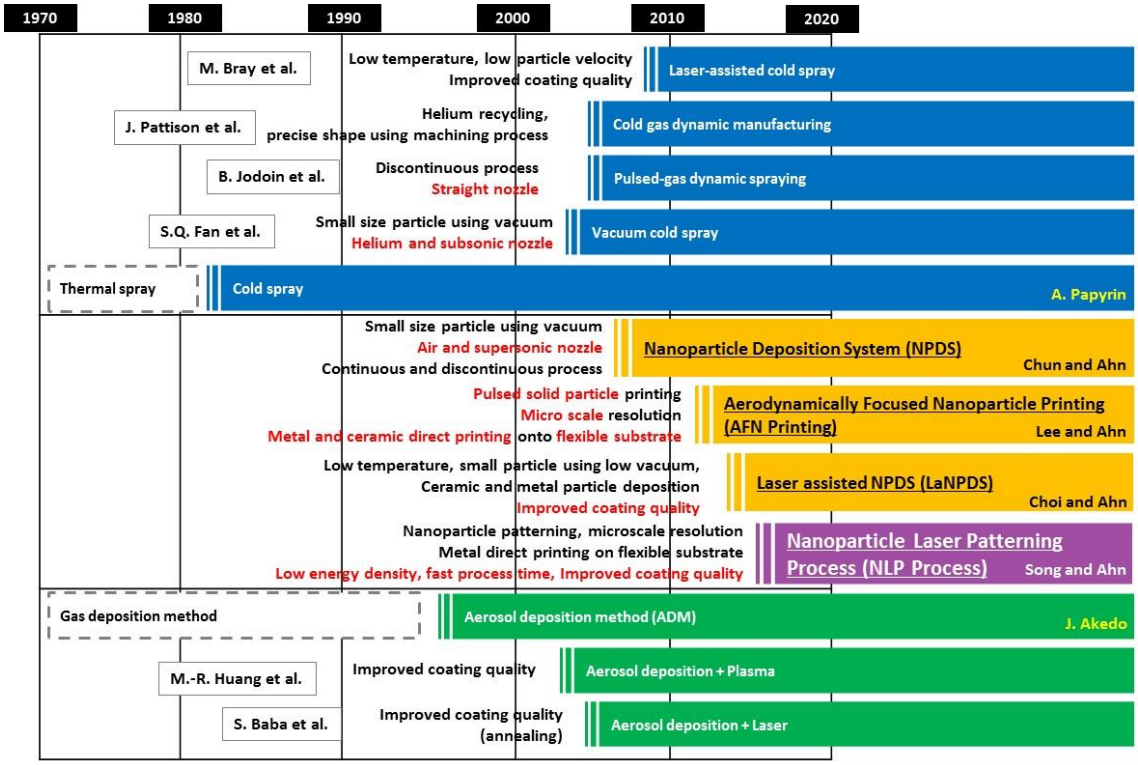

Figure 11. History of low temperature deposition processes using particle [27]

Table 1 shows the comparison of particle based printing systems. ADM, CS, NPDS, LaNPDS, AFN, and NLP processes are compared with feature scale, temperature, vacuum state, printing speed, durability, and printing type. Among these methods, AFN printing can only print small features of tens of micrometers. However, the printing speed of the AFN printing is relatively slow because it prints patterns serially. In addition, the porosity of AFN printed patterns is large which results in low durability of the printed results. Therefore, there is a need for a high throughput and durable nanoparticle micro patterning process to fabricate flexible electronics.

Table 1. Comparison of low temperature particle printing systems

	ADM	**CS**	**NPDS**	**La-NPDS**	**AFN**	**NLP**
Schema -tic diagram	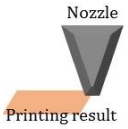					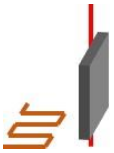
Feature scale	500 μm ~ 10 mm	500 μm ~ 10 mm	500 μm ~ 1 m	500 μm ~ 10 mm	30 μm ~ 10 mm	50 μm ~ 10 mm
Tempera -ture	Room temperature (RT)	RT ~ 800℃	RT	~35℃	RT	~60℃
Vacuum	Low vacuum	1 atm	-0.8 atm	-0.8 atm	-0.8 atm	1 atm
Printing speed (1 cm^2)	~10 sec	~5 sec	200 sec	200 sec	500 sec	200 sec
Durability	+	+	+	+++	+	+++
Printing type	Line (1D)	Line (1D)	Line (1D)	Line (1D)	Point (0D)	Line (1D)

Figure 12 shows the feature size and printing time of low temperature particle direct printing process. As discussed earlier, NPDS, La-NPDS, CS, and ADM have fast printing time but they can only print large features with sizes of hundreds of micrometers to millimeters. AFN printing can print smaller features of tens of micrometers. However, the printing speed is slow compared to other processes. To manufacture flexible electronics, the manufacturing process should be able to print small features of tens of micrometers with fast printing speed. Furthermore, the printed results should have high durability which is the limitation of particle based deposition process. NLP process was developed to meet the requirements.

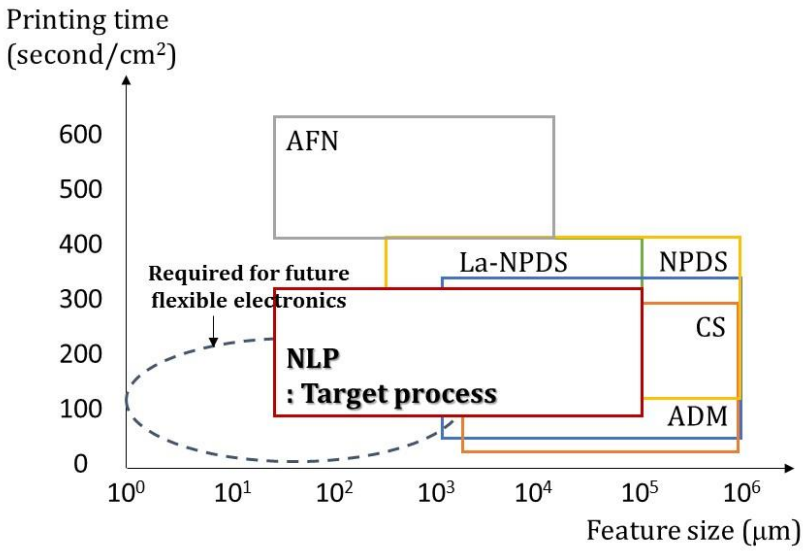

Figure 12. Process envelop for low temperature particle direct printing processes

2.2 Review on printing system with laser

Laser process has been applied to a deposition process as an auxiliary method to enhance the performance of additive nanomanufacturing [14]. Normally, by applying laser, reliability of the final product increased. Laser enables high quality surfaces with good mechanical properties. In addition, new materials can be combined. Manufacturing costs can be reduced by minimizing wasted materials during the process. Three main examples of using auxiliary laser in dry particle deposition processes are selective laser sintering (SLS), laser based deposition, and laser engineered net shaping (LENS).

Figure 13 and Table 2 show the schematic diagrams and detail process conditions of each process respectively [46-48]. As illustrated in Figure 13 (a), in SLS method [49-51], laser beam is focused on the particle layer in the powder bed, and heat facilitates the formation of necks between the particles. By repeating this process layer by layer, 3D parts in micro to mesoscale can be built. Ceramic, metal, glass, and polymer particles (polyamide, polystyrenes, thermoplastic, polyurethane, etc.) are normally used. The process uses high laser power around 100~200 W to partially melt the particles to form a dense 3D part. Normally the temperature of this process goes up to 1000°C. Layer thickness of the process is around tens of micrometers to few millimeters, and resolution is around 800 μm. In addition, high vacuum or ultra-high purity inert gas environment is required.

Figure 13 (b) shows the laser based deposition method. This method is typically applied to aerosol deposition method or cold spray deposition. ADM and CS deposition normally produce films with low adhesion force, especially for hard materials. Laser is applied in order to achieve high quality deposition with homogeneous and pore free

characteristics and to extend the range of materials and applications. Laser can also make build rate faster and reduce processing cost by removing the needs for gas heating as in CS method [52]. Combining laser with CS method has been demonstrated. Bray *et al*. [53, 54] reported that less than 1% porosity was achieved in metal coating. Several attempts were made to optimize the process, such as Coaxially Laser Assisted cold spray (COLA) project [55]. Laser can also be applied to preheat the substrate to a temperature below the particle melting point so that particles are softened and deformed more significantly during the impact [24]. Although particles are not fully melt, this process also uses high level of laser power, and the temperature reaches around 1000~1400°C.

LENS utilizes laser to weld the particles which comes out from the nozzle to build complex 3D structure [56]. Figure 13 (c) shows a schematic diagram of the process. Laser system is located coaxially with the nozzle in the system. There exist similar methods including laser metal deposition, direct energy deposition (DED), direct laser deposition, laser deposition welding, powder fusion welding, and laser cladding. Different from the laser based deposition methods, LENS uses higher temperature to fully melt the particles. With this process, metal particles are fully melt and a melt pool is formed on top of the base material and solidified. This process creates metallurgical bond between metal and substrate, thus adhesion force increases. Various kinds of metal materials can be used including iron, titanium, and tungsten with different laser conditions. The major challenge of this process is that the efficiency of the process is not high. Heat transfer from laser to the melt pool is inefficient. Loss of heat to the surroundings is significant [57]. Moreover, real time process control is difficult because of the limitations in monitoring techniques. The process quality needs to be improved [58-60].

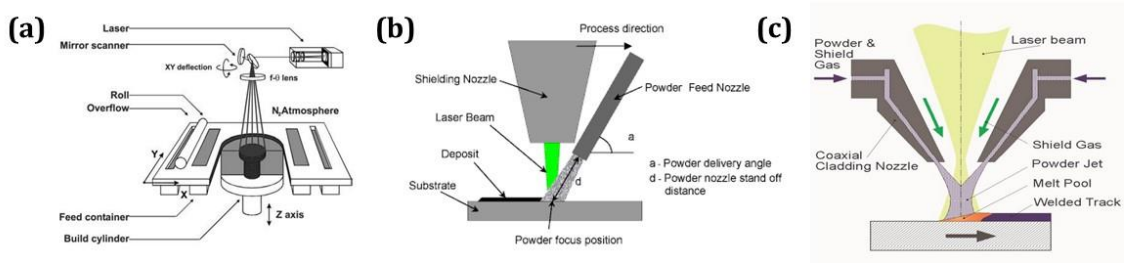

Figure 13. Schematic diagram of (a) selective laser sintering, (b) laser based deposition, and (c) laser engineered net shaping [46-48]

Table 2. Comparison between laser based printing methods [43]

	SLS	**Laser based deposition**	**LENS**
Sintering method	Solid state sintering	Partially melting	Full melting
Material	Ceramic, metal, glass	Ceramic, metal	Metal
Energy	High power laser	High power laser	High power laser
Temperature	800 ~ 1000°C	1000 ~ 1400°C	1000 ~ 1800°C
Dimension	3-D	2-D	3-D
Layer thickness	16 ~ 50 μm	300 ~ 500 μm	100 ~ 400 μm
Research institute	University of Texas	Russian Academy of Science	Sandia National Laboratories

In wet deposition processes, laser has also been used as an auxiliary method. For example, Chiolerio *et al*. [11] has combined inkjet printing with laser to improve the nanoparticle coalescence and reduce the resistance of deposited silver lines. Ko *et al*. [2] combined inkjet printing with selective laser sintering to fabricate flexible electronics with metal nanoparticles. It was shown that high resolution patterns can be printed in low temperature circumstances and the limitation of the direct inkjet printing method was

overcome. Likewise, laser is often combined with inkjet printing to improve particles coalescence and to achieve high resolution [61-63].

In summary, all of these processes introduced above use auxiliary laser to enhance the process performances. However, most of these processes have an issue regarding thermal damage, since they use high level of laser power, and it is coaxially or eccentrically affecting the substrate. Research of hybrid process combining laser and dry particle deposition mainly focuses on 3D structuring. Therefore, they use high level of laser power to melt the particles and build dense 3D parts. Laser based deposition method uses lower level of laser power to sinter the particles. However, the temperature of the process reaches around 1000°C. Thus, these methods cannot be used in flexible substrate which is vulnerable to heat. Especially, severe thermal damage is inevitable in a heat affected zone with high temperature condition. In addition, heat induced deformation of substrate is permanent [64]. When laser is applied, it melts not only the deposited material but also the base material. As a result, the film is not pure and needs more post processes to fix this problem. Therefore, there is a need for a new method which can apply laser process utilizing the advantage and reducing thermal damages at the same time. In the NLP process, low level of laser energy is used for printing. This can be realized using the nanometer sized particles with scale effect. Even though this process also uses plastic deformation of the substrate for the adhesion between particles and the substrate, the highest temperature of the substrate is less than 100°C. Therefore the deformation is not critical.

2.3 Review on models for particle deposition and laser effect

In aerosol jet printing, when the particle impacts the substrate, it either adhere or rebound from the substrate. Many researchers have studied particle impact model. For example, Dahneke [65] built a simple elastic model. Rogers & Reed [66] and Kadomtsev *et al*. [67, 68] built elastic-plastic models. Later, Qin *et al*. [69] developed the particle impact theory considering surface asperity deformation. Although there are differences, the basic idea is the same. When small particles impact, kinetic energy is converted to elastic energy and deformed. If the stress exceeds elastic yield limit of the soft material, plastic deformation happens and energy is lost. In the restitution process, if the stored elastic energy is smaller than total adhesive energy between the particle and substrate, the particle will be deposited, otherwise it will rebound [66]. A mathematical model of the impact and adhesion of microsphere based on the contact surface adhesion energy, Hertzian theory, and classical impact theory was built [70].

Deposition process has been also simulated to analyze the mechanism with various computational tools. Ogawa [71-73] used MD to model single particle deposited on substrate and studied their structural variation with different incident speeds, angles, and crystal orientations of the particle. Carrillo [74] used MD model with theoretical calculations to study nanoparticle deformation and its relationship with system parameters. A surface energy of nanoparticle is considered to predict nanoparticle adhesion. The result was compared with classical Johnson, Kendall, and Roberts (JKR) theory. However, MD usually deals with single particle because of its limitation in time and length scales. Figure 14 shows the length and time scale of different simulation tools [75]. MD can only simulate the behavior of sub-microscale structures for a period of nanoseconds. Therefore, the

deposition process modeled by MD normally predicts the epitaxial growth of the films [76-79], or the adhesive energy between nanoparticle and substrate by detachment [80, 81]. Kinetic Monte Carlo (KMC) and finite element method (FEM) are capable of simulating larger scale model than MD. However, most research still focuses on a single particle analysis. For example, Akedo [9, 82] studied change of local temperature and pressure with a single particle and the substrate using FEM. Chun *et al*. [35], studied bonding mechanism of ceramic particle in nanoparticle deposition system with numerical analysis and experimental results. There are deposition models which simulate multiple particles with KMC [83, 84] but the processes are not similar to the aerosol deposition of particles. These models studied sedimentation or pulsed laser deposition processes and only focused on the dislocation and island growth rather than deposition mechanism itself.

Likewise, there is an absence in deposition model which consider multiple particles. Therefore, with the existing deposition models, it is difficult to see the sintering and bonding of the particles because they are limited to single particle analysis. Therefore, morphological changes of the printed results are difficult to study with these current models. In this research, deposition and laser effect are combined in the integrated coarse grained cKMC simulation in mesoscale.

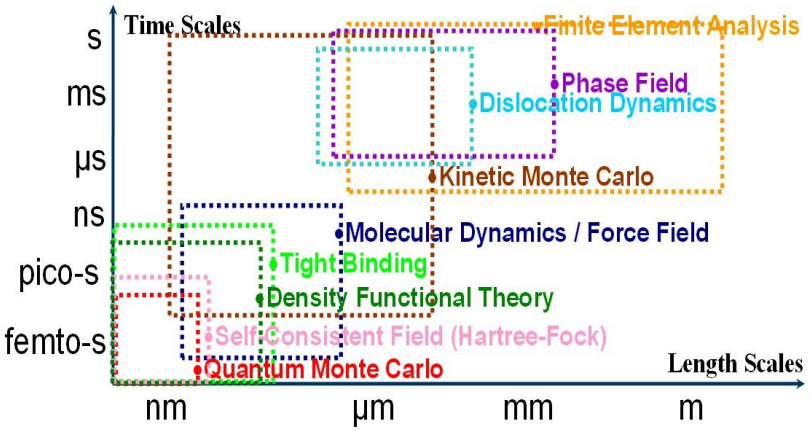

Figure 14. Simulation with nanomaterials across different scales [75]

Furthermore, there is an absence of model which predicts printing of the particles considering both kinetic and thermal energy. Models of particles treated by laser are normally focused on the particles which are not moving. MD [85-97] is the main approach for simulating laser effect on nanoparticles. It is usually used to elucidate sintering mechanism of certain nanoparticle such as Cu, Al, TiO_2, and Au. Most of these models use different initial conditions such as particle size, orientation, and different sintering condition such as pressure and temperature, then analyze the results to explain sintering process or mechanism. Simulated results include neck diameter, number of pores, flow stress, hardness, average grain size, density, atomic mobility, relative shrinkage, relative rotation, surface area, characteristic sintering time, etc. Usually these results are compared with the results from analytical or experimental model to validate the model and to propose new or better explanation for sintering mechanism. For example, Buesser *et al*. [98] studied growth of TiO_2 nanoparticles by sintering. They analyzed evolution of nanoparticle surface area during the sintering process to study sintering mechanism. Zhu *et al*. [99] studied sintering of two copper nanoparticles. The aligned and randomly oriented particles were

studied to check the deformation and rotation in the necking part. Raut *et al*. [100] studied the consolidation of two or three aluminum nanoparticles and investigate the effect of temperature, particle size, and crystallographic orientation on the sintering effect. The dominant sintering mechanism is examined by measuring shear stresses and mobility of atoms near the necking area. In addition, there have been numerous attempts to simulate microstructural evolution during sintering process with KMC model. Their models are usually based on grain growth and pore migration process. Particularly the Ising or Potts model, where state changes by minimizing system energy without information of time, has been used to simulate morphological change of particles in sintering [101-114]. For instance, Tikare *et al*. [108] used a KMC Potts model to simulate three major processes of sintering, including formation, diffusion, and densification. This method was successfully applied to a three-particle model. It can predict microstructural evolution by simulating the expected topological changes and the kinetics of densification. Shrinkage rate with respect to time was derived from simulation results and compared with the one predicted by sintering theory. The model was further extended to complex powder bed compacted with large numbers of particles with arbitrary shapes [107]. Hara *et al*. [111] used KMC Potts model to predict sub-micro sized nickel particle sintering and validated by comparing with focused ion beam – scanning electron microscope (FIB-SEM) images. Olevsky [112] simulated microstructural evolution during sintering process with KMC model, which is combined with continuum theory. The resulting images of the microstructures as time series were used to calculate constitutive parameters of sintering stress and normalized bulk viscosity. Bjørk *et al*. [114] studied microstructural evolution and sintering behavior of powder compacts composed of spherical particles with different particle sizes. It was found

that densification rate, final relative density, grain size, grain growth, total number of necks, neck area, and pore size of particles varied with different initial particle size distributions. Other KMC models were also used for sintering analysis [115-119]. For example, Westerhoff *et al*. [117] used off-lattice KMC to simulate particle aggregation. The relaxation time for surface evolution and the influence of elasticity on sintering were investigated. Simulation results were compared with Koch-Friedlander theory. Lim *et al*. [120] compared the rate of neck growth in atomistic KMC simulation with classical continuum theory prediction and in-situ tunneling electron microscopy (TEM) observation of gold nanoparticle coalescence. Furthermore, phase field simulation is often used for sintering analysis [121, 122].

Likewise, there is an absence of model to predict printing of the particles considering both kinetic and thermal energy. Current models can only analyze one aspect which is not suitable for the hybrid system. There are few attempts to predict deposition with thermal and kinetic energy. However, almost all of the models deal with the process with high temperature which includes melt pool [56, 123, 124]. In the NLP process, particle deposit with kinetic energy of impact and thermal effect below particle melting point at the same time. In this research, molecular dynamics will be combined with an analytical model as a multiscale approach to introduce thermal effect in the particle impact model.

2.4 Review on fabrication process for applications

Wettability is an important surface property for various applications such as self-cleaning clothes or building walls. It can be controlled by pattern width. Yoon *et al*. [125] studied wetting property of silver patterns printed via AFN printing with different pattern widths. Width of the patterns were changed from 100 to 500 μm, and different contact angles of the water droplet were measured. Furthermore, chemical composition can change the wetting property. Chun *et al*. [126] machined a copper plate with laser and annealed it as a post process in order to get different oxidation degree of the material. Cu_2O and CuO has different hydrophobic and hydrophilic property. Other than these two studies, many researchers studied wettability change of the surface [127-130]. Some of them use bio-mimic structure such as lotus leaves to have super hydrophobicity [131-133]. Current fabrication processes control wetting property either with pattern width or with chemical composition of the materials. None of the research reported uses pattern width and chemical composition simultaneously to control wetting property. In this research, pattern width and composition of the materials will be controlled at the same time using the NLP process.

Paper substrate is widely used in flexible electronics using the advantages of low cost, light weight, and eco-friendly [134]. Recently, kirigami structure was used to fabricate various intriguing applications. Hwang *et al*. [135] fabricated tunable mechanical metamaterials through hybrid kirigami structure. To have functionality, it was first either spray coated or casted followed by mixing of the functional materials and then cut with CO_2 laser. Gao *et al*. [136] fabricated paper fish sensors by printing graphene followed by plasma treatment on paper and folding and cutting with scissors. Although

these results were successfully applied as a sensor or metamaterials, the fabrication processes were complicated with several steps. Cutting and printing were not performed within one system which requires position referencing between the processes. This referencing technology is highly demanding when the patterns are complicated in micro or nanoscale. In NLP process, cutting and printing can be conducted within one system, and kirigami electronics were fabricated as a proof of concept.

Strain sensor is one of the most widely studied applications in direct printing technology. This is because particle-based sensors normally have higher sensitivity than sensors fabricated by other processes [137]. Figure 15 shows review on strain sensors fabricated with different types of materials. In most cases, gauge factor is controlled by the materials, not by the process itself. In addition, durabilities of the printed sensors are low. They are normally printed with inkjet printing or soft lithograph process. With these processes, it is difficult to control the performance of the application by the process itself. In this research, performance of the sensors can be controlled by using different laser conditions. In addition, strain sensors and conductive lines can be printed together within one system.

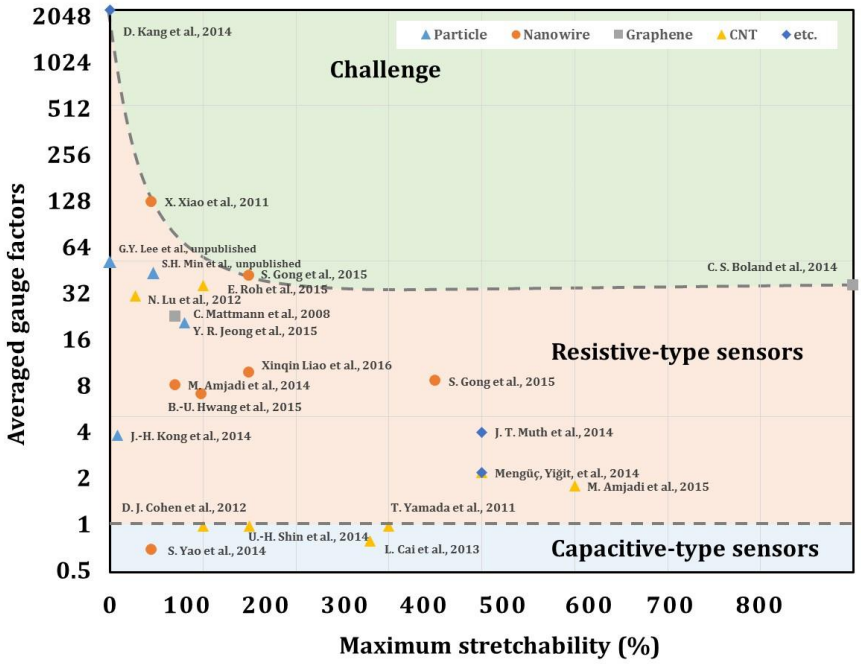

Figure 15. Review on the researches of strain sensors [137]

CHAPTER 3. SYSTEM DESIGN AND INTEGRATION

A high throughput direct writing process for flexible electronics was developed, where nanoparticles are sintered with laser while they are selectively deposited. This process is called nanoparticle laser patterning process. In Section 3.1, system configuration and detail printing process will be introduced. The whole NLP process is consist of two processes: printing process and cleaning process. These will be explained in detail in two subsections. In Section 3.2, setup of the actual system and detail specifications of the process will be explained.

3.1 Process configuration

The proposed NLP process is based on the concept of commercial laser printer in NPDS, as previously introduced in Section 2.1. It is a hybrid process of NPDS and laser process to selectively deposit or selectively control the properties of the printed results. The NLP process consists of two steps: printing and cleaning processes. Figure 16 shows the detail process sequence of the NLP process to print strain gauge pattern. This figure only depicts a nozzle, laser path, and printed area. In this diagram, detail laser system, particle feeding system, and substrate moving system are not described. These systems are explained in Section 3.1.1 in detail. Figure 16 (a)-(d) show the printing process and (e) shows the cleaning process. In the printing process, when the nozzle scans the substrate in y-axis direction, laser scans and selectively shines on the substrate through the nozzle in x-axis direction. As the substrate moves, the laser scan path changes based on the pattern design. Meanwhile, particles are constantly fed through the whole area of nozzle outlet on the substrate in z-axis direction. As shown in Figure 16 (b), the area printed with laser

irradiation is illustrated in a dark color whereas, area printed without laser irradiation is marked as a bright color. However, only the laser irradiated particles deposit and remain on the substrate after the cleaning process. In the cleaning process, brush is carefully used to remove the laser unirradiated particles without damaging the printed patterns.

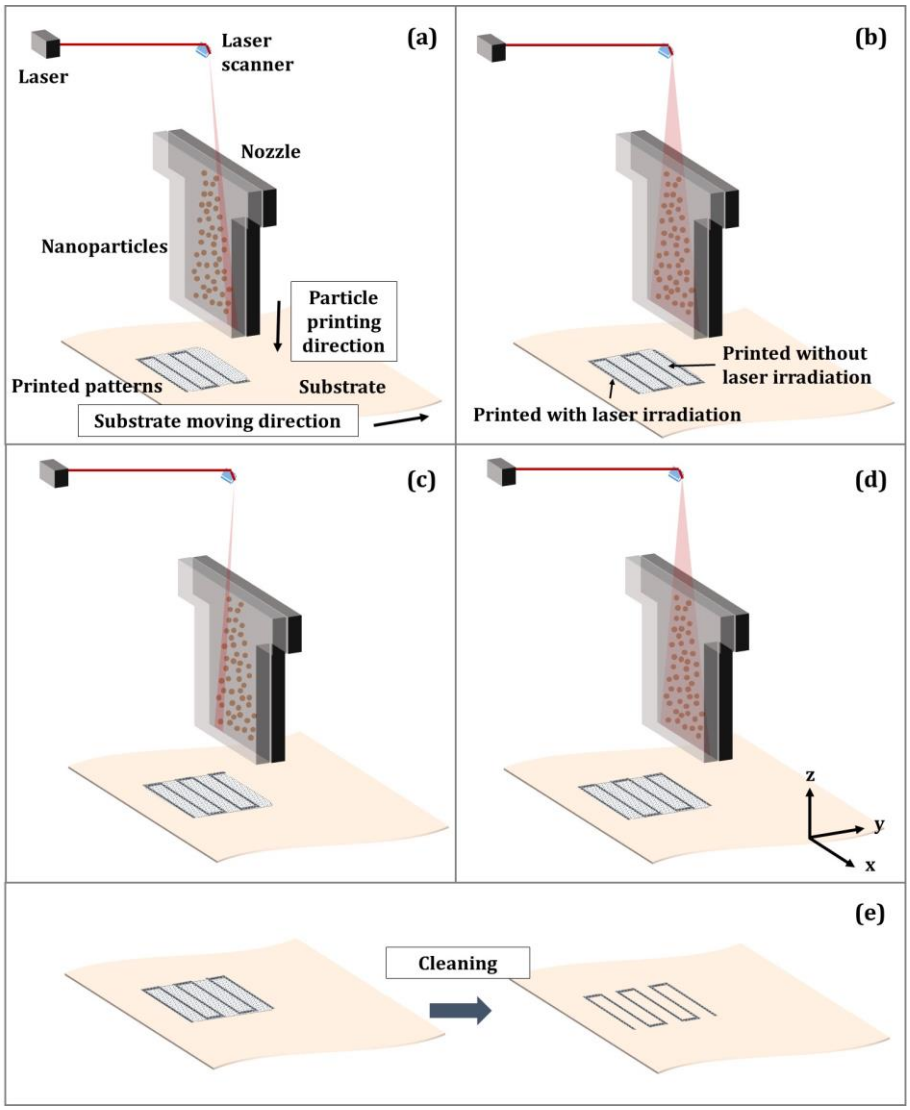

Figure 16. The process sequence of NLP process

3.1.1 Printing process

Figure 17 is the system configuration of the process. It is composed of two parts, deposition part and laser part. The dash line shows the path of the particle flow and the solid line shows the path of the laser beam. Specifically, deposition part consists of air compressor, aerosol generator, nozzle, chamber, motorized stage, and stage controller. The subsonic slit nozzle was designed by Chun [27]. The nozzle inlet has a circular shape with a diameter of 10 mm. The nozzle outlet has a square shape of size 0.4×10 mm^2. The size of the nozzle slit is large enough for the beam to pass without energy loss. A fluidized bed aerosol generator (TSI 3400A, TSI Incorporated, USA) is used as an aerosol generator. It uses a continuous drive of bead chain to carry particles from the powder reservoir to the area where they are mixed with compressed air. Compressed air carries the particles in an aerosol state and goes through the nozzle to the substrate. The pressure of the compressed air was set as 1 bar. The chamber was designed and fabricated with acrylic material and used to prevent the aerosol of particles from spreading to the surroundings. The size of the chamber is $150\times150\times60$ mm^3. Different from the NPDS system, vacuum pump was not used in the process. The compressed air goes out from the chamber through a hole to make pressure inside the chamber constant. This system uses atmospheric condition for deposition. This is because laser process helps deposition even without a vacuum condition. Particles moving with lower velocity are more likely to deposit, because high kinetic energy makes particles rebound from the substrate. This will be discussed in Section 5.2.6 and 5.2.7. If the chamber is in a vacuum state, the velocity of the particles will be higher because of the larger pressure difference.

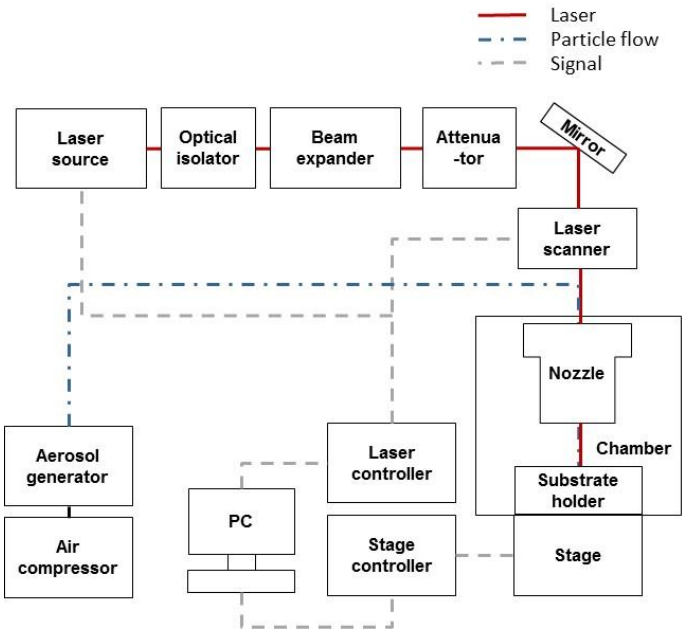

Figure 17. System configuration of NLP process

In order to maintain the laser path through the nozzle, nozzle and chamber were fixed in their positions and the substrate was moved during the printing process. The nozzle was attached on top of the chamber. The substrate holder is located below the nozzle. The other end of it was attached to the stage which is located outside the chamber to prevent contaminations with particles. A motorized stage (AM3-0602, Micro Motion Technology, Korea) was used. Figure 18 shows the computer-aided design (CAD) model of the system including the chamber, nozzle, substrate holder, and stage. Supporting parts on each sides and the bottom of the stage were fixed to the surface plate. Particle flow and laser path are separated at first. When the particles enter the nozzle, they are started to get affected by laser. Figure 19 shows how the stage moves. The middle part is a bellows made with rubber. As the stage moves from the left to the right, the substrate holder which is attached to the stage moves together with the deformation of the rubber bellows. Material and geometry of the bellows were selected considering the deformation range and stiffness. The bellows

should follow the motion of the stage. If the length and diameter of the bellows are small, the deformation range is small. Therefore, travel distance of the stage is small. If the material is too stiff, it does not follow the stage movement and slip occurs.

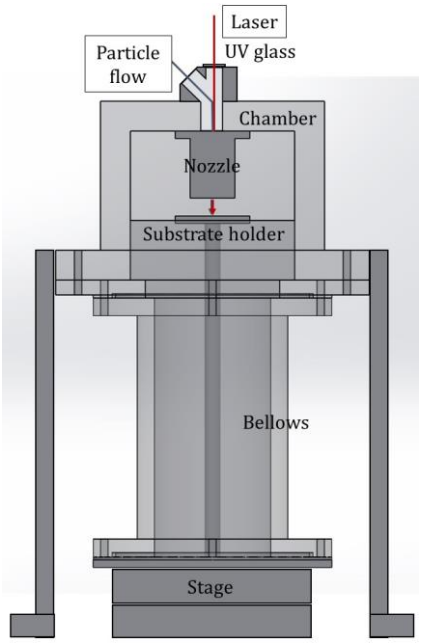

Figure 18. CAD model of chamber, nozzle, substrate holder and stage

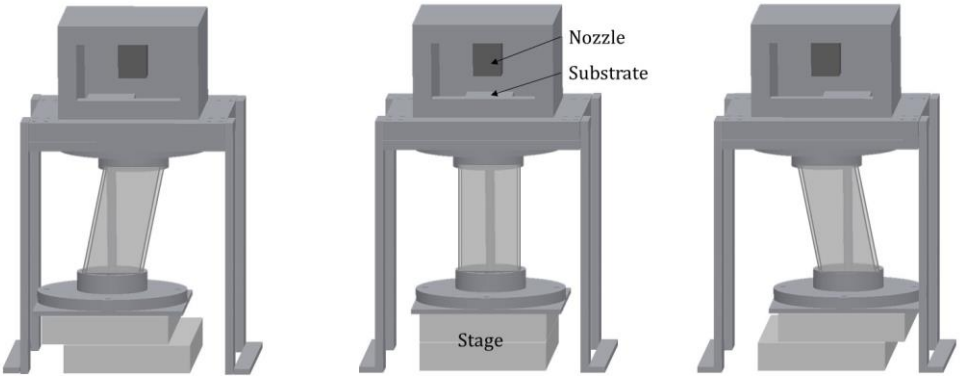

Figure 19. CAD model of how substrate moves

The laser part consists of a laser source, optical isolator, beam expander, attenuator, reflective mirror, laser scanner, and controller. The optical isolator is used to prevent the damage of the laser source from the reflected beam when using a reflective substrate. The beam expander expands the beam size from 0.7 to 6 mm. It reduces the divergence and controls the input beam diameter to minimize the spot size. The attenuator is used to control the laser power precisely. The reflective mirror shifts the path of the laser beam towards the laser scanner. The laser scanner controls the laser path based on the pattern design. It is interconnected with laser marking software (EZCAD, Integrated Technology INC, USA). The laser beam goes through the nozzle and directly shines on the substrate. Detail laser conditions are described in Table 3. In this system, ultraviolet (UV) laser was used (Awave-355nm, Advanced Optowave Corporation, USA) because metals normally have high absorbance near UV wavelength. The absorption coefficient of the nanoparticles used in the process is analyzed in Figure 20. Both silver and copper particles have high absorption coefficients near UV wavelength range. In addition, a nanosecond pulse type laser is used to effectively transfer heat compared to a continuous mode laser. A pulse of the high power beam is repeated with a nanosecond pulse width, while continuous mode laser uses the same averaged power continuously. High thermal energy is transferred to the particles within a short period of time. This can reduce thermal damage preventing the accumulation of the heat compared to the continuous mode. In addition, since the process uses nanometer sized particles, the efficiency of the heat absorption is high because of large surface to volume ratio. Therefore, power level of the laser is relatively low compared to the other processes introduced in Section 2.2. The highest laser power used was 800 mW.

Table 3. Laser conditions

Property	Value
Wavelength	355 nm
Power	< 4 W
Spatial mode	TEM00
Frequency	30 kHz
Pulse width	< 15 ns

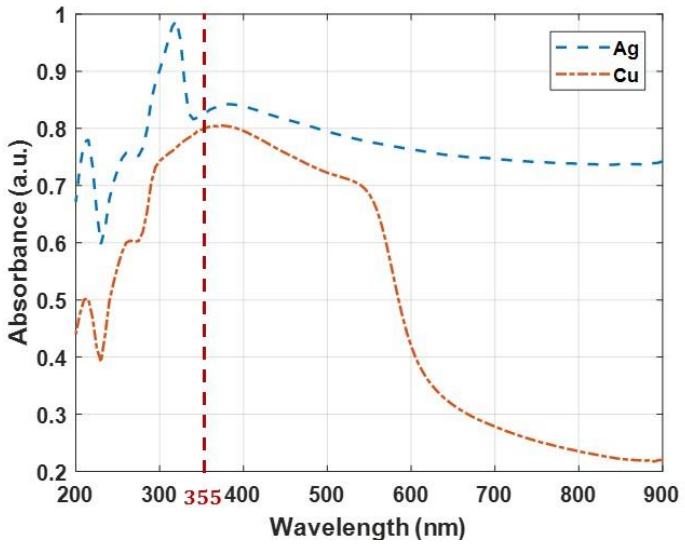

Figure 20. Absorption coefficient of silver and copper particles

3.1.2 Cleaning process

The cleaning process was done after the printing process to remove the particles in the area without laser irradiation. Brushing, air blowing, and taping methods were tested. Figure 21 shows the methods and their results. The cleaning method should completely remove the undesired area without damaging the printed patterns. Table 4 shows the comparison of the methods. The brushing method can remove the particles efficiently, at the same time causes less damage on the printed patterns. The air blowing method cannot remove the particles even though there was no damage on the printed patterns. The taping method can effectively remove the undesired particles. However, it also removes parts of the printed patterns. Therefore, the brushing method was selected as the cleaning process for the NLP process.

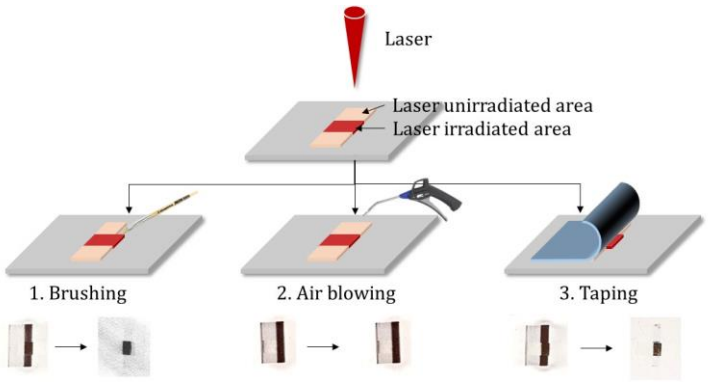

Figure 21. Cleaning methods for area without laser irradiation

Table 4. Comparison of cleaning methods

	Brushing	**Air blowing**	**Taping**
Cleaning	○	×	○
Damage on patterns	×	×	○

3.2 Process design and integration

The hardware was organized and integrated based on the system design described in Section 3.1. Figure 22 shows the actual hardware setup for the printing system. The path of the laser beam and the particle flow are described with a solid and dash line respectively. The laser beam goes through the nozzle and focuses on the substrate. The printing was conducted on the laser focal point.

There is a power loss inside the laser scanner and the nozzle. Therefore, there are differences between the applied laser power and actual laser power that affects the particles. Figure 23 shows the measured points of the power levels to evaluate the power loss. Point 1 is the point where the beam enters the laser scanner. Point 2 is the point where the beam passes through the scanner and enters the nozzle. Point 3 is the point where the beam passes through the nozzle. The power measured at point 3 is the actual power that the particles are affected. Laser power levels were changed from 25 to 800 mW. These were measured and set at point 1.

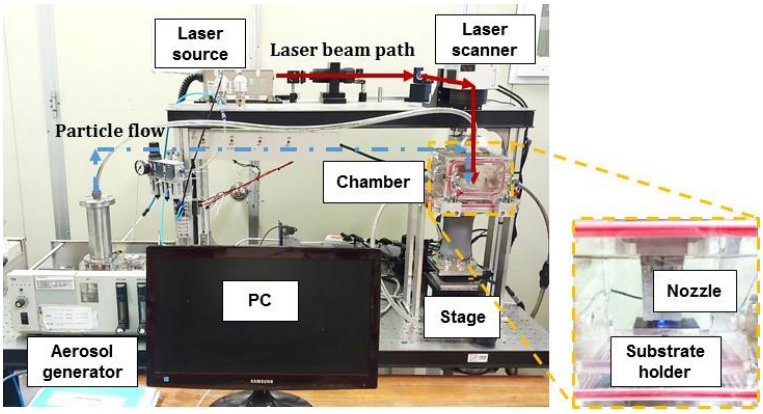

Figure 22. Hardware setup of NLP process

The measured power at each point is listed in Table 5. Almost half of the power is lost when it passes through the laser scanner. The half of the remaining power is lost when it passes through the nozzle. Laser energy density was calculated accordingly. The laser power was converted to the energy density considering laser spot size which has the diameter of 50 μm and laser irradiation time. The calculated energy densities were 0.15, 0.31, 0.76, 1.40, 2.62, and 5.86 J/cm^2 for 25, 50, 100, 200, 400, and 800 mW of applied laser power respectively.

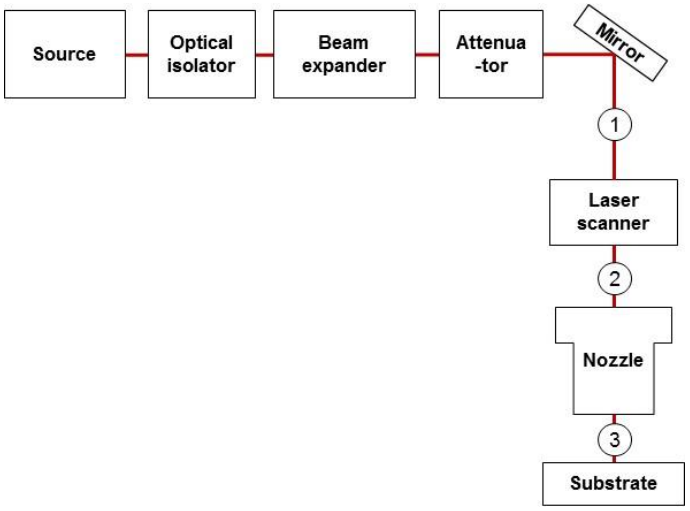

Figure 23. Measured point of laser beam power

Table 5. Energy loss of laser beam

Point	Laser power (mW)					
1	25	50	100	200	400	800
2	9	19	43	95	188	437
3	6	12	30	55	103	230

CHAPTER 4. PERFORMANCE EVALUATION AND ANALYSIS

To study the process-structure-property relationship, the effects of process parameters on the deposition performance are assessed. Evaluation of the newly developed process and the printed results was done with various characterization methods. There are mainly two factors that affect the performance of the printing: printing parameters and laser conditions. In Section 4.1, selected printed results with the NLP process are introduced. In Section 4.2, printing performances with different printing parameters are analyzed. The resolution of the process will be evaluated. In addition, the effect of the printing conditions on adhesion and the effect of the stand off distance (SoD) on the printing will be investigated. In Section 4.3, printing performances with different laser conditions are analyzed. The thermal effects of laser on the morphology and porosity of films are observed under scanning electron microscope. Chemical composition of printed pattern is also characterized using X-ray diffractometer. The electrical and mechanical property will be analyzed and discussed in Section 4.4. The sensitivity of electromechanical property with respect to the porosity, as a result of different laser energy densities, is analyzed. Finally, the process-structure-property relationship will be built.

4.1 Printed results

Copper and silver particles were used to print patterns on board paper and PET substrate. They were bought from Sigma Aldrich. Substrates were bought from stationery and the thickness of paper and PET substrate was 0.32 and 0.12 mm respectively. Figure 24 shows SEM images of raw particles. The diameter of the particles were same or less than 100 nm. These raw particles were used for printing without any pre-treatment. Figure 25 shows the optical images of the printed copper patterns with different magnitudes. Red boxes marked on the left figures are magnified and shown on the right. Various patterns were printed on paper and PET substrate. The applied laser power was 400 mW, which is equal to the energy density of 2.62 J/cm^2. Other laser parameters were the same as described in Table 3 and laser scan speed was 50 mm/s. The aerosol pressure of the compressed air was 1 bar, feed rate of the stage was 25 μm/s, and SoD was 3 mm. By changing laser scanning area and timing, multiple lines, cross lines, and curved patterns were printed.

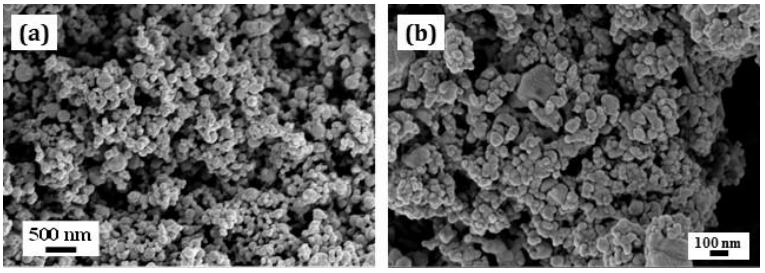

Figure 24. SEM image of raw (a) copper and (b) silver particles

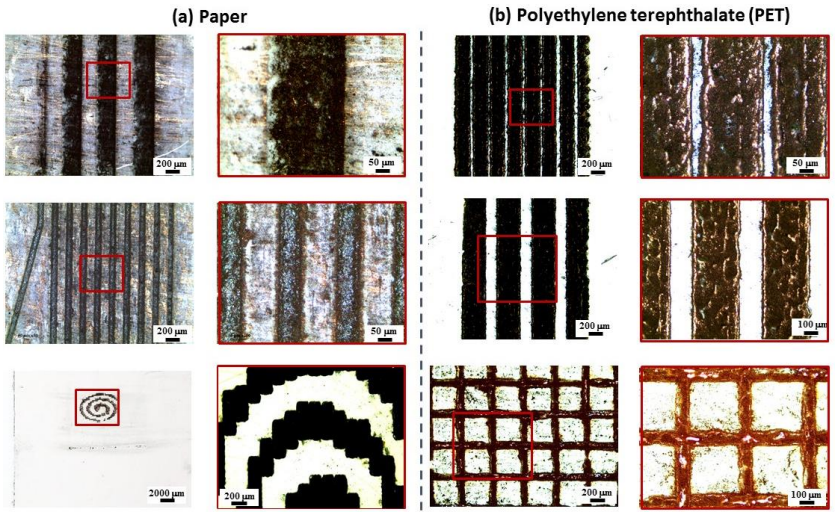

Figure 25. Printed result of various patterns printed with copper particles on paper and PET substrate

4.2 Printing performance with different printing parameters

Many process parameters are involved in the printing process. First of all, material selection of nanoparticle and substrate is important for printing. Specifically, the selection of nanoparticles including material type, diameter, and phase as well as the selection of the substrate including material type and surface roughness affect the printing results. These features are related to the properties of the materials. Furthermore, printing conditions such as temperature, humidity, and vacuum state of the surroundings also change the printing results. Moreover, the printing process itself has different process parameters. A shape and type of the nozzle, SoD, aerosol pressure, stage feed rate, carrying gas type, etc. can be controlled during the printing process. The effect of printing parameters will be studied in this section. In the laser process, wavelength, laser scan speed, frequency, irradiation time, and power level can be varied. The effect of the laser parameters will be discussed in Section 4.3.

4.2.1 Resolution

Among various process parameters, stage feed rate and laser scan speed are the main factors that can affect the line width of the printed patterns. Therefore, the minimum line width which is regarded as a process resolution was evaluated with different laser scan speed and stage feed rate. Figure 26 and Figure 27 show the change of line width with different conditions on PET and paper substrate respectively. This test was done without turning off the laser to see the correlation between the two parameters. Copper particles were used for printing material. Laser energy density was 1.4 J/cm^2. Laser scans the substrate with the scan speed of 2.5, 5, and 10 mm/s while the stage is moving with the velocity of 5, 10, 20, and 40 μm/s. If the scan speed of laser is higher than 20 mm/s, the patterns were not separated. The line width decreases with higher laser scan speed. The minimum line width was 50.87 μm on PET substrate. In case of paper, it was 28.64 μm. The focal size of the laser beam used in the process is 50 μm. It is assumed that the achieved minimum line width is the effective area of the Gaussian shape beam. Paper substrate requires higher level of laser energy for deposition. The detail printing mechanism related to the laser energy density will be discussed in Chapter 5. If the focal size of the beam can be reduced or Gaussian beam shape can be controlled with additional optical components, the resolution is expected to decrease accordingly. The patterns can be also printed with controlling the operating time of the laser. The minimum line space was measured using this method. This is important for applications in flexible electronics such as a capacitor. Not only the distance but also the complete separation between lines are important. A conductivity test was done to examine the complete separation of two adjacent lines. Figure 28 shows the optical image and confocal result of the adjacent lines. When the line space

was 30 μm, the lines were not completely separated. However, when the line space was 40 μm, there was no contact area. Therefore there was no conductance between two lines.

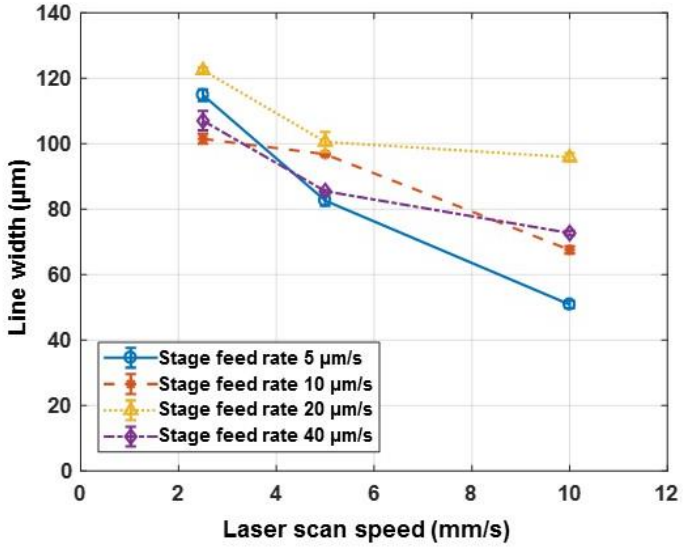

Figure 26. Line width with respect to stage feed rate and laser scan speed on PET substrate

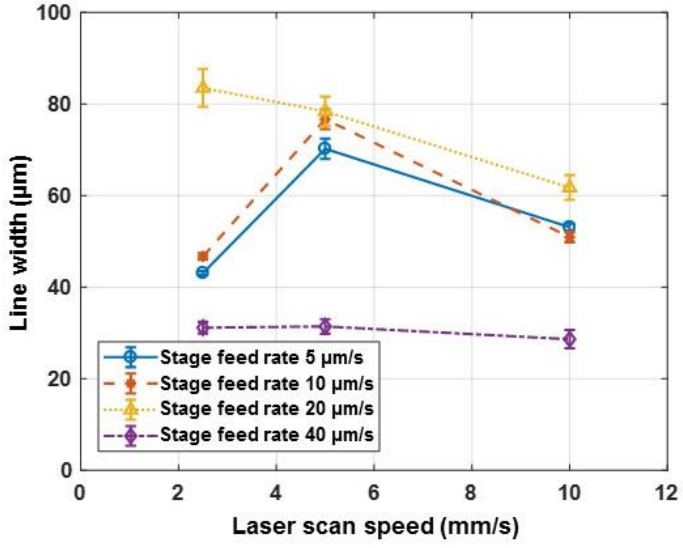

Figure 27. Line width with respect to stage feed rate and laser scan speed on paper substrate

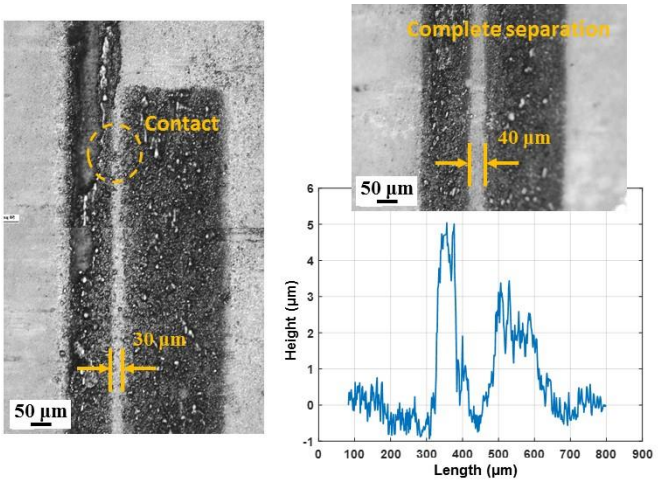

Figure 28. Optical images and confocal result of adjacent lines

4.2.2 Adhesion test

Adhesion test was conducted to test the adhesive force and durability of the deposited patterns. Scotch tape test was conducted following the method shown in the literature [138]. Figure 29 shows the printed copper particles on paper substrate with different printing conditions before conducting the adhesion test. Laser energy density was 1.4 J/cm^2. Figure 30 shows the images of the samples after twice of detachment tests. The area printed without laser irradiation was completely removed after twice of scotch tape tests. However, most of the area printed with laser irradiation remained. Especially, adhesion between the substrate and the particles in the area printed with laser irradiation was durable when particles were printed with proper process conditions. Printing conditions for durable adhesion were feed rate of 25 µm/s and laser scan speed of 50 mm/s.

Scan speed / Feed rate	2.5 mm/s	50 mm/s	100 mm/s	200 mm/s
25 µm/s				
50 µm/s				
75 µm/s				

Figure 29. Adhesion test of printed results: Before detachment

Scan speed / Feed rate	2.5 mm/s	50 mm/s	100 mm/s	200 mm/s
25 µm/s				
50 µm/s				
75 µm/s				

Figure 30. Adhesion test of printed results: After twice of detachment tests

4.2.3 Effect of SoD

The effect of SoD was also tested. Since the NLP process is a direct printing method, whether particles can be printed on the curved surfaces was tested. Figure 31 shows the printing process on the different curved surfaces. SoD is different through the nozzle length direction. Figure 32 shows an illustration of the location of the nozzle and curved substrate. Figure 33 shows the printed results. The copper nanoparticles were successfully printed on the curved paper substrate. Laser energy density was 2.62 J/cm^2 and laser scan speed was 50 mm/s. The aerosol pressure of the compressed air was 1 bar, feed rate of the stage was 25 μm/s, and SoD was 3 mm. Adjusting a laser focal point is important to effectively transfer thermal energy but small error can be accepted within a depth of focus. In optics, the depth of focus is the distance of tolerance of the best focal point where the beam is judged to be in focus. Micro-Electro-Mechanical Systems (MEMS) process is highly sensitive to SoD which is a main drawback. The NLP process is less sensitive to SoD compared to the MEMS process.

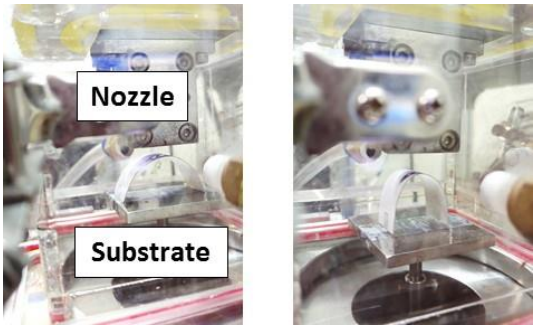

Figure 31. Experimental setup for direct printing on curved surface

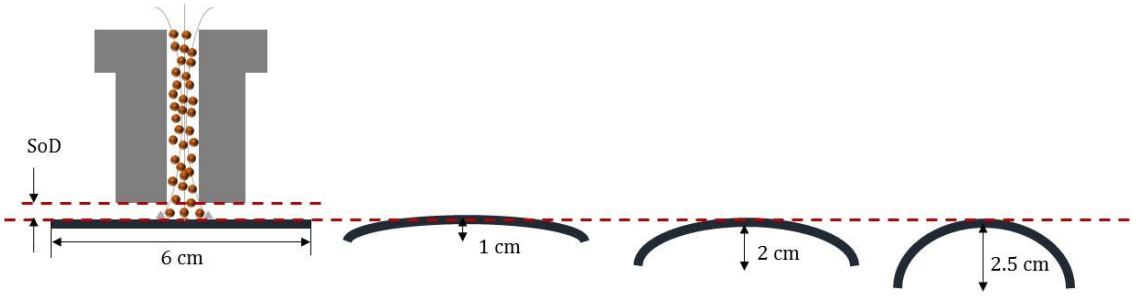

Figure 32. Schematic diagram of direct printing on curved surface

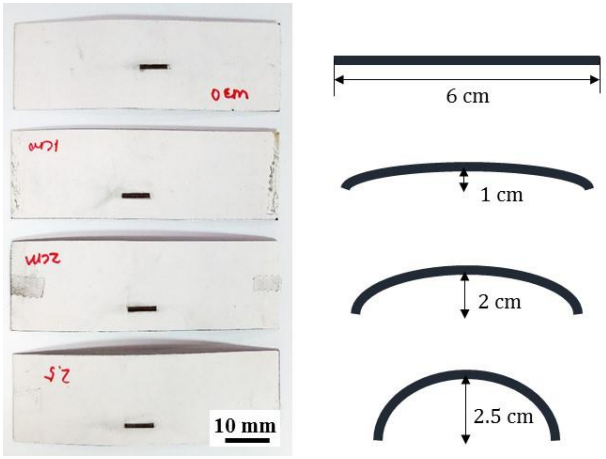

Figure 33. Deposition results

4.3 Printing performance with different laser conditions

Evaluation of the process and the deposition results with different laser conditions was studied. With laser treatment, sintering of nanoparticles occurs and morphologies of the printed patterns change. The morphological changes of the printed results will be investigated with SEM and confocal spectroscopy. In addition, thermal energy of the laser can change the composition or phase of the material itself. It will be evaluated using XRD analysis.

4.3.1 Morphology

In order to see the sintering effect of laser, microscopic images of printed patterns were observed under SEM. Figure 34 shows SEM images of the copper patterns on paper and PET substrate with different magnitudes. As marked with circles, sintering of the nanoparticles was observed. The nanoparticles are coalesced and their boundaries are combined together forming bigger agglomerated particles. Especially, for PET substrate, clear interlayer between the copper patterns and PET substrate was observed.

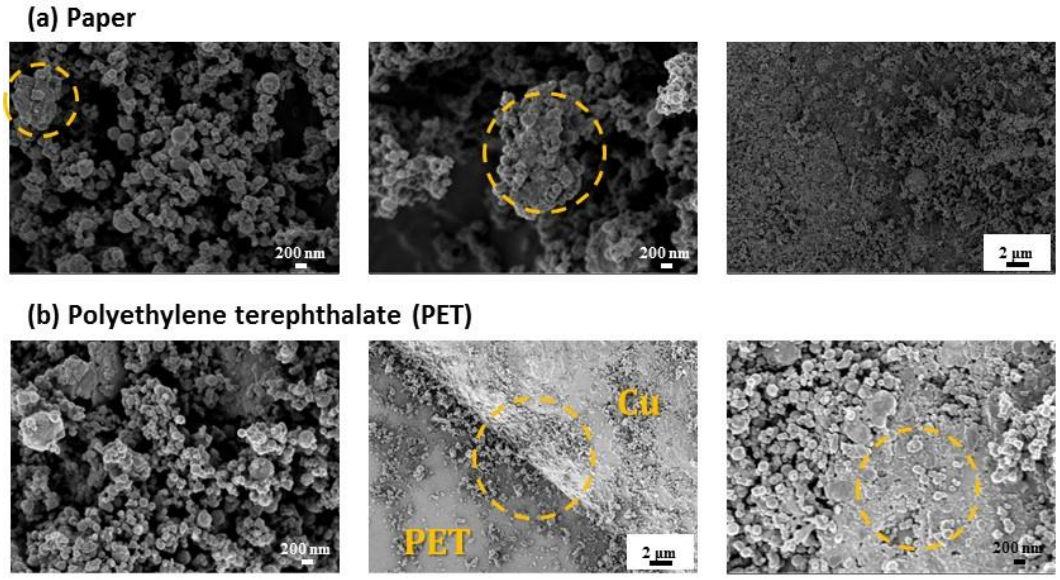

Figure 34. SEM image of copper patterns surface

In order to evaluate the sintering effect with different laser energy densities, morphology changes were compared. Figure 35 shows the SEM images of the cross section and surface of the copper patterns printed on paper substrate with different laser energy densities. Surface image was taken at random place on top of the printed patterns. Cross section image was observed by cutting the pocket on the printed patterns by FIB milling. They were not clear because of the re-deposition and melting of the particles. The particles processed by FIB at the boundary tend to redeposit on the adjacent area, precluding the observation of the clear cross section. Besides, particles are melted by the ion beam energy, because beam energy is high enough to cut a hole. Therefore, as the last step, fine milling is conducted with low energy beam in order to observe clear cross section. However, the surface is still affected by the ion beam energy. Still, we can see the trends that as the laser energy density increases, porosity decreases because of the sintering effect. Porosity is related to the contact between particles and affects both electrical and mechanical properties. If the porosity is large, the contact between the particles is weak. Therefore, path of the electrons is hindered. The resistance of the printed pattern is small accordingly. Likewise, if the porosity is small, the contact area between the particles is large. Therefore, mechanical property is stronger than patterns with larger porosity. This will be discussed more in detail in Section 4.4.

	1.40 J/cm^2	2.62 J/cm^2	5.86 J/cm^2
Cross section image	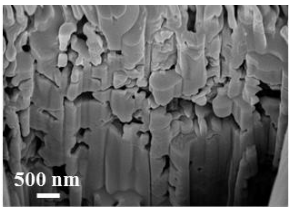	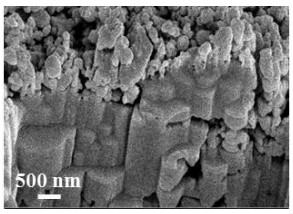	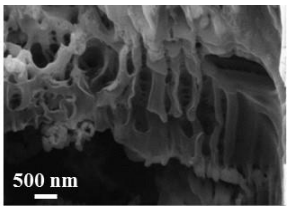
Surface image	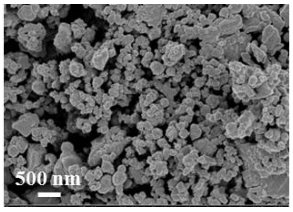	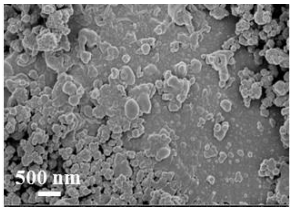	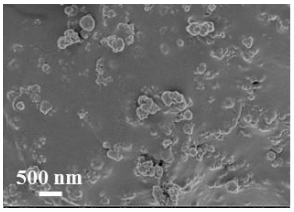

Figure 35. SEM image of copper patterns, cross section and surface image with different laser conditions

These observations are only limited to the top or few hundreds of nanometers from the surface. Laser penetration depth and film growth rate were compared to see the sintering effect through the depth direction. First, optical and thermal penetration depth were calculated for copper. Figure 36 shows the concept of optical and thermal penetration depth. Optical penetration depth is the depth where the photons reach. As the photon interacts with materials, heat propagates deeper [139]. Therefore, the thermal penetration depth is larger than the optical penetration depth. Optical penetration depth is calculated by

$$\delta_{optical} = 1/\alpha, \tag{1}$$

where α refers to the absorption coefficient [140]. For copper material, $\delta_{optical}$ is 14.6 nm. Thermal penetration depth can be modeled by

$$\delta_{thrmal} = \sqrt{4\kappa\tau}, \tag{2}$$

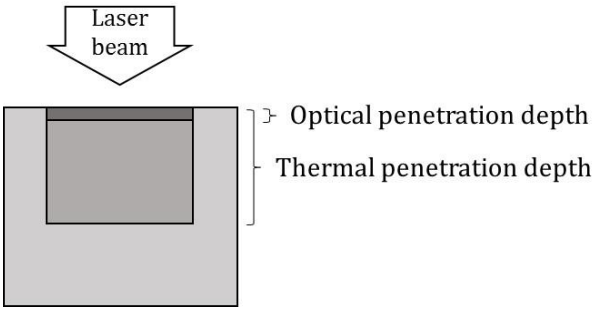

Figure 36. Optical and thermal penetration depth [139]

where κ and τ refers to a thermal diffusivity and pulse duration respectively [140]. For copper particle, the value of κ is 1.11×10^{-4} m^2/s and pulse duration in the process is 20 ns. Therefore the thermal penetration depth is 3 μm.

Afterwards, the film growth rate was calculated. It is assumed that the film only grows when the laser is irradiated and film growth rate is steady with time. To calculate the film growth rate, thickness of the film and the time that the area is exposed to the laser irradiation should be calculated first. Figure 37 shows discrete area to calculate the film growth rate. Size of the area and laser beam is drawn larger for understanding. Since the stage moves and the laser scans the substrate in the nozzle length direction, the laser exposure time of the discrete area is dependent on the laser scan speed and stage feed rate. Laser irradiation time is replaced with the number of laser scan in the discrete area. In the discrete area of 50× 50 μm^2, laser scans the area 10 times when the stage feed rate is 25 μm/s and laser scan speed is 50 mm/s. Figure 38 shows the measured thickness of copper patterns with different laser energy densities. Thickness of the film ranges from 15 to 30 μm with different laser energy densities. Therefore, the film growth rates are 1.5 ~ 3 μm/scan. These values are smaller than laser thermal penetration depth of copper with 20 ns laser pulse condition. Therefore, laser can affect through the whole area in the depth

direction. Afterwards, copper printed patterns were cut to the half with the cutter to observe the cross section to the bottom. Figure 39 shows the SEM image of the cross section of the whole film. Although slight scratches are observed in the cross section because of the shear stress applied by the cutter, same structures were observed inside the cross section. In addition, sintered particles were also observed near the substrate. Therefore, it can be concluded that particle sintering effect is consistent throughout the depth direction. This is because the NLP process uses laser while printing. Laser affects the whole printed area.

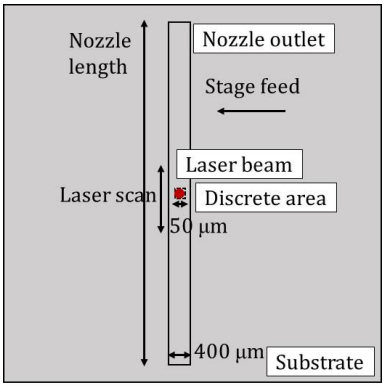

Figure 37. Calculation of laser irradiation number

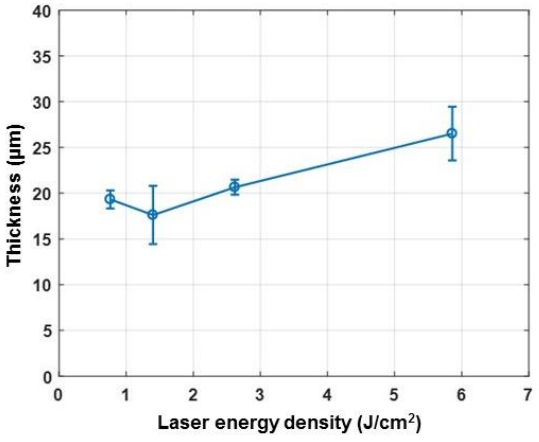

Figure 38. Thickness changes with respect to laser energy density

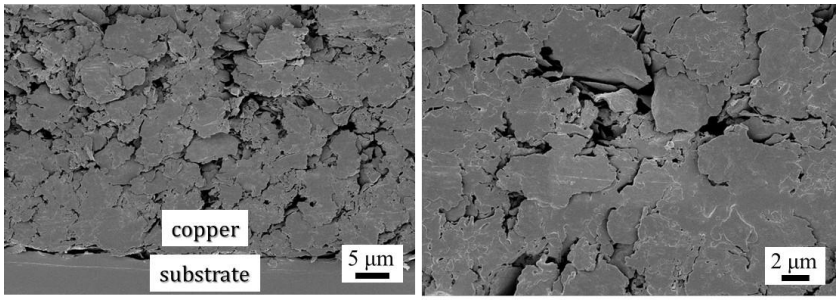

Figure 39. SEM image of cross section in depth direction

4.3.2 Composition

Thermal energy of the laser can change the phase or composition of the nanoparticles. XRD is a characterization method which detects crystalline structure using X-ray diffraction. By analyzing peak location and intensity, periodic atomic arrangement in the material can be analyzed. This is related to the material properties such as phase and composition. The change of composition with laser irradiation in the NLP process was measured with XRD. Figure 40 is the XRD results showing the oxidation degree with different laser energy densities. Oxidation degree changed with different laser conditions. When the patterns are printed with the laser energy of 0.31 and 0.76 J/cm^2, Cu and Cu_2O peaks are observed. With 1.40 J/cm^2 and 2.6 J/cm^2 laser conditions, CuO peaks appear. However, when treated with higher laser energy, Cu_2O peaks appear again. Normally, oxidation degrades the electrical property of the printed copper patterns. The copper particles are not completely oxidized even with the highest laser energy irradiation.

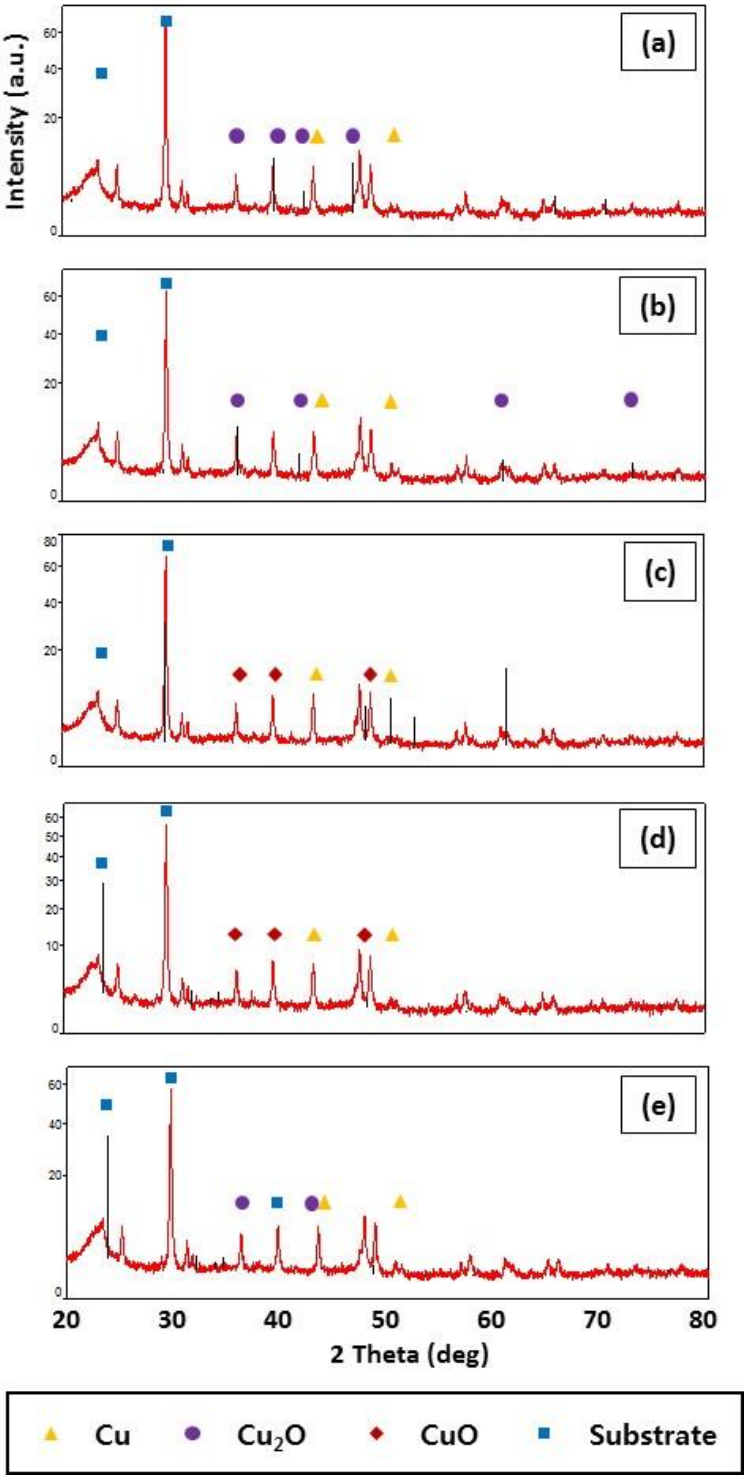

Figure 40. XRD results of printed copper patterns with different laser conditions, (a) 0.31, (b) 0.76, (c) 1.40, (d) 2.62, and (e) 5.86 J/cm^2

4.3.3 Particle recycle test

In the NLP process, nanoparticles are printed in the whole area and only the particles with the laser irradiation remain after the cleaning process. Since the particles are also printed in the undesired area and removed afterwards, it can be regarded as a waste of material. This can also cause environmental issues. Therefore, chance for recycling removed particles was checked. XRD results of the removed particles were analyzed and compared with those of the initial particles. They were compared with raw particles as well as the particles which go through the printing process without laser treatment. Figure 41 shows the composition of the raw and removed nanoparticles. Results showed that removed nanoparticles show the same peaks as those of raw particles or particles without laser treatment. The printing process itself without laser treatment only applies physical energy. Therefore, composition of the nanoparticles does not change. In addition, it can be assumed that laser effects on the flying particles and on the area near the laser irradiation are negligible in this process. These results showed the possibility for particle recycle because the recycled particles have the same compositions as the initial particles.

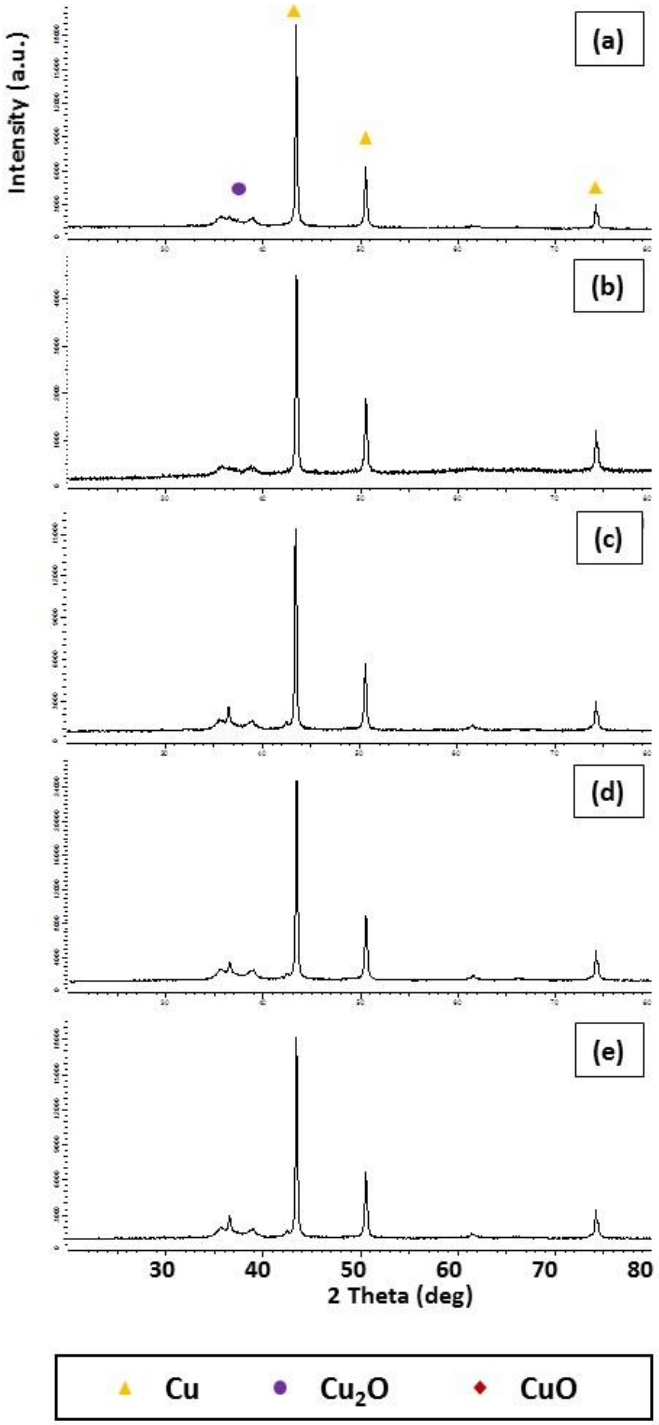

Figure 41. XRD results of recycled particles with different laser conditions (a) Raw particle, (b) 0 J/cm^2, (c) 1.40 J/cm^2, (d) 2.62 J/cm^2, and (e) 5.86 J/cm^2

4.4 Process-structure-property relationship

Process parameters affect the structure of the printed results as discussed in Section 4.3. Specifically, different laser energy levels change the porosity of the printing. These structural changes are related to the electrical and mechanical properties of the printing by changing the contact area and the distance between the particles. Therefore, the process-structure-property relationship needs to be studied. In Section 4.4.1, electrical properties of the deposited patterns and their changes with bending and folding are analyzed with different laser energy densities. In Section 4.4.2, mechanical property of the printed patterns will be analyzed. Cracks after the cycle test are observed.

4.4.1 Electrical property

Electrical property of the printed line was analyzed. Resistivity was calculated as

$$R_0 = R\frac{A}{L}, \tag{3}$$

where R_0 is the resistivity, R is the resistance. A and L is the area of the cross section and the length of the line respectively. Resistance of the copper and silver printed line was measured with an ohmmeter and cross section geometry was measured with a confocal spectroscopy. Figure 42 shows the results of the confocal spectroscopy. The cross section of the printed line shows triangular shape and the area can be calculated with the geometry. Figure 43 shows the calculated resistivity with different levels of laser energy. As a laser energy density increases, resistivity decreases in both silver and copper printed lines. This is because of a porosity difference. As the laser energy density increases, porosity decreases

as shown in Figure 35. Therefore the contact area between particles is large resulting in low resistivity.

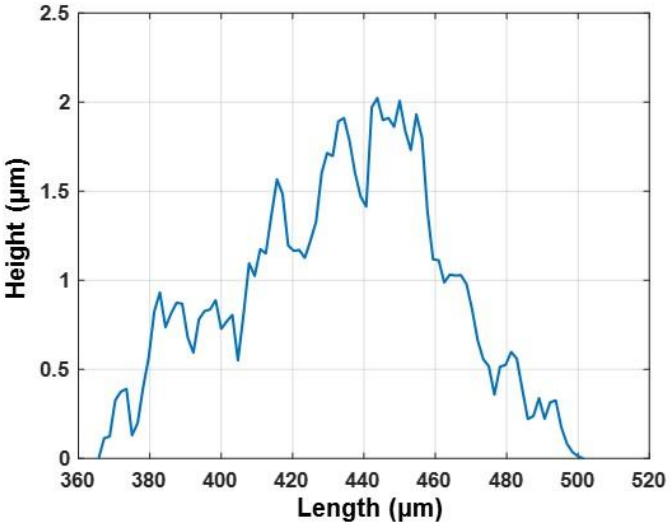

Figure 42. Cross section geometry of silver conductive line

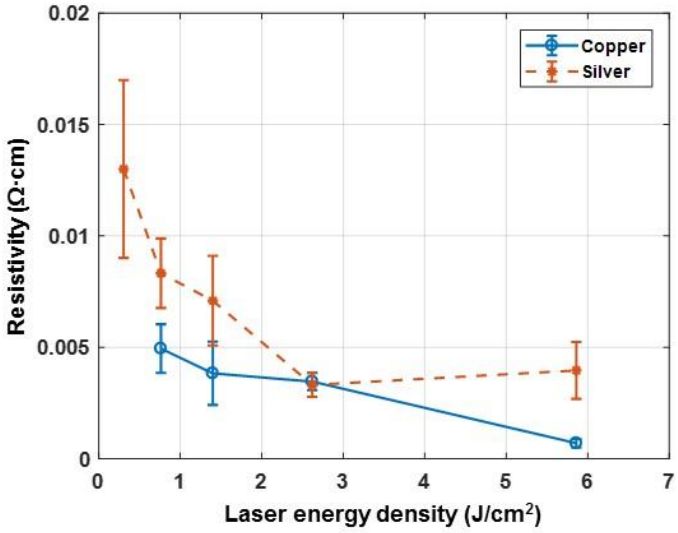

Figure 43. Resistivity with different laser energy densities

For flexible electronics, electrical property with bending and folding is important. The resistivity with different radius of curvatures and bending directions were measured and analyzed with different laser energy density levels. Copper nanoparticles were printed as a line with 8 mm× 1 mm size on PET substrate. The conductive wires were connected with a silver paste at the end of the printed line. After the silver paste is completely dried, UV cure adhesive sealant (UV-5500, Skycares Inc., Korea) was coated on top of the conductive lines and silver paste. After curing, the UV resin can prevent the damage on the printed sample from external force or contact. All the samples with bending and folding tests shown in Section 4.4 were packaged with these methods. Figure 44 shows the hardware setup for the bending test. The sample was fixed in the stage and the stage was moved in x-axis direction for bending motion. The stage traveled for the distance of 2000 μm with the velocity of 100 μm/s. After each loading and unloading, 500 ms was posed for stabilization. The bending was repeated 100 times. Charged coupled device (CCD) camera was located in y-axis direction to observe the bending curvature of the sample. Data acquisition (DAQ) device (NI USB-6009, National Instruments Corporation, USA) or source meter (Keithley 2450, Keithley Instruments, USA) was used to gather resistance data. The 4 terminal sensing method was used as illustrated in Figure 45 to reduce the measurement error from the 2 terminal sensing. Figure 46 shows the normalized resistances with different radius of curvatures. Three different samples were tested and averaged values as well as error bars are marked on the graph. As the radius of curvature decreases, resistance increases. This is because distance between the particles gets further with larger bending and the electrons are hindered from moving freely. The copper line printed with 1.40 J/cm^2 laser treatment shows the change in the normalized resistance from 1 to 1.75,

whereas the copper line printed with 5.86 J/cm^2 laser treatment shows the change from 1 to 1.5. The change in the resistance of the sample printed with higher laser energy irradiation was relatively small. This is because it has lower porosity. The change in the distance between the particles is smaller in the sample with low porosity. Therefore, it is less sensitive to bending. It can be concluded that change rate of resistance with bending can be controlled by laser conditions by varying porosity. As a result, the performance of the strain sensor can be designed and controlled.

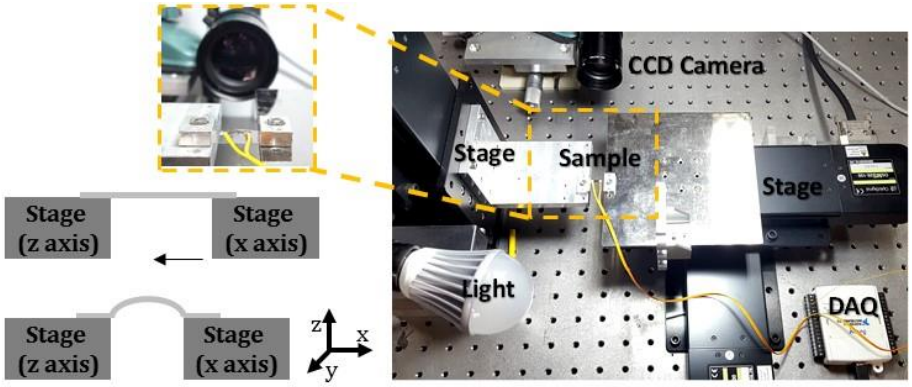

Figure 44. Hardware setup for bending test

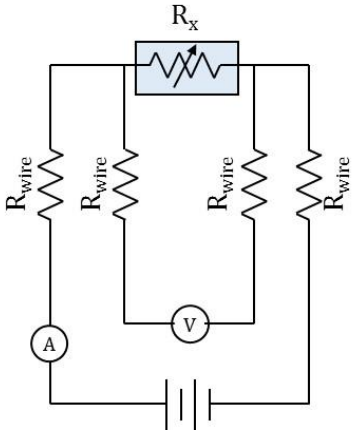

Figure 45. Bending test with 4 terminal sensing

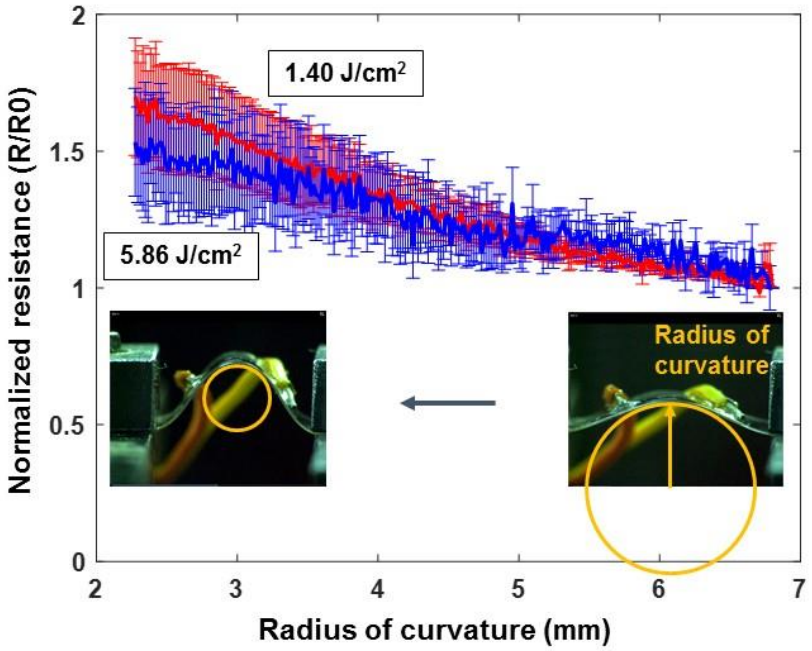

Figure 46. Normalized resistance with different radius of curvatures

Figure 47 shows the optical image of the bending test with different bending directions. Convex and concave bending was tested. Figure 48 is the result of the convex and concave bending. The resistance is related to the the distance between particles as discussed earlier. Contrary to convex bending, the particles get closer in concave bending and the resistance decreases. In both convex and concave bending, resistance change of copper line printed with higher laser energy density is less sensitive to the bending. Therefore, patterns printed with high laser energy density can endure wide bending range with constant resistance. It can be used for the printed circuit applications or strain and pressure sensors which require wide sensing range. On the other hand, electrical property of the patterns printed with low laser energy density is sensitive to bending. Therefore, it is suitable for sensible sensor applications.

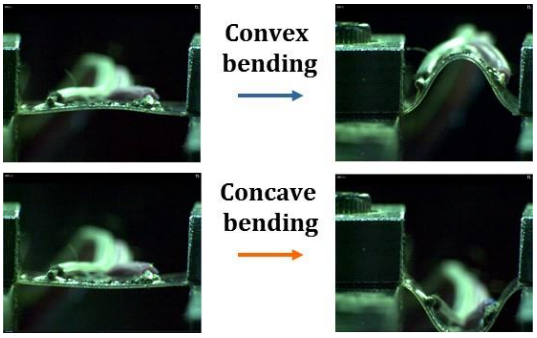

Figure 47. Bending test of different bending directions

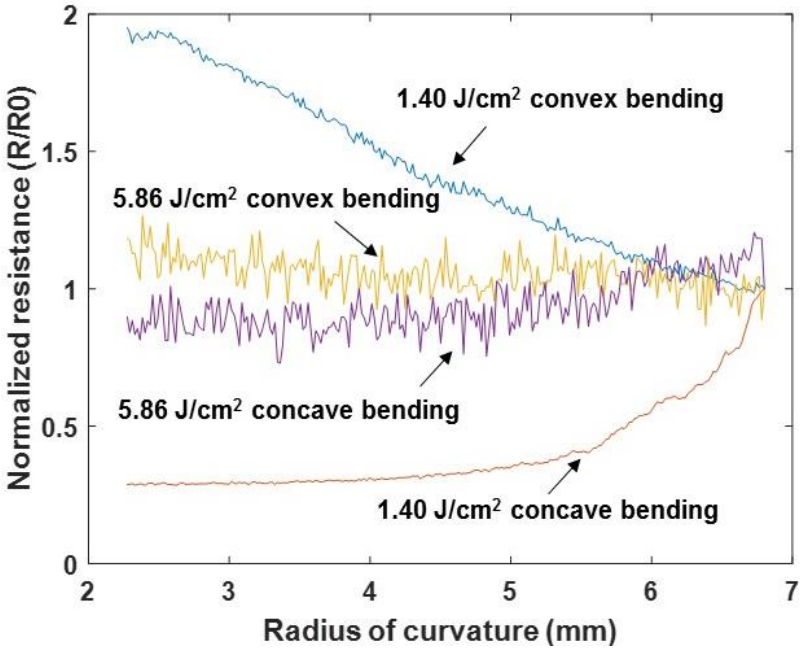

Figure 48. Normalized resistance with different bending directions

Conductance of the silver patterns printed on paper with folding was tested. Figure 49 shows the circuit design and hardware setup for the folding test. A light emitting diode (LED) is used to check the conductance. Voltage was 5 V and R1 was 1000 Ω. R2 is the resistance of the silver patterns and the value varies with the folding motion. Conductance of the silver line printed with low and high laser energy density was compared with different folding degree by observing the LED. Compared to the bending motion which the

distance between the particles in the whole area changes, folding only happens in the certain area but the distance between particles changes more drastically. Folding can be regarded as the bending with a small radius of curvature. Figure 50 shows the results of the folding tests. The silver line printed with low laser density was not conductive with 180° folding, whereas the line printed with high laser density was conductive with 180° folding. However the brightness of the LED decreased which means that the resistance has increased in a large order. Figure 51 shows the results for the folding with the different directions. Similar to the convex and concave bending discussed earlier, outer folding refers to the direction that the average distance between the particles gets larger, whereas inner folding refers to the direction that the particles get closer. In case of inner folding, both samples were conductive with 180° folding. However, the brightness of the LED with the sample printed with low laser energy decreased. It is shown that sensitivity of conductivity change with folding is also related to the porosity which is controlled by laser energy level. Figure 52 and Figure 53 show the results for the repeated folding tests. This test was conducted with the silver line printed with high laser energy to investigate whether it is conductive even with the repeated folding tests. With three times repeated folding tests, the results were the same.

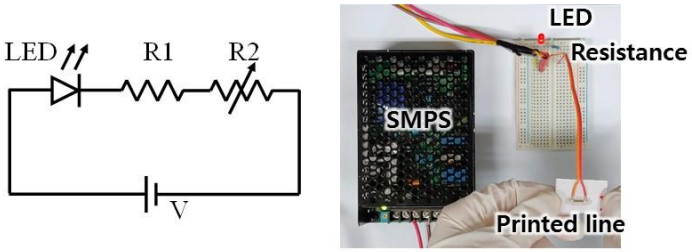

Figure 49. Experiment setup for folding test

Folding degree / Laser condition	0°	90°	180°
	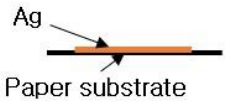		
Low laser (1.40 J/cm^2)	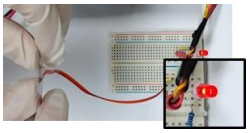	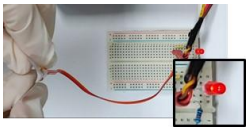	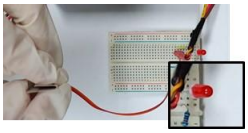
High laser (5.86 J/cm^2)	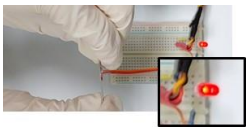	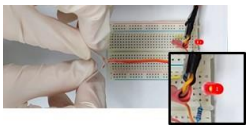	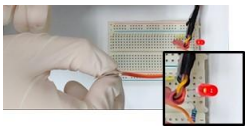

Figure 50. Folding test results: Outer folding

Folding degree / Laser condition	0°	90°	180°
	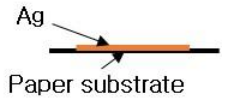		
Low laser (1.40 J/cm^2)	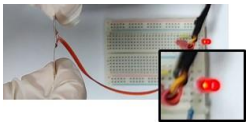	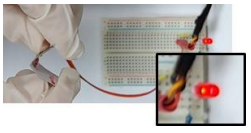	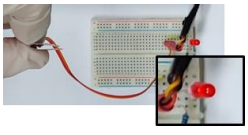
High laser (5.86 J/cm^2)	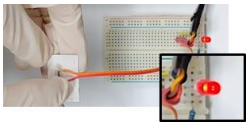	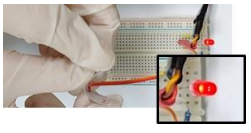	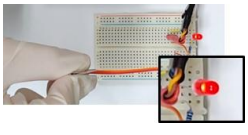

Figure 51. Folding test results: Inner folding

Folding degree / Number of repeat	0°	90°	180°
1	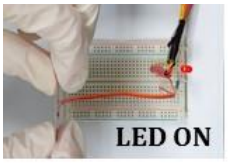	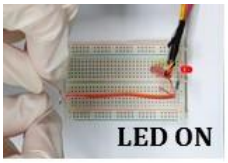	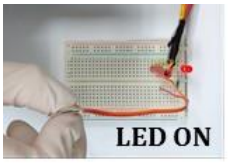
2		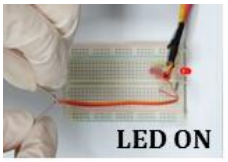	
3			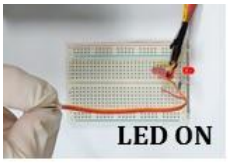

Figure 52. Folding repeat test: High laser power, outer folding

Folding degree / Number of repeat	0°	90°	180°
1	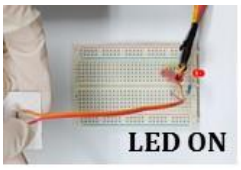	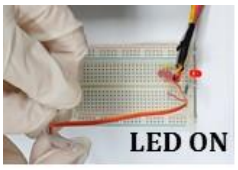	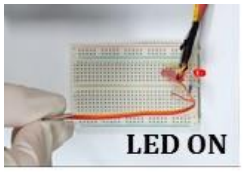
2	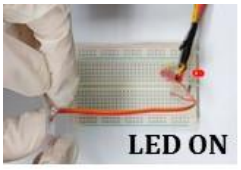		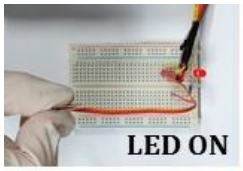
3		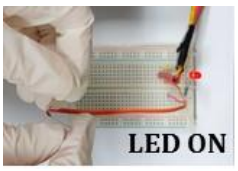	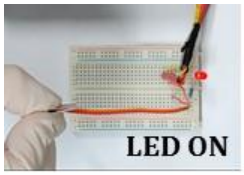

Figure 53. Folding repeat test: High laser power, inner folding

4.4.2 Mechanical property

Mechanical property was evaluated with a cycle test. Change of resistance with repeated number of bending was tested. Resistance changes with 100 times bending were measured. Figure 54 shows the results of the cycle test. Resistance change was stabilized after 70 number of bending in the low laser irradiated sample. Therefore, as a sensor application, 70 times bending can be performed as an aging process. After the aging process, the same performance within the error of 3.6 % is expected. In the high laser irradiated sample, performance was stabilized after 45 number of bending and the resistance was constant afterwards. Gauge factor was calculated as

$$Gauge\ factor = \frac{\Delta R/R}{\Delta L/L}, \tag{4}$$

where ΔR is resistance change and $\Delta L/L$ refers to the strain. Figure 55 shows the strain with bending. Strain value was calculated with

$$\varepsilon_m = \frac{b}{a}, \tag{5}$$

$$\varepsilon_x = -\frac{y}{b}\varepsilon_m, \tag{6}$$

where ε_m is a maximum strain at the cross section, a is the radius of curvature, b is the location of the neutral axis, and y is the distance of the measured point from the neutral axis. Maximum strain value was 0.03. Gauge factor was 2.01 and 0.31 for low and high laser irradiated sample respectively.

Figure 56 shows the SEM images of the cracks in the copper printed patterns with low laser irradiation after 100 bending tests. Multiple cracks are observed vertical to the bending direction because of strain. Since the NLP process uses raw particles without binder and the process temperature is low, the density of the structure is low compared to other processes. The structures are vulnerable to the deformation and cracks are easily formed.

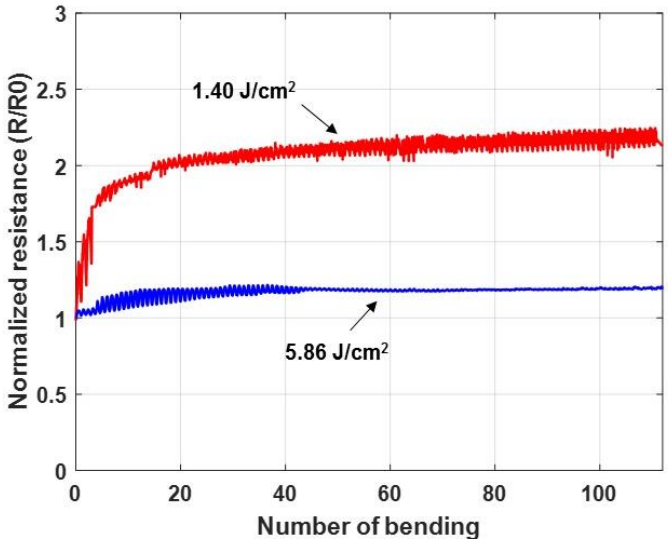

Figure 54. Cycle test

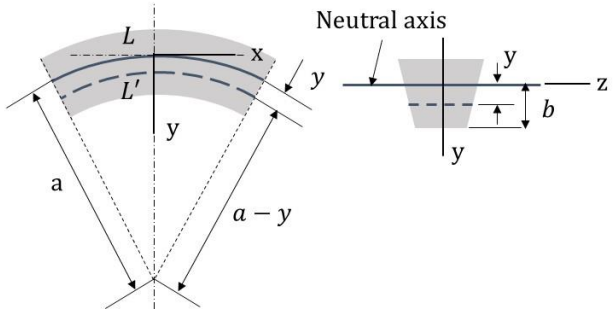

Figure 55. Strain with bending

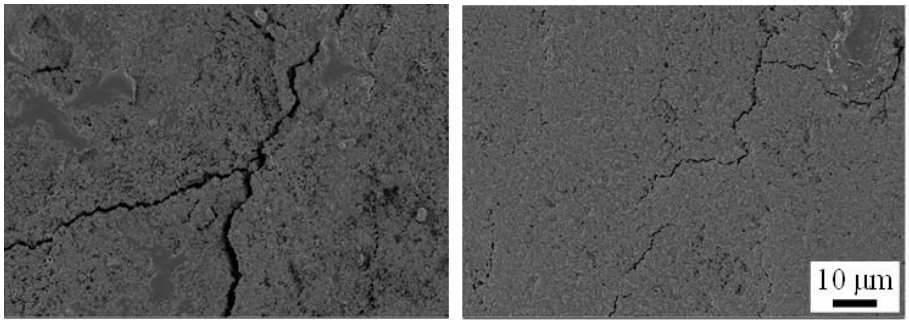

Figure 56. SEM image of crack after 100 bending test

To analyze the crack initiation, resistance change with cycle test was observed carefully and it was found that the change of the resistance is significant in the first several number of bending. Resistance changes with the first three times of bending were observed separately. Figure 57 shows the results of the normalized resistance with the repeated bending tests for three times. As marked with circles, the second derivative of the graph is positive in the first bending, whereas it is negative from the second bending. This means that crack is initiated from the first bending. In addition, difference between the maximum and minimum resistance increases with repeated bending motion in the low laser irradiated sample. This is because cracks propagate in the initial stage. However, difference between the maximum and minimum resistance is similar with repeated test in the high laser irradiated sample. This is because the structure is more stable with lower porosity. Figure 58 shows the gauge factor with different number of bending. Gauge factor is in the range of 20 ~ 50 depending on the laser condition and the number of bending in the initial stage. After the crack stabilization, gauge factor converges to 2.01 and 0.31 respectively. 70 and 45 number of repeated tests are needed for crack stabilization in low and high laser energy irradiated sample as discussed earlier. The sample with high laser energy irradiation began to stabilize more quickly.

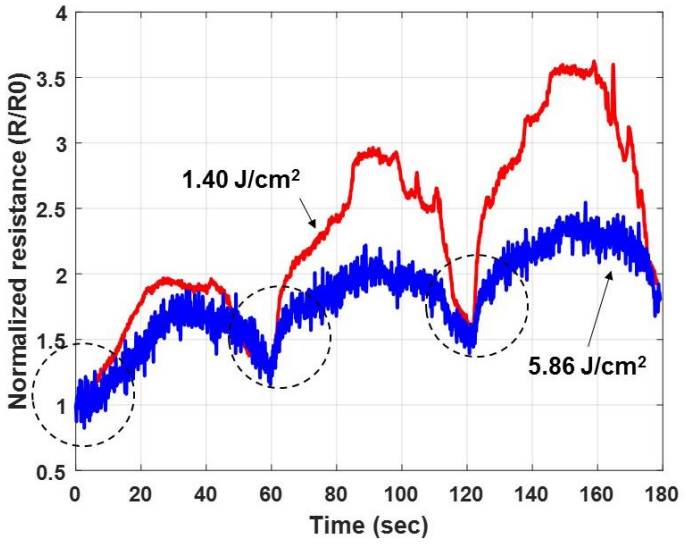

Figure 57. Resistance change with loading and crack initiation

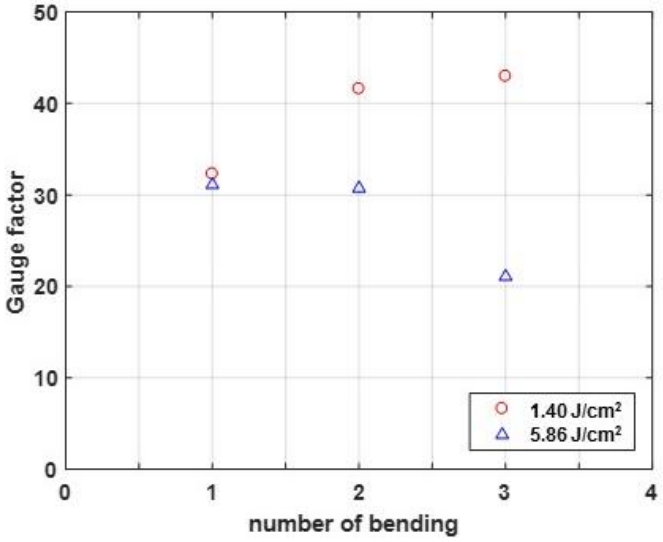

Figure 58. Gauge factor with number of bending

In summary, in the NLP process, laser conditions affect the properties of the printing. Laser process can change two main characteristics: chemical composition and morphologies of the printed structures. The changes of physical properties are related to the variation of chemical composition. For example, wettability changes along with different oxidation degrees of copper. Electrical conductivity also varies by the oxidation levels of metal particles. These changes are only dependent on the material selection. In this research, our focus is on morphological changes. Laser can control the porosity of the deposited structure in the NLP process. The process-structure relationship can be built by systematic characterization and quantification of structures. With high laser energy irradiation, because of the sintering effect, porosity of the printing decreases and a denser structure is formed. In this research, SEM image is used to compare the porosity of the structure qualitatively. Quantitative analysis is needed to build the relationship between the quantified porosity and electromechanical properties. Here, porosities were measured with image processing as shown in Section 5.3. The image processing approach includes bias and errors because the measurement is dependent on the light condition. In addition, the analysis is limited to the small area which cannot always represent the whole structure. Therefore, bias is inevitably included. The Brunauer-Emmett-Teller (BET) method uses gas absorption to study surface area including the pore size distribution. However, this method is limited to open pore measurement. There are other methods developed to study the porosity of structures. For example, the Kelvin equation can be applied to measure total pore volume. BJH and Dollimore-Heal methods can calculate volume, area, and distributions of mesopores [141].

With a high level of laser energy, porosity of the structure decreases. If the number of holes within the structure decreases and the diameter of the neck between particles increases, the averaged mean free path of the electrons increases. This results in low resistance. Table 6 shows the selected examples of conductive copper electrodes fabricated with various methods and their resistivity values [142]. Resistivity of the copper patterns printed with the NLP process is higher than that of other processes. The resistivity can be further reduced. For example, higher laser energy which does not damage the flexible substrate can be used. In addition, oxidation degrades the electrical properties. Oxidized printed patterns can be reduced with flashlight sintering process. Furthermore, laser effect on different substrate materials needs to be explored. There is a possibility that particles are embedded on the porous paper. These embedded particles can affect the properties. This effect needs to be characterized and compared with the denser PET substrate.

Table 6. Selected examples of the resistivity of conductive copper electrode fabricated with various methods [142]

Materials	**Method**	**Resistivity (μΩ·cm)**
Cu nanoparticle	Ink jet	20
CuO	Laser reduction	31
$Cu(OH)(NO_3)/Cu(NO_3)_2$	Laser reduction	240
$Cu(OH)PO_4$	Laser direct structuring	9.18
$Cu(OH)_2$	Intense pulsed light	5.27
$Cu(OH)(NO_3)$	Intense pulsed light	125.1
CuO	Intense pulsed light	10
Cu particle	Flash light sintering	80
Cu nanoparticle	**NLP process**	**693**

The properties with bending and folding were analyzed. If the strain is applied in the direction that the distance between the particles gets further, resistance increases. When the structure is deformed and strain is applied, cracks occur. Especially, since the NLP process is a dry particle deposition process with a low level of laser energy, the structure is not dense. Therefore, cracks are easily generated. Cracks can be used as a working principle of a strain sensor by controlling the contact area between the particles with bending and folding. In the early cycles, cracks are not fully propagated, therefore the sensor performance is not stabilized. If the cracks are fully developed and stabilized with more cycles, steady performances are expected. More systematic characterization of fracture needs to be conducted to study the nonlinear relationship between effective strain and resistance. For example, cracks with the repeated number of bending can be observed to understand the crack propagation process. Cracks need to be quantified and compared between the printed patterns with different laser conditions. The change of resistances is less sensitive to the bending and folding cycles in the high laser energy irradiated sample. This knowledge can be utilized to design and characterize flexible electronics with the process. To use the printed patterns as commercial flexible electronics, more experiments need to be done to verify the performances accurately. For example, the gauge factor can be calculated with different radii of bending, speeds of loading, and the thickness of the film and the substrate. A larger number of cycles can be tested to evaluate the life expectancy of the electronics. The effect of temperature and humidity on the performance can be tested.

Moreover, when analyzing the electrical property with bending and folding, UV resin was used for packaging. Strictly speaking, it is the property of the metal-polymer

composite that was measured. Polymer can work as a damper material when deformed, and life span of the flexible electronics can be extended by protecting particles from the outside. However, the electrical property is different from that of the pure metal printing. Tradeoff between the reliability and the performance can be studied and considered when designing flexible electronics. In addition, other electromechanical properties can be measured and quantified to complete the process-structure-property relationship. For example, conductivity of the printed circuit can be quantified. Not only the porosity but also the hardness, modulus of elasticity, and tensile strength of the printed film can be measured by nano indentation. These structural properties can be linked to electromechanical properties as well.

CHAPTER 5. PROCESS MODELING AND ANALYSIS

To help establish the process-structure-property relationship in the developed printing process, a multiscale framework to model the nanoparticle deposition is developed. An analytical adhesion model predicts the deposition based on process parameters including laser irradiation, temperature, and particle size, as well as the mechanical properties of particles. The mechanical properties of nanoparticles are predicted by molecular dynamics simulations to construct the structure-property linkage at atomic scale. A controlled kinetic Monte Carlo simulation model is developed at mesoscale to build a process-structure relationship to predict the morphology of the printed film. In this chapter, the developed multiscale framework is described. In Section 5.1, an overview of the framework is provided. In Section 5.2, multiscale model combining analytical and MD model is studied to elucidate the deposition mechanism of the process. In Section 5.3, morphological change of the printed patterns with different process parameters is analyzed with the cKMC model.

5.1 An overview of the multiscale framework

Understanding the deposition mechanism of aerosol jet printing is important to fully control the process. They are studied with analytical model and computational tools to allow engineers to predict the behavior of products and performance of manufacturing process. Many researchers studied the deposition mechanism with analytical model, FEM, and MD model as discussed in Section 2.3. Most of the studies do not consider thermal energy which is essential for the NLP process. Some of the studies include thermal effects. But they are dealing with high temperature including the melt pool.

To study the deposition mechanism with thermal effect, an analytical model and a MD model are combined into a multiscale model. Laser condition and particle size are the main factors for deposition in the NLP process, as verified in experiments. With low laser power, particle deposition is not successful. However, high laser power results in substrate damage. In addition, it was found that particles with the size of 5 μm or above tend to rebound and no pattern can be generated. For smaller particles of diameter under 100 nm, they can be deposited under certain laser conditions. This scale effect is usually attributed to the large surface-to-volume ratio of small particles and more efficient laser energy absorption. Here, the scale effect of particles is examined by analytical and simulation models. In addition, kinetic energy is different with different particle sizes. Kinetic energy is an important factor in the particle impact model.

The proposed multiscale adhesion model is shown in Figure 59, where information is exchanged at different length scales. The diameter of nanoparticles is similar to the laser wavelength. Temperature change of the particle itself is difficult to measure. Therefore, the

analytical model of laser-nanoparticle interaction proposed by Pustovalov *et al.* [143] was used to estimate temperature change. In this model, heat capacity and absorption factor are important, which are also dependent on the size of particles. With temperature as an input, the elastic-plastic properties of particles with different temperatures are predicted with MD simulations as a structure-property analysis. For particles, these properties are also dependent on the particle size. With the mechanical properties of substrate and particles, along with temperature, particle size, and other process parameters, deposition can be predicted with an adhesion model with classical particle impact and bonding.

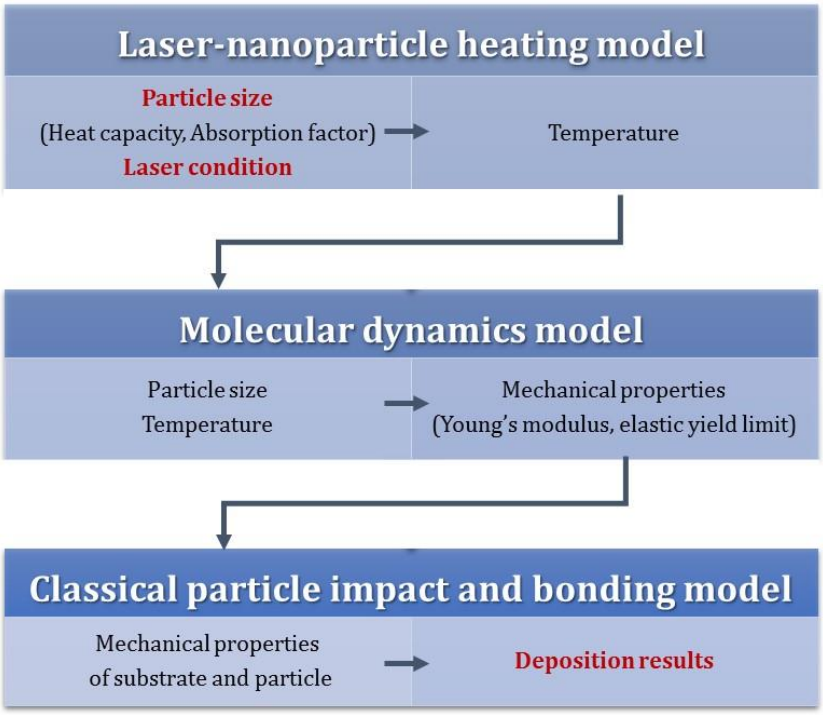

Figure 59. The proposed multiscale adhesion model

The application procedure of the developed multiscale adhesion model is described in Figure 60. In the analytical adhesion model, the concerned parameters are material properties such as mass, density, as well as mechanical properties of particles and the substrate. Process parameters such as velocity of the particle are also needed. Elastic-plastic properties such as Young's modulus, Poisson's ratio, and the elastic yield limit are dependent on temperature of the particles and substrate which can be controlled by laser conditions. In this study, the temperature change of the substrate was measured by an IR camera and its properties with respect to different temperatures were found from the literature. In addition, the effect of laser on nanoparticles is studied.

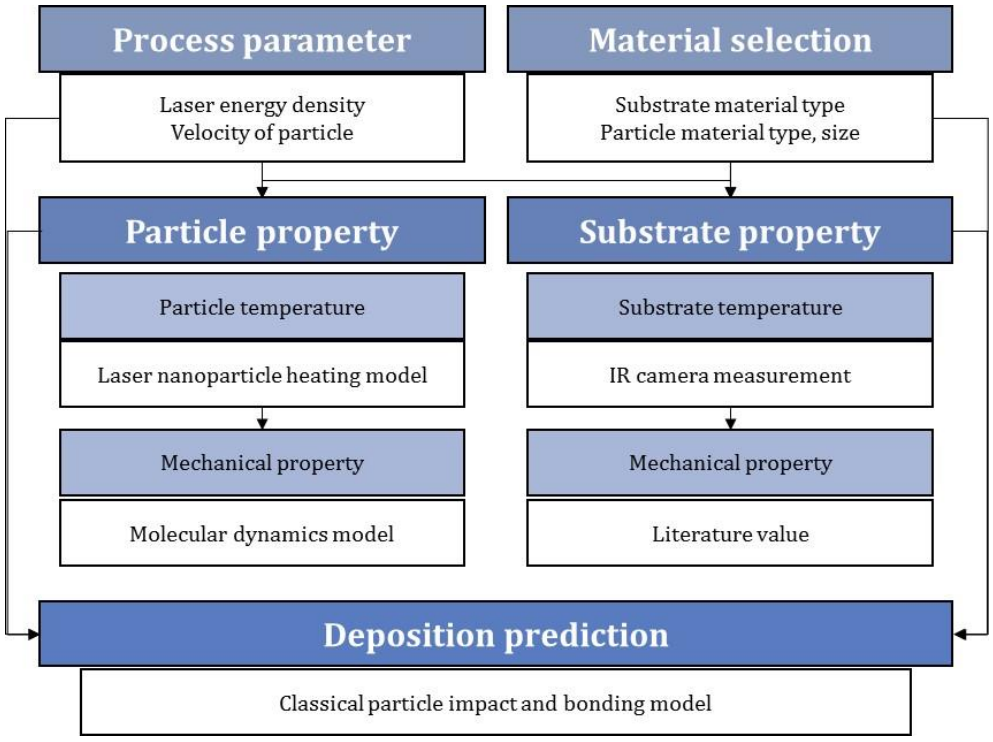

Figure 60. Process flow for deposition mechanism model

The introduction of laser changes the morphologies of the printed film. The adhesion model for aerosol deposition is normally limited to single particle analysis. The prediction of morphological changes requires a model at a much larger scale. In addition, laser affects particles throughout the particle flow from the beginning of the nozzle to the substrate. The timescale of laser irradiation is few milliseconds, and the thickness of the printed patterns is in the scale of micrometer. Simulation models which can predict larger sizes and longer timescale than molecular dynamics are needed. To predict the morphology of deposition results, a controlled kinetic Monte Carlo model of deposition is developed to study the morphologies of printed films with laser irradiation. The process-structure relationship at the mesoscale can be established with this model.

5.2 Deposition mechanism

5.2.1 Classical particle impact and bonding model

Figure 61 illustrates the particle impact model for deposition. Since particles go through the elastic and plastic deformation during the impact on the substrate, the adhesion of a particle to a solid surface was analyzed with the theory of Rogers and Reed [66]. When small particles impact, the kinetic energy is converted to the elastic energy. If the stress exceeds the elastic yield limit of the softer material between particle and substrate, plastic deformation happens and energy is lost. In the restitution process, if the stored elastic energy of a particle is smaller than the total adhesive energy, the particle will be deposited. Otherwise it will rebound.

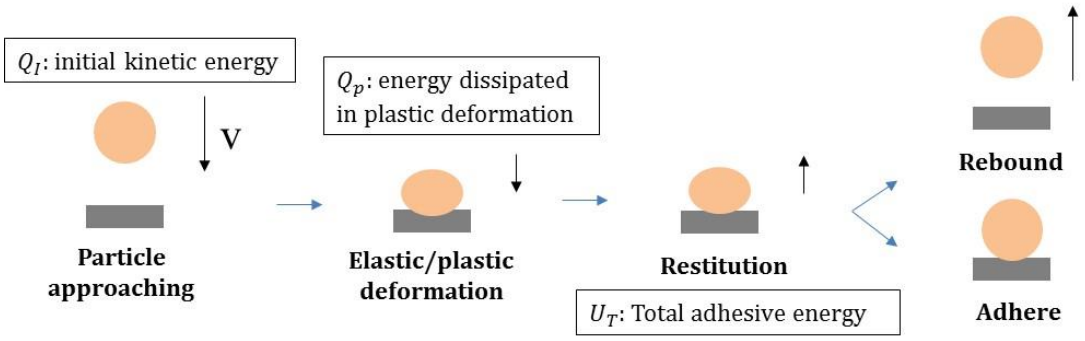

Figure 61. Particle impact model for deposition

The initial kinetic energy Q_I and energy stored as plastic deformation Q_p can be calculated based on

$$Q_I = \frac{1}{2}mv^2, \tag{7}$$

$$Q_p = \left(\frac{(2mv^2 - \frac{1}{8}m\varphi^2)^{1/2} - (\frac{15}{8}m\varphi^2)^{1/2}}{2} \right)^2, \tag{8}$$

respectively, where

$$\varphi = (\frac{2\pi}{3K})^2 \left(\frac{2}{5\rho}\right)^{1/2} Y^{5/2} \tag{9}$$

is the limiting elastic velocity. ρ, m, and v are the density, mass, and velocity of the particle respectively, Y is the elastic yield limit of the softer between the two bodies, and

$$K = 4/[3\pi(k_1 + k_2)] \tag{10}$$

is an effective elastic modulus where

$$k_i = (1 - {\nu_i}^2)/(\pi E_i), \tag{11}$$

ν_i is Poisson's ratio, and E_i is Young's modulus of each body ($i = 1, 2$). Therefore, the remaining energy when the particle is in the stage of restitution is $Q_I - Q_p$.

$$U_T = U_M + U_S \tag{12}$$

is a total adhesive energy between the particle and the substrate, which is the sum of the mechanical energy U_M and surface energy U_S. The mechanical energy U_M and the surface energy U_S can be calculated based on

$$U_M = P_0 \frac{\left({P_1}^{2/3} + 2P_0{P_1}^{-1/3}\right)}{3K^{2/3}{R_c}^{1/3}}, \tag{13}$$

$$U_s = \Delta\gamma\pi\left(\frac{R_c P_1}{K}\right)^{2/3}, \tag{14}$$

respectively, where P_0 is the external force applied to the contacting bodies, which is normally a gravitational force. P_1 can be calculated as

$$P_1 = P_0 + 3\Delta\gamma\pi R_c + \left[(P_0 + 3\Delta\gamma\pi R_c)^2 - {P_0}^2\right]^{1/2}, \tag{15}$$

where $\Delta\gamma$ is the surface energy per unit area, and R_c is the contact geometry parameter. This can be calculated as

$$R_c = \frac{K({r_e}^2 + {r_p}^2)^{3/2}}{\pi {r_p}^2 Y + r^{1/2} K(5m\varphi^2/4r^{1/2}K)^{3/5}}, \quad (16)$$

where r is a radius of the particle. r_e and r_p are the projected radii of elastic and plastic deformation respectively.

The criteria whether the particle will adhere or rebound are

$$(Q_I - Q_p) < U_T\text{: Particles adhere} \quad (17)$$

$$(Q_I - Q_p) \approx U_T\text{: Particles remain on surface} \quad (18)$$

$$(Q_I - Q_p) > U_T\text{: Particles rebound.} \quad (19)$$

In order to calculate the values of Q_I, Q_p, and U_T, the elastic-plastic properties of the particle and substrate, which are dependent on the temperature, are calculated as described in Sections 5.2.3 to 5.2.5.

5.2.2 Temperature change of particles- Model of nanoparticle heated by laser

The temperature change of nanoparticles with laser irradiation is calculated analytically. The thermal energy of nanoparticles interacting with laser follows [143]

$$\rho c V \frac{dT}{dt} = \frac{1}{4} I_0 \alpha S - J_c S, \quad (20)$$

where ρ and c are the density and heat capacity of the particles respectively, V and S are the volume and surface area of the particles, T is the temperature, t is the time, I_0 is the

constant intensity of laser irradiation, α is the efficiency absorption factor, and J_c is the energy loss from heat conduction. If the heat capacity and efficiency of absorption are assumed to be constant with time, and heat conduction between particles and convection during time t can be ignored, then temperature changes of nanoparticles can be modeled by [143]

$$T = T_{\infty} + \frac{3I_0 \alpha t}{4\rho c r}, \tag{21}$$

where T_{∞} is the initial temperature and r is the radius of particles. Since it is difficult to measure the temperature of nanoparticle itself, theoretical and literature values are used for validation.

It has been reported that various properties of particles such as melting point, absorptivity, and thermal conductivity vary with different sizes [2, 144, 145]. In Equation (21), the absorption coefficient and specific heat capacity are dependent on the size of the particles. They were obtained from experiments. They were measured using differential scanning calorimeter (DSC) and ultraviolet-visible (UV-Vis) spectrophotometer respectively. Figure 62 shows the absorption coefficients of the copper particles with different particle diameters. Both types of particles show the largest absorbance near 355 nm wavelength. The exact values are $\alpha_{D=45} = 0.80$ and $\alpha_{D=0.1} = 0.98$. Figure 63 shows the DSC results with different particle size. Heating rate was 25 K/min. Copper particles with diameters of 5 μm and 0.1 μm show different DSC curves. In the DSC curve, a small decrease is the glass transition point. The highest peak, which corresponds to the crystallization process, is followed by a large decrease which is the melting point. In order

to analyze the specific heat capacity at room temperature, particles were analyzed in the temperature range of 0 to 50°C with the heating rate of 10 K/min. The specific heat capacities of the particles of diameter 5 μm and 0.1 μm are 1.52×10^2 J/kg·K and 1.05×10^3 J/kg·K respectively. Finally, the temperature change of the particle was calculated with Equation (21). Figure 64 shows the estimation of copper particle temperature with different laser conditions. The temperature of the copper particle of diameter 0.1 μm reaches 250°C with laser irradiation of energy level of 6 J/cm^2, whereas the temperature of 5 μm sized particle only reaches 50°C. These values are reasonable because the sintering temperature of copper particles is 200~500°C.

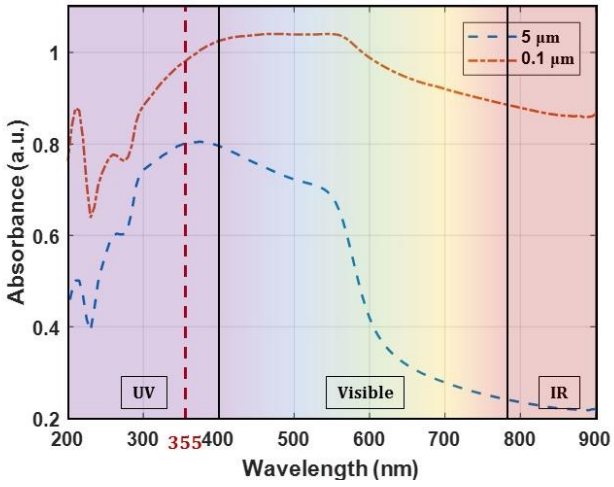

Figure 62. Absorption coefficient of copper particles

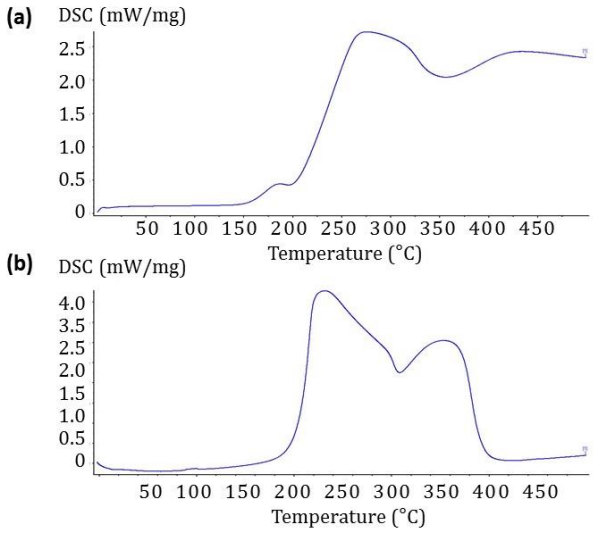

Figure 63. DSC results of (a) 5 μm and (b) 0.1 μm copper particles

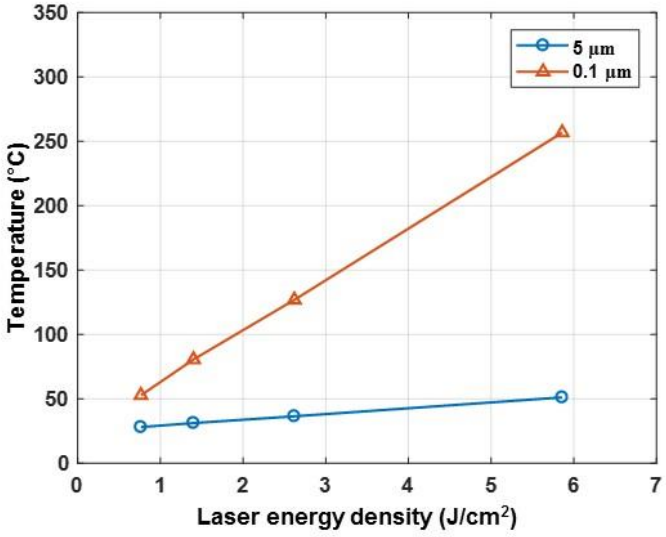

Figure 64. Estimation of copper particle temperature with different laser conditions

5.2.3 Mechanical properties of particles – Molecular dynamics model

MD model was built to estimate mechanical properties of nanoparticles with different sizes and temperatures. Mechanical properties of nanoparticles are difficult to be measured directly by experiments. If the interatomic potential is accurate and electron-phonon coupling effects are negligible, the results of MD simulations are reliable. Therefore, efforts were made to find accurate interatomic potentials. The embedded atom method (EAM) potential developed by Mishin *et al*. [146] which successfully modeled properties of various copper structures was used. The crystal structure of copper is a fcc structure with the unit cell length of 3.6 Å. In this model, a polycrystalline structure was modeled as opposed to a single crystalline structure. Figure 65 shows the comparison between the single crystalline and polycrystalline structures. Grain boundaries and defects are the important factors to be considered for estimating mechanical properties in the polycrystalline structure. The built structure was first relaxed for energy minimization. Afterward, uniaxial tensile properties such as Young's modulus and the elastic yield limit were calculated. During the uniaxial tension process, isothermal-isobaric condition was assumed.

Figure 66 shows the polycrystalline copper particle before and after uniaxial tension. Figure 67 shows the comparison of stress-strain curves of polycrystalline structure and single crystalline structure. If the particle is modeled as an ideal single crystalline structure, Young's modulus and the elastic yield limit are high.

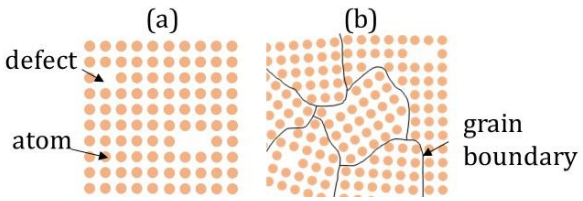

Figure 65. (a) Single crystalline and (b) polycrystalline structure

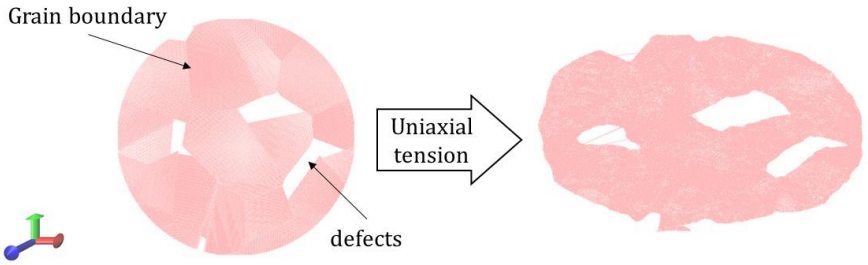

Figure 66. Polycrystalline copper particle before and after uniaxial tension

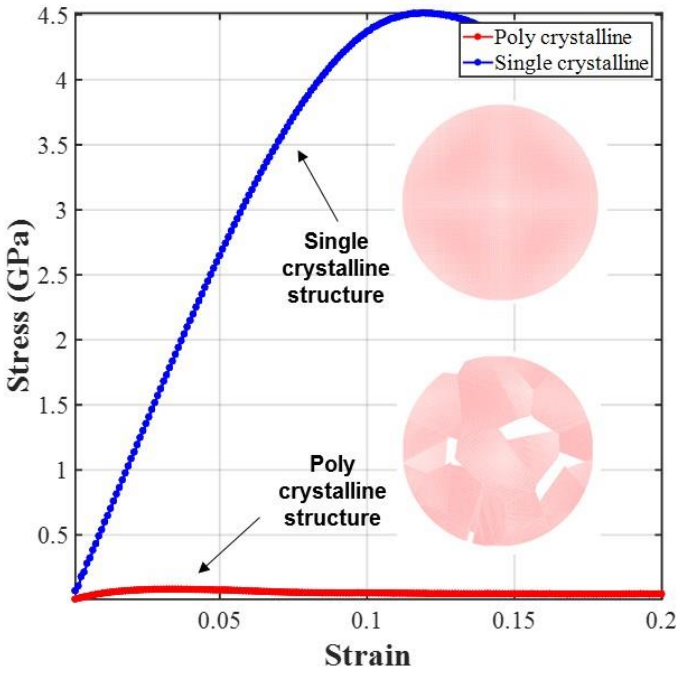

Figure 67. Stress-strain curve of single crystalline and poly crystalline copper particle

The particle temperature was changed to 300, 600, and 900 K. The temperature condition was changed by assigning the atomic velocity according to the temperature. The particle size was changed to 25, 50, and 100 nm. To model a particle with the diameter of tens of nanometers with MD, the computational cost is too high. The particle model was simplified to a disk shape with periodic boundary conditions in order to model bigger particles. Using periodic boundary conditions with simplified shape, the simulation cost was reduced considerably. Figure 68 and Table 7 show the results with different temperature conditions. The size of the particle was fixed to 100 nm. With a higher temperature, Young's modulus decreases slightly from 2.98 to 2.23 GPa and the elastic yield limit also decreases from 79 to 58 MPa. Figure 69 shows the stress-strain curves of different size of copper particles. The temperature of the particle was fixed to 300 K. With a smaller particle, Young's modulus and the elastic yield limit decrease. Table 8 shows the results. Young's modulus decreases from 3.03 to 0.19 GPa and the elastic yield limit decreases from 79 to 3 MPa.

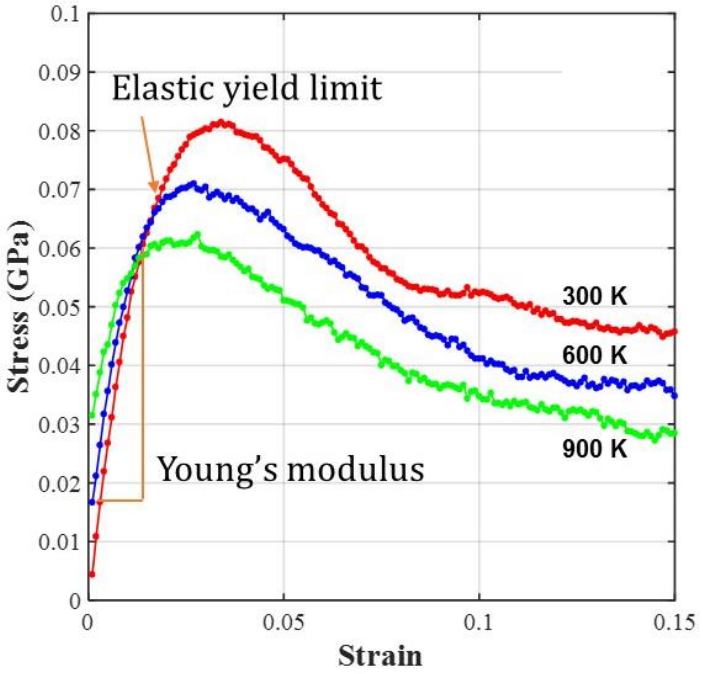

Figure 68. Stress-strain curve of different temperature of copper particle (particle diameter: 100nm)

Table 7. MD results of particle's mechanical properties with different temperature conditions

Temperature (K)	300	600	900
Young's modulus (GPa)	2.98	2.74	2.23
Elastic yield strength (MPa)	79	68	58

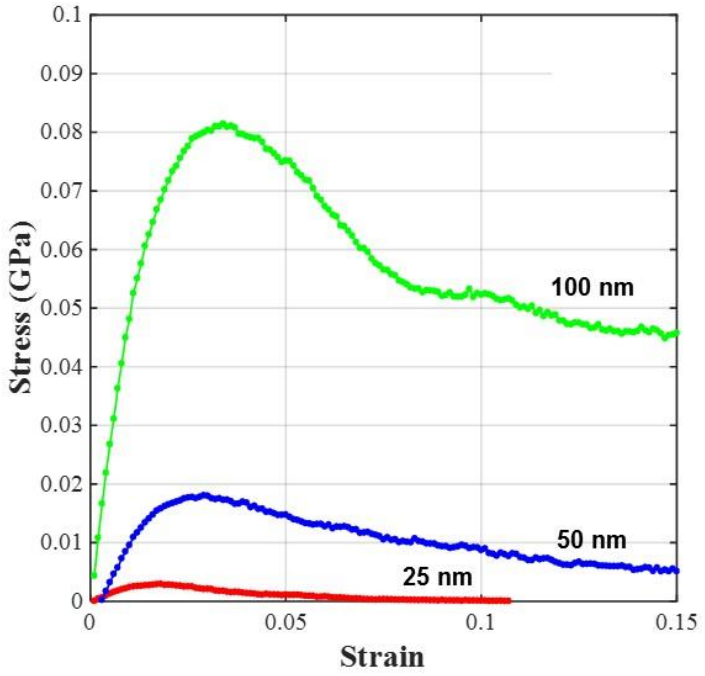

Figure 69. Stress-strain curve of different size of copper particle (particle temperature: 300 K)

Table 8. MD results of particle's mechanical properties with different particle size

Diameter of particle (nm)	25	50	100
Young's modulus (GPa)	0.19	0.85	3.03
Elastic yield strength (MPa)	3	16	79

To validate the model, results were compared with the experiment and simulation results from literature. It was difficult to find published results regarding mechanical properties with different temperature conditions in nanocrystalline copper structures. However, in bulk structures, experimental results show that Young's modulus and the elastic yield limit decrease as temperature increases [147]. Furthermore, the effect of particle size was also compared with experimental and simulation results. Table 9 shows the tensile test results from literature [148, 149]. These are results of specimens that are

machine cut from the nanocrystalline metal, prepared by powder metallurgy. The diameter of the powder is shown in the table. Although there were some differences in Young's modulus, the values of elastic yield limit were similar to those of MD results. Zheng *et al*. [150] studied the stress-strain curve of copper nanoparticles with MD simulation. Figure 70 shows the results. The copper nanoparticles of 4, 6, and 8 nm diameter size were analyzed. Young's modulus of the model was around 1.43 GPa when the particle size is 6 nm. However, they cannot predict the elastic yield limit of the particles. It is concluded that the MD model is reasonable because the predicted properties are in the same range as the data from the literature.

Table 9. Experimental results of copper mechanical properties of nanocrystalline metal from literature [148, 149]

	Micro (10 μm)	Nano (50 nm)	Ref.
Young's modulus (MPa)	484	484	[148]
Elastic yield strength (MPa)	170	385	
	Micro (50 μm)	Nano (25 nm)	Ref.
Young's modulus (MPa)	467	361	[149]
Elastic yield strength (MPa)	83	185	

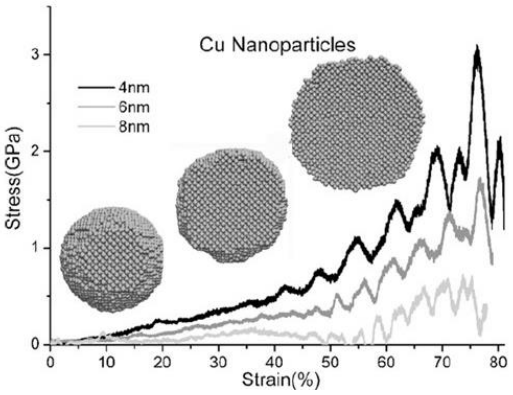

Figure 70. Simulated properties of copper nanoparticles by MD model [150]

Theoretically, if the crystal structures of the materials are same, Young's modulus should have the same values. In addition, the elastic yield limit should increase with a smaller grain size. If the grain size is smaller, the material contains fewer dislocation. Therefore, particles with smaller grains can endure more strain in the elastic range than the particles with larger grains. This is also known as the Hall-Petch effect given by

$$\sigma_y = \sigma_0 + \frac{h}{\sqrt{d}}, \tag{22}$$

where d is the diameter of the grain, σ_y is the elastic yield strength, and σ_0 and h are constant which are the material properties. In single crystalline structure, particle size is equal to the grain size. However, in polycrystalline structure, particles consist of several grains. The grain size is smaller than the particle size. If the grain size is smaller than a critical grain size which is 10 nm for most of the metals, the Hall-Petch effect will not work [151]. This is because smaller grains under 10 nm are unable to support the dislocation with strain. This is called the inverse Hall-Petch effect modeled as

$$\sigma_y = \sigma_0 + h\left[\frac{1 - P_{dis}}{d}\right]^{\frac{1}{2}}, \tag{23}$$

where P_{dis} is the probability of a dislocation being absorbed by the grain boundaries. However, this effect is difficult to observe by experiment. Figure 71 shows the Hall-Petch relationship for the copper material by several studies. Only the data marked as gray circles reported the inverse Hall-Petch relationship with the grain size of 16 nm [152]. Although the grain size is largely dependent on the manufacturing process, it is assumed that the grain size gets smaller with smaller particle size in this research. The grain size was around 15 nm in the model. Therefore, trend that the elastic yield limit decreases with smaller particle size can be explained with the inverse Hall-Petch effect. Figure 72 shows the effect of grain size on the mechanical properties simulated by this MD model. Even though the sizes of the particles are the same, if the grain size is smaller, the elastic yield strength is lower.

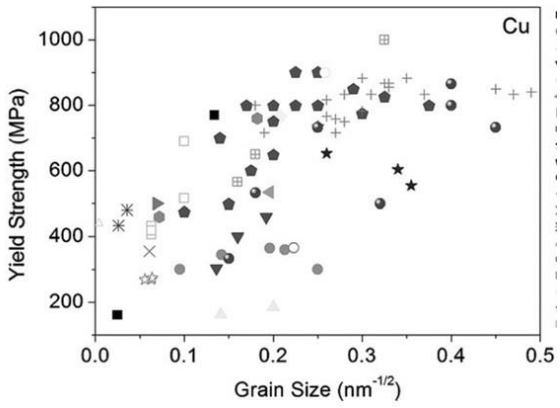

Figure 71. Hall-Petch relationship for copper by several studies [151]

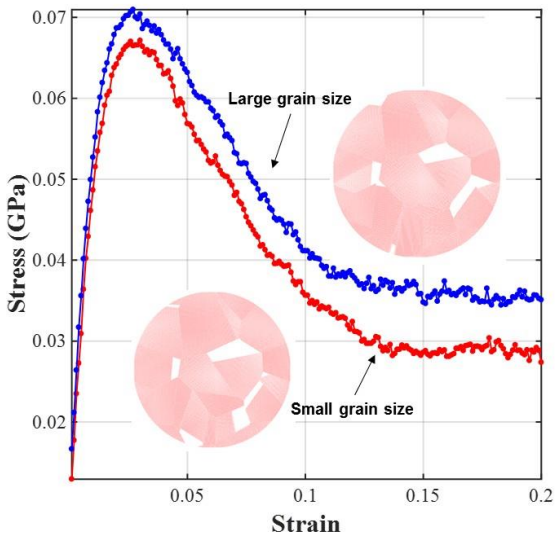

Figure 72. Effect of grain size on mechanical properties (particle diameter: 100 nm)

Another possible explanation is the difference in computational simulation and real model. Figure 73 shows an illustration of the explanation. For the real particle, probability that defects exist is lower in smaller particle. Therefore, the elastic yield limit is higher. On the other hand, for the MD model, since the grains and defects are generated artificially, if the size of the particle gets smaller, defects become dominant. Therefore, the elastic yield strength decreases.

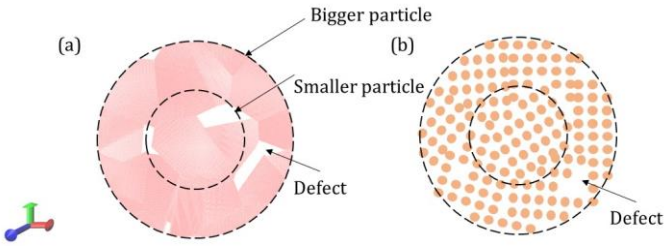

Figure 73. Effect of defects on mechanical properties (a) MD model and (b) real particle

5.2.4 Temperature change of substrate

Temperature change of the substrate with laser irradiation was measured by infrared (IR) camera (CX 320, COX). Figure 74 shows the image from the IR camera of the nozzle, PET substrate, and laser irradiation point. By analyzing the colors, temperatures can be measured. Figure 75 shows the temperature change with time. The laser power was 600 mW, laser scan speed was 50 mm/s, stage feed rate was 25 μm/s, and aerosol pressure was 1 bar. Substrate temperature decreases when the stage is moving and the aerosol is ejected because of a heat transfer effect. This cooling effect is shown from 5 to 20 seconds.

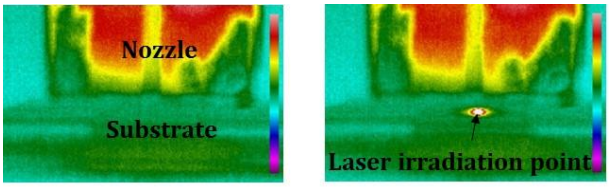

Figure 74. IR camera (CX 320, COX) image with laser irradiation

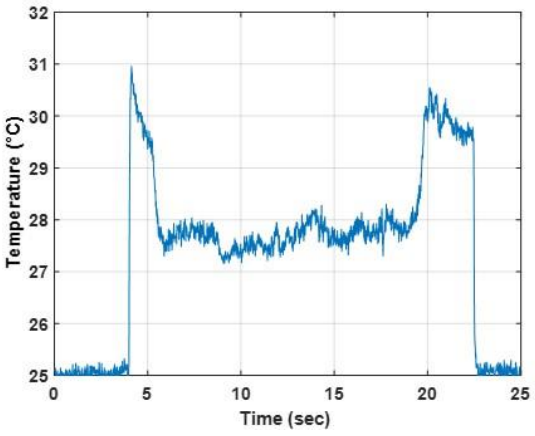

Figure 75. Temperature change with regard to time

In the system, the nozzle is located above the substrate. Therefore, it was difficult to measure the temperature without the camera untilted. Calibration was done to estimate the real temperature. Figure 76 shows the calibrated temperature. The temperatures of the substrate increase up to 60 and 70°C when the applied laser power are 400 and 600 mW respectively.

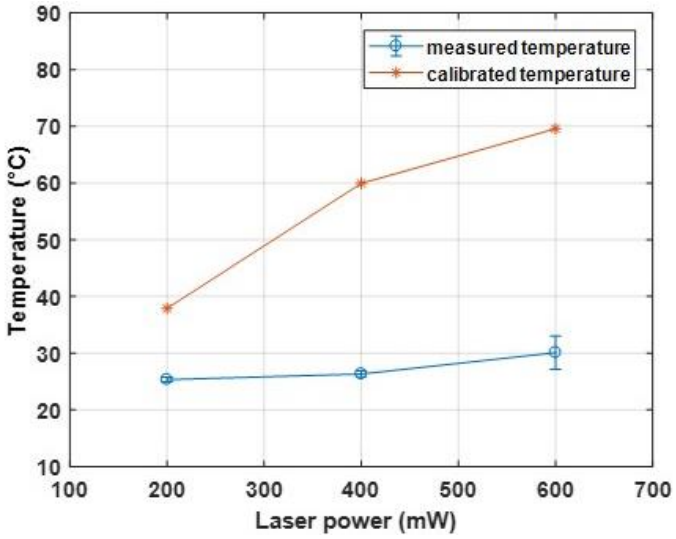

Figure 76. Temperature change with regard to laser power level

5.2.5 Mechanical properties of substrate

Mechanical properties of the substrate are also related to the deposition of the particles as discussed in Section 5.2.1. The elastic-plastic properties of PET film with different temperatures were analyzed. The temperature of PET substrate reaches around 70°C with laser irradiation as shown in Figure 76. The properties of PET film with different temperatures were found from the literature [153]. Table 10 shows the temperature dependent mechanical properties of PET film. Young's modulus and the elastic yield strength of PET substrate decrease with a higher temperature. These values were used to calculate the values of Q_p and U_T which are introduced in Section 5.2.1. It is shown that the elastic yield limit of PET substrate is lower than that of the particles.

Table 10. Temperature dependent mechanical properties of PET film [153]

Temperature (°C)	**Young's modulus (GPa)**	**Tensile strength (MPa)**	**Elastic yield strength (MPa)**
27	2.25	48.9	28.85
60	1.61	46.0	18.95
100	1.07	38.6	12.69
140	0.36	22.3	4.17
180	0.15	13.5	1.98

5.2.6 Prediction of the deposition

First, the adhesion between the substrate and the particle was studied. As discussed in Section 5.1, particle size and laser condition are the most important factors for deposition. The radius of particles varies from 0 to 2 μm. The adhesion with and without laser irradiation was predicted. Particle energy is calculated as

$$(Q_I - Q_p) - U_T. \tag{24}$$

Therefore, as discussed in Section 5.2.1, if the particle energy is greater than zero, particle will rebound. If the value is less than zero, it will adhere. The FEM results studied by Chun [27] and Choi [43] were used to estimate the velocity of the particles.

Figure 77 and Figure 78 show the results of the model. Without the laser irradiation, none of the particles adheres. However, if the laser has a power level that is higher than 400 mW, particles which have radius smaller than 900 nm will adhere. To make the particle and substrate adhere, the value of $(Q_I - Q_p) - U_T$ should have a negative value. Three methods can be conducted to lower the value: 1) reduce Q_I value, 2) increase Q_p value, or 3) increase U_T value. First, to reduce the Q_I value, either velocity of the particle or the mass of the particle should decrease. The velocity of the particles can be mainly controlled by the aerosol pressure. The mass of the particles can be controlled by the size of the particles assuming that same type of material is used. Therefore, one of the reasons why only small particles under certain criteria adhere is that the kinetic energy is smaller than that of the bigger particles. The effect of the particle velocity on deposition will be discussed in Section 5.2.7 with sensitivity analysis. The particles are more likely to deposit when the

velocity is low. Secondly, the energy dissipated in the plastic deformation should increase. Q_p is also related to the mass and velocity of the particles. However, the elastic yield limit Y and the limiting elastic velocity φ are the most important factors. As discussed in Sections 5.2.3 and 5.2.5, if the temperature increases with laser irradiation, the elastic yield limit of both particle and substrate decrease. This results in higher energy dissipation of the plastic deformation. Therefore, particles which rebound without laser irradiation will adhere with laser energy above certain level. As the particle size changes, mechanical properties also change. However, the value of the elastic yield limit is adopted as the softer between particle and substrate. The elastic yield limit of PET or paper substrate is always lower than that of the particle. Therefore, the plastic deformation is dominantly controlled by the substrate properties. There is no need to get the quantitative relation between the particle size and mechanical property. Finally, to increase the total adhesive energy, either mechanical energy or surface energy has to increase. The mechanical energy is related to the external force as well as contact geometry. These values are related to the projected radius of elastic and plastic deformation which are dependent on Young's modulus and Poisson's ratio of the particle and the substrate as well as the elastic yield limit of the softer body. The surface energy is determined by the material type of the substrate and the particle. It can be concluded that material type is also an important factor for adhesion.

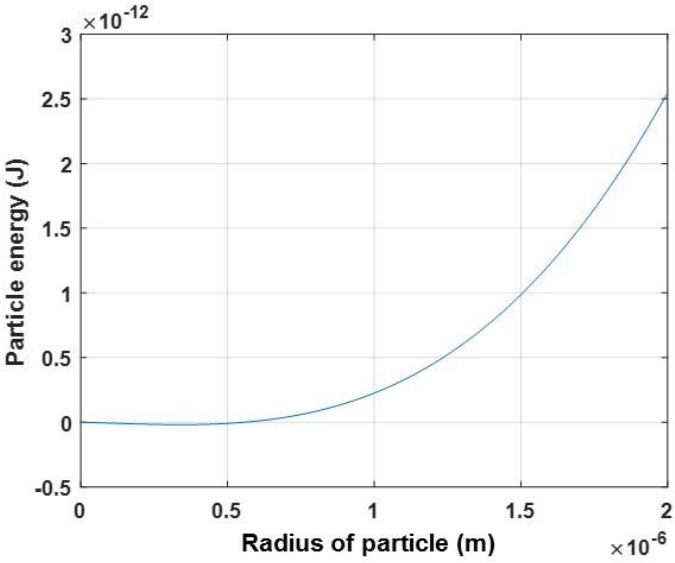

Figure 77. Adhesion condition without laser irradiation

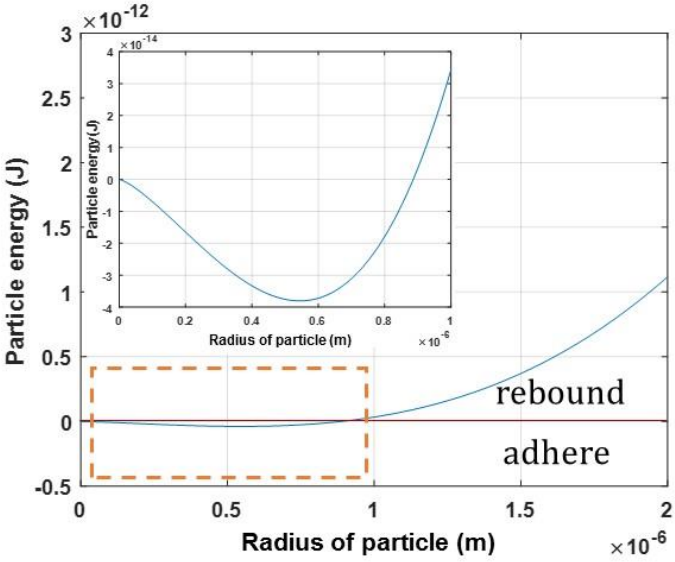

Figure 78. Adhesion condition with laser irradiation of 400 mW

After the adhesion of particle on the substrate, particle- particle adhesion occurs. Since the particle comes to the original state after the restitution process during the elastic deformation, radius of plastic deformation was predicted with different elastic yield strength of the particle. Figure 79 shows the illustration of the concept of projected radius

of elastic and plastic impact [154]. Figure 80 shows the relationship between the elastic yield limit and radius of plastic deformation. As the laser energy density increases, the temperature of the particle increases. Therefore, the elastic yield limit decreases. With lower elastic yield strength, radius of plastic deformation increases, which results in lower porosity. It eventually results in low resistance as discussed in Figure 43.

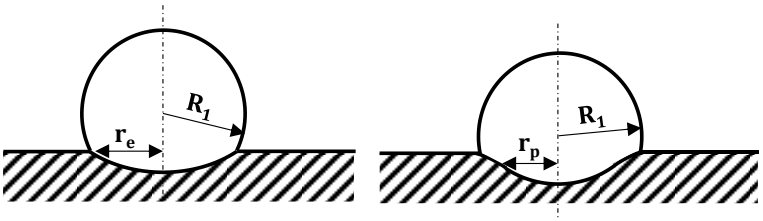

Figure 79. Projected radius of (a) elastic impact and (b) plastic-elastic impact [154]

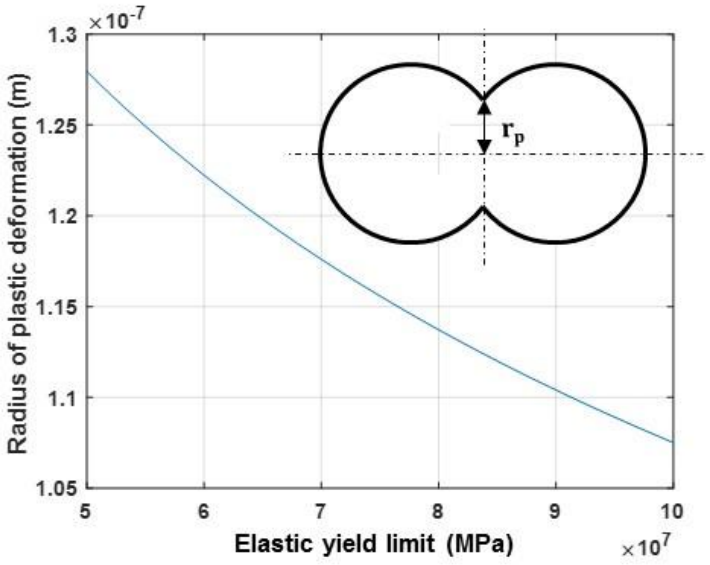

Figure 80. Relationship between elastic yield limit and radius of plastic deformation

5.2.7 Sensitivity analysis

Figure 81 shows the results of sensitivity analysis with different particle speed. The laser energy density is 2.6 J/cm^2. Young's modulus is 400 MPa. Particle speed mainly affects the value of the initial kinetic energy Q_I. If the particle speed decreases, initial kinetic energy decreases. Therefore, whole particle energy decreases accordingly, and particles are likely to adhere on the substrate. With the particle velocity of 300 m/s, particles of radius below 336 nm are expected to adhere. With higher velocity of 500 m/s, only smaller particles of radius below 247 nm are expected to adhere.

Even though the elastic yield limit is a more important factor to determine the adhesion than Young's modulus, the effect of Young's modulus on adhesion was also tested. Figure 82 shows the sensitivity analysis results of Young's modulus of the particle. The velocity of the particle was 300 m/s and the temperature of the substrate was 60°C. The adhesion is more probable for the particles with a higher Young's modulus.

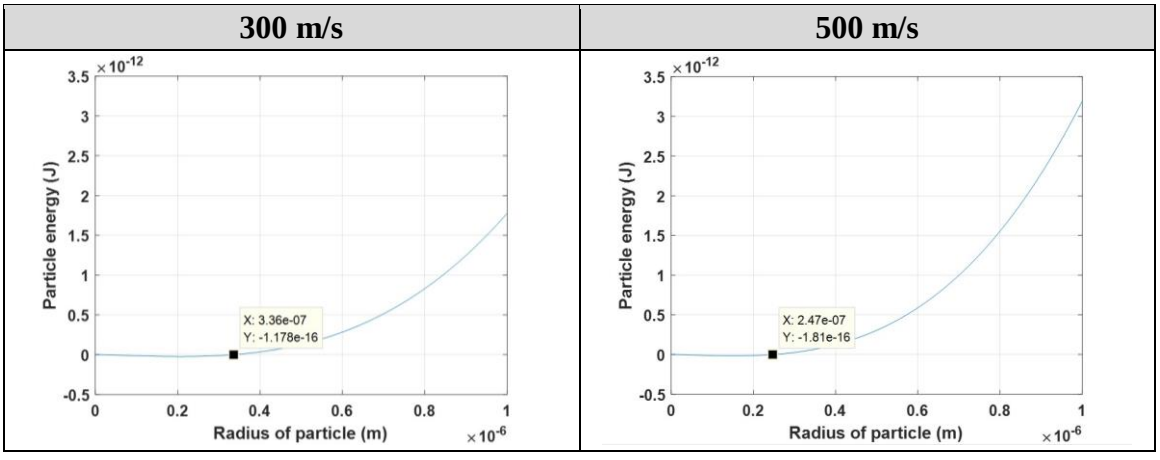

Figure 81. Sensitivity analysis of particle substrate adhesion: particle speed

Furthermore, the effect of the substrate temperature which can be controlled by laser energy density was analyzed. Figure 83 shows the results of the sensitivity analysis for substrate temperature. Young's modulus was 400 MPa and the particle velocity was 300 m/s. When the temperature of the substrate gets higher, particles can easily adhere.

3 GPa	400 MPa
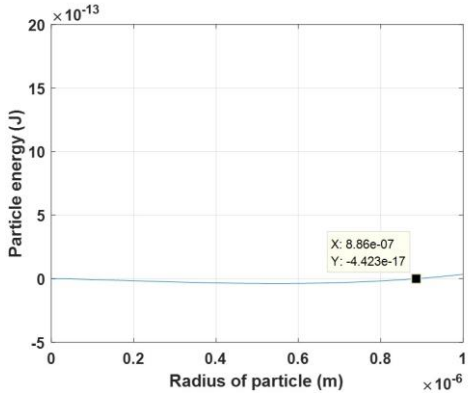	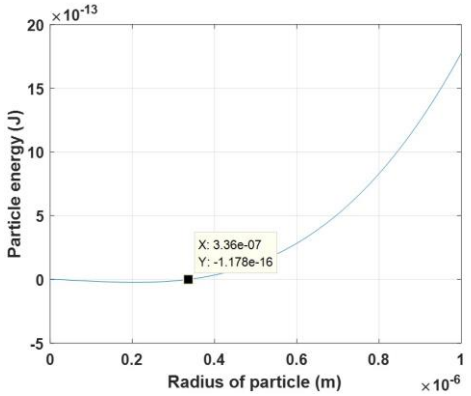

Figure 82. Sensitivity analysis of particle substrate adhesion: Young's modulus

60°C	100°C
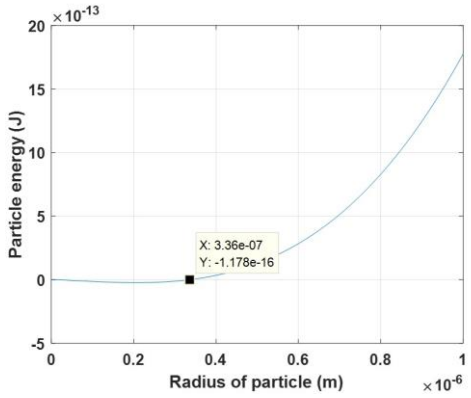	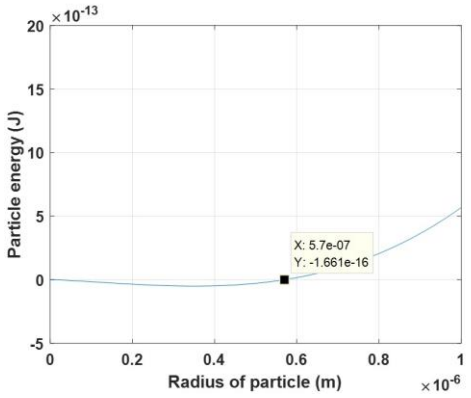

Figure 83. Sensitivity analysis of particle substrate adhesion: substrate temperature

5.2.8 Validation of the model

The deposition mechanism model was validated with the experimental results. Diameter of the particles was varied from 0.1 to 5 μm. They were bought from Sigma Aldrich and Thermo Fisher Scientific company. Figure 84 shows the SEM images of the different sized copper particles.

Printing was done with different aerosol pressure and laser energy levels on PET substrate. The aerosol pressure changes the velocity of the particles. Figure 85 shows the images of the samples right after they were took out from the chamber, and Figure 86 shows the images of the samples after the cleaning process.

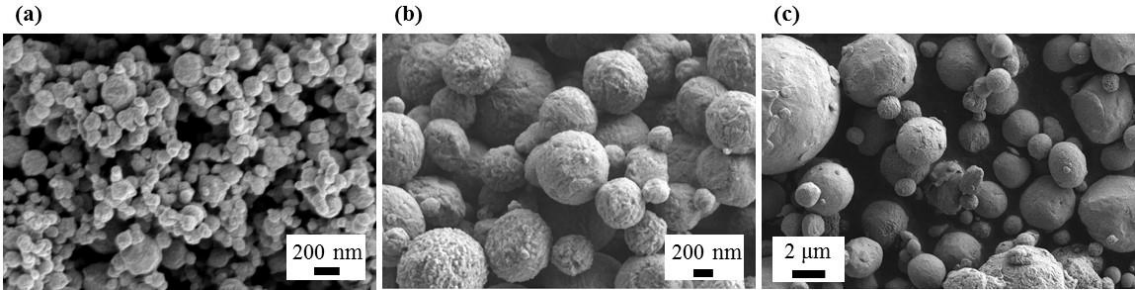

Figure 84. SEM image of the (a) < 100 nm, (b) 0.5~1.5 μm, and (c) 3.25~5 μm sized copper particles

Particle size (μm)	Energy density (J/cm^2) / Aerosol pressure (bar)	1.40	2.62	4.24	5.86
~0.1	1				
	2				
0.5~1.5	1				
	2				
3.25~5	1				
	2				

Figure 85. Printing results of different sized particles before cleaning process

Particle size (μm)	Energy density (J/cm^2) / Aerosol pressure (bar)	1.40	2.62	4.24	5.86
~0.1	1	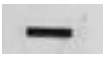			
	2		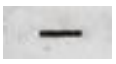		
0.5~1.5	1				
	2				
3.25~5	1				
	2				

Figure 86. Printing results of different sized particles after cleaning process

The particles which have diameter under 0.1 μm were successfully printed under any tested conditions. Printing of the particles with diameter of 0.5~1.5 μm was also successful. With the higher particle velocity, there are some marks in the area without laser irradiation. These were observed under the optical microscope. Figure 87 shows the optical

images of the samples with the highest laser irradiation of 0.5~1.5 and 3.25~5 μm sized particles. It is concluded that high velocity of the particles damages the substrate, whereas damages with laser irradiation were not significant.

With the particles with the diameter bigger than 3.25 μm, printing was not successful in any tested conditions. Therefore, it can be concluded that the particle size is the most important factor for deposition compared to the particle velocity and laser power level. These results also match with the predicted particle size for adhesion in the developed multiscale model. Table 11 shows the summary of the deposition conditions by experimental observation.

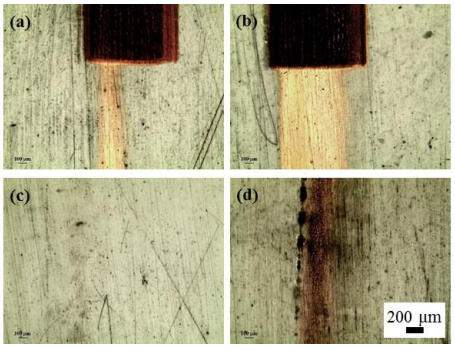

Figure 87. Optical image of the printing under condition (a) 0.5~1.5 μm, 1 bar, 5.86 J/cm^2, (b) 0.5~1.5 μm, 2 bar, 5.86 J/cm^2, (c) 3.25~5 μm, 1 bar, 5.86 J/cm^2, and (d) 3.25~5 μm, 2 bar, 5.86 J/cm^2

Table 11. Experimental results of deposition with different particle sizes and laser conditions

Laser condition / Particle diameter	Without laser irradiation	With laser irradiation (above certain energy density)
< 1.5 μm	No deposition	Deposition
> 3.25 μm	No deposition	No deposition

5.3 Morphology– cKMC model

The effect of laser treatment on morphological change of films in the nanoparticle deposition system is studied with cKMC simulation [45]. cKMC is a generalized version of classical kinetic Monte Carlo, which can be used to simulate both controlled and self-assembly processes at atomistic level with larger sizes and longer timescales than MD [155]. In this model, LI-NPDS which uses a slightly different laser treatment method from the NLP process was studied. LI-NPDS uses an in-direct laser sintering method as explained in Section 2.1. In the process, nanoparticles go through laser treatment in the aerosol flow through a tube before deposition. Thus the laser beam does not contact the substrate, and this avoids any potential damage on the substrate. Nanoparticles are then deposited on the substrate through the nozzle. In this work, a coarse-grained cKMC model was constructed to simulate diffusion, laser irradiation, and deposition processes simultaneously for alumina particle. Although this model uses different material and different system configuration, it shows the potential that this cKMC model is capable of predicting the morphological change of the printed results of nanoparticle printing system with laser process in large time and length scale. This model can be applied with different simulation parameters in the NLP process.

5.3.1 Controlled kinetic Monte Carlo

Since the timescale in the complete LI-NPDS process is much longer than normal microstructural evolution of laser sintering, it is difficult to use MD to simulate the LI-NPDS process. The directed particle diffusion and deposition in the process cannot be simulated with regular KMC, because KMC does not contain the complete information of

the physical systems. Kinetic energy is not directly modeled in KMC. As a result, KMC can only simulate pure self-assembly random events in bottom-up nanomanufacturing. It cannot simulate controlled movement of atoms and particles which only diffuse along certain directions, especially in some top-down manufacturing processes [155].

In contrast, cKMC allows us to impose directional constraints on diffusion and deposition in simulating the complete LI-NPDS process. cKMC [155] is a generalization of KMC, where deterministic events are introduced into the model so that either a random or deterministic event can lead to system state update. The deterministic or controlled events are used to model processes where atomic arrangement is triggered by external energy sources such as light, heat, electromagnetic field, or others. The modeling of these inputs is essential for top-down manufacturing processes, which is not possible in traditional KMC simulation. Figure 88 and Table 12 show the example of cKMC model for FIB process [155]. In cKMC, this is realized by introducing controlled diffusion direction so that particles can selectively diffuse at certain direction or towards certain location. Furthermore, different species with different kinetic energy levels can be introduced. This information is necessary to model complete physical systems, where traditional KMC is not able to do so. cKMC can simulate all the kinetic events simultaneously if the corresponding rates are known. cKMC has been implemented [156] and integrated with stochastic parallel particle kinetic simulator (SPPARKS), which is a KMC tool developed at Sandia National Laboratories [101].

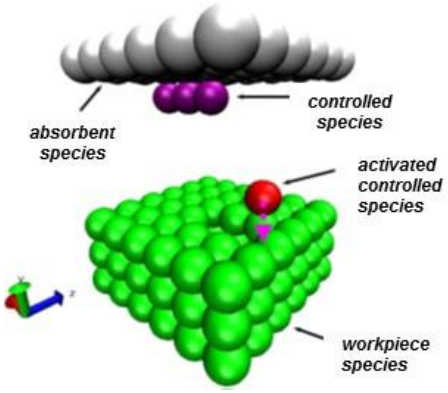

Figure 88. cKMC models for FIB [155]

Table 12. Example events in FIB lithography process [155]

Reaction/transition event
R1: $Ga\_src \rightarrow Ga^{+}$ (controlled)
R2: $Ga^{+} + vacancy \rightarrow vacancy + Ga^{+}$ (controlled)
R3: $workpiece\_species\_gas + vacancy \rightarrow vacancy + workpiece\_species\_gas$
R4: $workpiece\_species^{+} + vacancy \rightarrow vacancy + workpiece\_species^{+}$
R5: $Ga\_gas + vacancy \rightarrow vacancy + Ga\_gas$
R6: $e^{-} + vacancy \rightarrow vacancy + e^{-}$
R7: $workpiece\_species\_gas + absorbent \rightarrow vacancy + absorbent$
R8: $Ga\_gas + absorbent \rightarrow vacancy + absorbent$
R9: $workpiece\_species^{+} + absorbent \rightarrow vacancy + absorbent$
R10: $e^{-} + absorbent \rightarrow vacancy + absorbent$
R11: $Ga^{+} + workpiece\_species + vacancy \rightarrow Ga\_gas + vacancy + workpiece\_species\_gas$
R12: $Ga^{+} + workpiece\_species + vacancy \rightarrow Ga\_gas + e^{-} + workpiece\_species^{+}$

5.3.2 cKMC model of the printing system

The LI-NPDS process is schematically shown in Figure 89. Nanoparticles in LI-NPDS go through laser treatment in the aerosol flow through a tube before deposition. Thus the laser beam does not contact the substrate, and this avoids any potential damage of the substrate [44]. Nanoparticles are then deposited on the substrate through the nozzle. In this research, an on-lattice coarse grained cKMC model is built. In the coarse grained method, one nanoparticle instead of one atom is modeled at each lattice site. It is computationally more efficient to model larger particles instead of atoms if the physical or chemical interactions between atoms within a particle are not of interest. Therefore, coarse grained models are commonly implemented for large systems. The LI-NPDS model has 12800 fcc lattice sites. Each site has 4 basis atoms, so there are 51200 basis atoms in total.

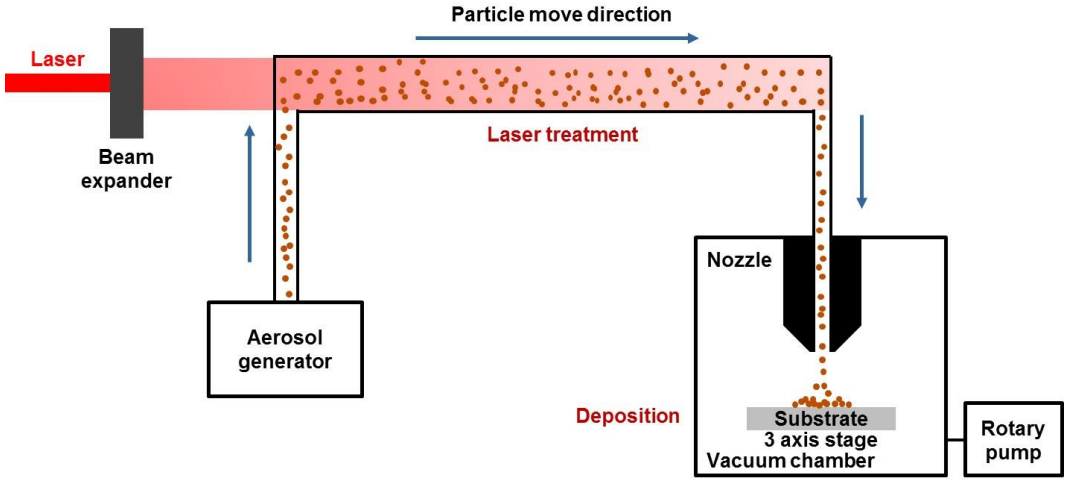

Figure 89. System configuration of the LI-NPDS process modeled by cKMC [45]

Events in cKMC are defined based on experimental observations in the physical system. To observe the laser effect on alumina nanoparticles (Cotronics corporation, 200 nm), the particles were captured after laser treatment and before going through the nozzle. This removes the effect of impact during deposition and focuses only on laser effect. Particle size was measured under particle size analyzer (Zetasizer Nano ZS, Malvern Instruments, UK). Figure 90 shows the relationship between size of clustered Al_2O_3 nanoparticles and laser power. As laser power increases, clustered particle size gets smaller. Agglomerate state is a preferred state of nanoparticles. Due to the effect of aerosol flow and laser energy, clustered nanoparticles crack down into small pieces. Figure 91 shows the comparison of different laser treatment methods. In a conventional laser sintering process, particles in steady state are heated by laser in powder bed. The surface of particles are partially melt. Particle coalescence occurs, and larger particles are formed. In contrast, when particles are moving in the aerosol flow with certain velocity, particles do not aggregate after laser treatment. Instead, they break down into small pieces because of the additional energy, including kinetic energy and thermal energy, induced by aerosol pressure difference and laser irradiation respectively.

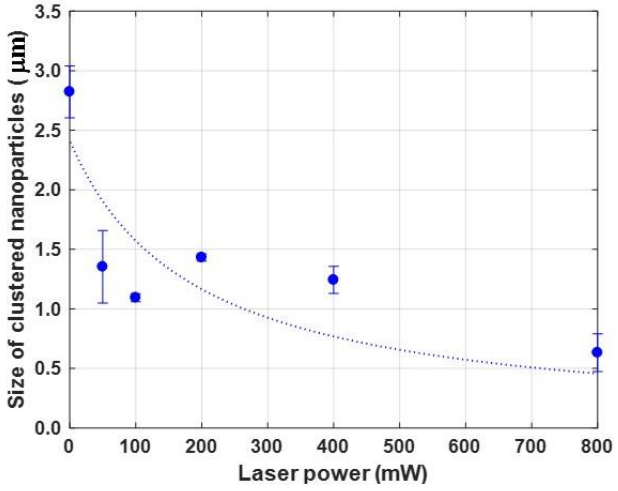

Figure 90. Effect of laser power on size of clustered Al_2O_3 nanoparticles. [44]

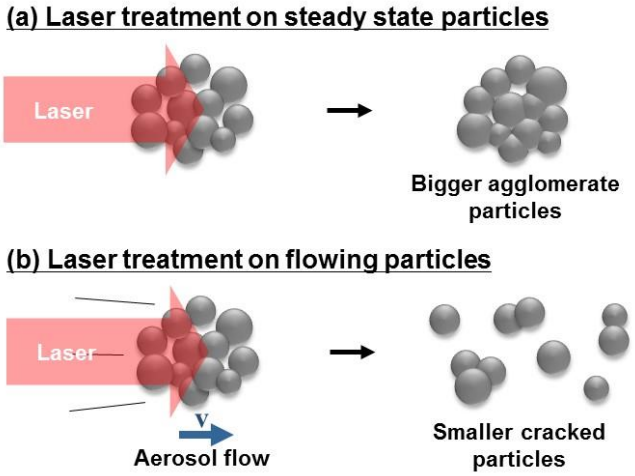

Figure 91. Comparison of results with different laser treatment methods. (a) particles that are in steady state and (b) particles with kinetic energy moving along aerosol flow [45]

Six types of species, including vacuum, air, agglomerated nanoparticle, disintegrated nanoparticle, deposited film, and substrate are defined. The events of reaction and diffusion, particularly laser treatment and deposition, are added with proper rates. Particle diffusion, laser treatment, and deposition events are defined as

$$\text{Nanoparticle} + \text{vacuum} \xrightarrow{Diffusion} \text{vacuum} + \text{nanoparticle}, \quad (25)$$

$$\text{Nanoparticle} + \text{air} \xrightarrow{Diffusion} \text{air} + \text{nanoparticle}, \quad (26)$$

$$\text{Agglomerated nanoparticle} \xrightarrow{Laser\ treatment} \text{Disintegrated nanoparticle}, \quad (27)$$

$$\text{Nanoparticle} + \text{substrate} \xrightarrow{Deposition} \text{Deposited film} + \text{substrate} \quad (28)$$

respectively. Figure 92 illustrates these events. In diffusion process, vacuum or air swap their positions with agglomerated or disintegrated nanoparticles so that particles can move forward to diffusion direction as Figure 92 (a). Laser treatment events change agglomerated nanoparticles to disintegrated nanoparticles with vacuum or air between them. Fewer nanoparticles after laser treatment are at the agglomerated state than the ones before. This is modeled in KMC as bond breaking as illustrated in Figure 92 (b). The effects of deposition are illustrated in Figure 92 (c). Deposition events happen when nanoparticles reach the substrate. After deposition events, agglomerated or disintegrated nanoparticles change into deposited film. Figure 93 illustrated laser treatment and deposition events with different laser power levels. Ratio of particles cracked varies with different laser powers. Expected deposition results with different particle sizes are shown. Larger particles are expected to form rough, porous, and thick film, in comparison with smaller particles.

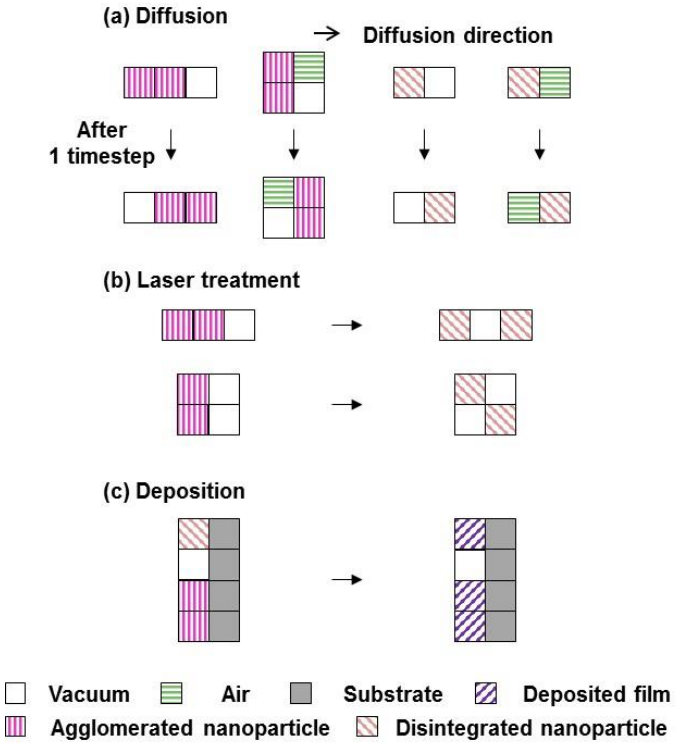

Figure 92. Examples of diffusion, laser treatment, and deposition events. (a) diffusion, (b) laser treatment, and (c) deposition events [45]

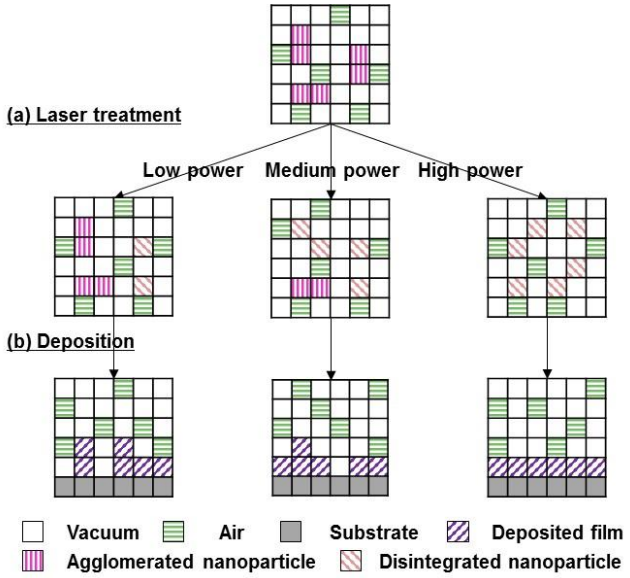

Figure 93. Illustrations of laser treatment and deposition with different laser power levels. (a) laser treatment and (b) deposition events [45]

The rate of reaction P is calculated as [157]

$$P = pexp\left(-\frac{E_a}{R_g T}\right), \tag{29}$$

where E_a is activation energy, R_g is the gas constant, T is the temperature, and p is the pre-factor. Here, laser treatment and deposition effect are separated, because there are many complex physical phenomena related to both processes.

Activation energy for laser treatment is the energy required for breaking agglomerated particles. This value was reversely calculated as 0.167 μJ using the data shown in Figure 90. The temperature of particles T is calculated based on

$$\Delta \mathrm{T} = \mathrm{H}\frac{1}{mc}, \tag{30}$$

$$\mathrm{H} = \alpha I A_l t, \tag{31}$$

where ΔT is the amount of temperature increase from room temperature, H is the amount of applied laser energy, m is the mass of particle, c is specific heat capacity, α is the absorptivity, I is the laser power, A_l is the area of laser irradiation, and t is time of laser exposure. The calculated particle temperatures are 25, 26.2, 27.4, and 29.8°C for laser power of 0, 50, 100, and 200 mW respectively.

In addition, deposition rates provide information about how many particles are actually deposited out of all particles that reached the substrate. Deposition rates and other simulation parameters such as reverse kinetic rates are difficult to measure by experiment

or obtain in references. Therefore, they are estimated through sensitivity analysis of the simulation model. Calibration was done with thickness data of the laser condition 0 mW.

Figure 94 shows the sensitivity analysis for reverse rate and deposition rate. As shown in Figure 94, circular markers are simulated data and the straight line indicates the reference value from experiments. If reverse rate is large or deposition rate is low, film thickness will be smaller than real value. However, if reverse rate is small or deposition rate is large, film thickness will be large. Therefore, both deposition and reverse kinetic rate were set as 0.1.

Experimental data were used to check whether the simulation model is reasonable. Al_2O_3 particles are deposited on sapphire wafer with LI-NPDS. Figure 95 shows the thickness measurement with the cross sectional image of the deposited film. The porosity of the deposited layer was estimated from the two-dimensional SEM images. Figure 96 explains the image processing process for porosity analysis. Images were converted to binary ones first, and the dark regions were then extracted as pores. Porosity was calculated as the number of whole pixels over the number of black pixels by using ImageJ particle analyze tool.

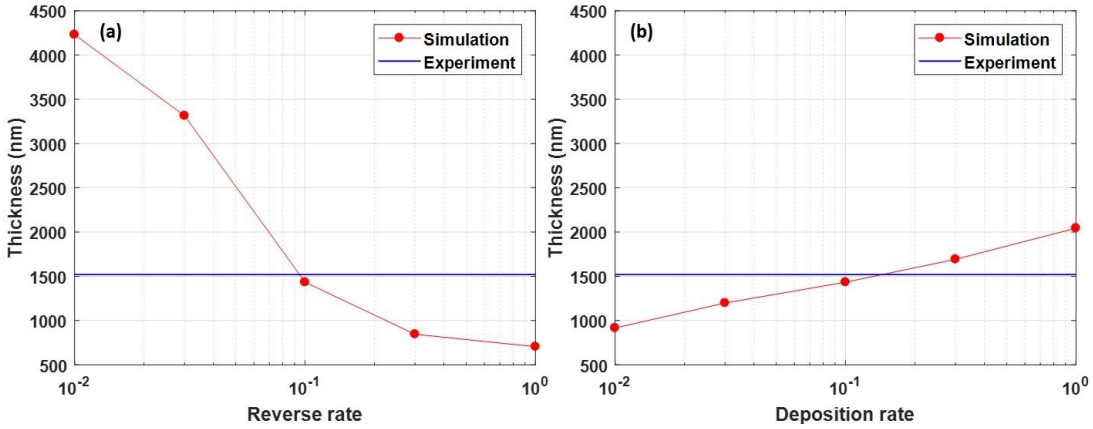

Figure 94. Sensitivity analysis for (a) reverse rate and (b) deposition rate [45]

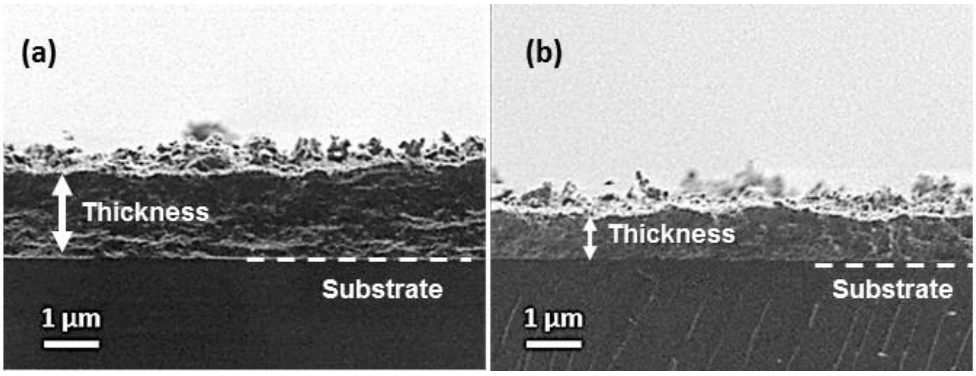

Figure 95. Cross section image of deposited film with (a) 0 mW and (b) 200 mW laser power for thickness analysis [45]

Figure 96. Image processing process for porosity analysis [45]

5.3.3 Simulation results

After the simulation model was built and rate catalog was completed, the model was run at different temperatures corresponding to different laser powers. Each simulation was repeated three times with different seeds to obtain statistical average since KMC is a stochastic algorithm. These results are averaged and standard deviations are expressed as error bars in the result graphs. The size of entire simulation model is $50 \times 16 \times 16$ and consists of around 40000 atoms. Simulation time is 80 time steps. It took around 40 minutes with computer with 64 bit Intel Core i7-4790 CPU. This is a relatively short computational time compared to other simulation tools. The actual physical process takes around tens of microseconds, which can be simulated within 1 hour. Approximately 160000 events occur for each time step in average. Figure 97 is the simulation results visualized with Visual Molecular Dynamics (VMD) tool [158]. As simulation time increases, particles which were initially located on the left side of the tube diffuse to the right side with laser treatment. After particles reach the substrate, they are deposited on the substrate and form a film. With different levels of laser power, the number of particles that turned into smaller nanoparticles and the properties of deposited layer varied.

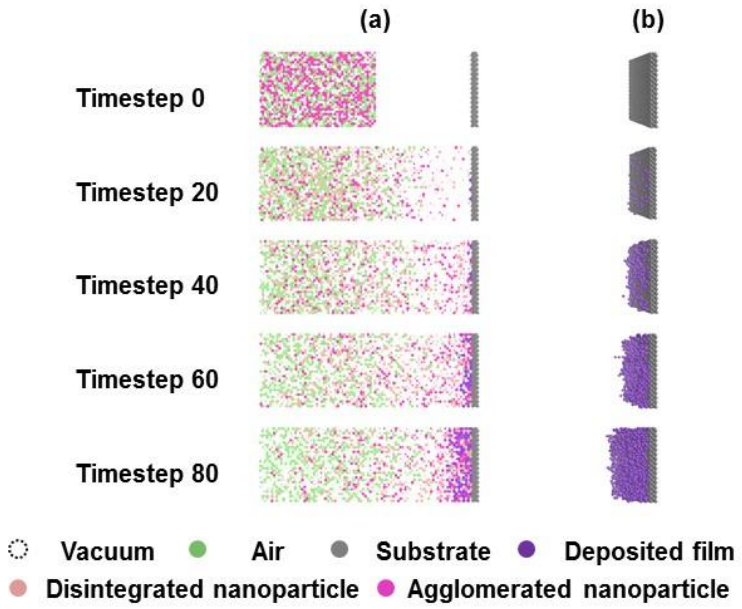

Figure 97. Visualization of the simulation result including (a) the complete system and (b) substrate [45]

5.3.4 Validation

Simulation results are compared with experimental results to check the validity of the simulation model. The predicted thickness is compared with the experimental results from the previous work of Ahn *et al*. [44]. The predicted porosity was also compared with the experimental measurement from images as shown in Section 5.3.2. Figure 98 shows the comparison of film thickness, where the simulated values are denoted by circles and experimental results by triangles. The thickness of the film decreases as laser power increases. Simulation results show the similar values and same trends as experimental results.

Figure 99 shows the comparison of the porosities of films predicted from simulation and experimental estimation. It is observed that higher laser power breaks nanoparticles into smaller pieces. Therefore, it results in less porous films. The explanation is that larger

agglomerated particles have larger interception areas that lead to hindrance of the deposition of other particles. As a result, small particles tend to form thin and less porous films than the larger ones.

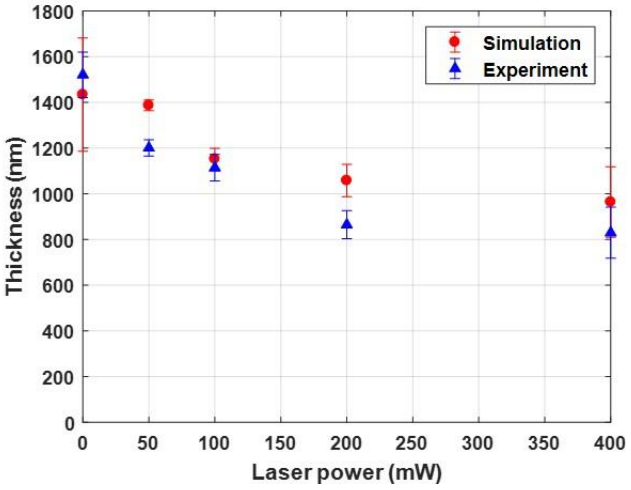

Figure 98. Simulation and experimental results: Change of thickness of Al_2O_3 deposition layer with respect to laser power [45]

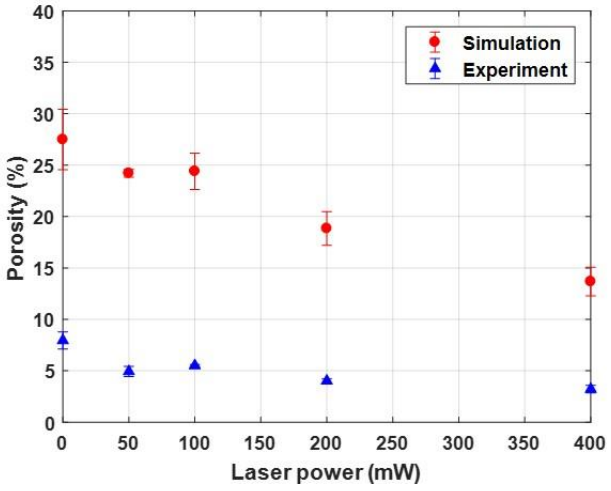

Figure 99. Simulation and experimental results: Change of porosity on Al_2O_3 deposition layer regarding to laser power [45]

As shown in Section 5.3.2, porosity was measured by image processing with SEM image of deposited layer. Since the two-dimensional images do not provide the sense of depth and the results are also dependent on the lighting condition when images were taken, the estimations of porosity are always lower than simulation predictions. The simulation predictions were based on the three-dimensional structures, where the number of deposited nanoparticles was counted and porosity was calculated directly. Because the experimental measurement of porosity has an inherent bias, there is a value difference or discrepancy between the two sets of values. Nevertheless, the trend and slope are the same.

To validate the simulation model where its predicted porosity value cannot be directly measured experimentally, a Gaussian process regression (GPR) or Kriging model is constructed to predict the discrepancy, which is

$$D(x) = Sim(x) - Exp(x) + \mathrm{e}, \tag{32}$$

where $Sim(x)$, $Exp(x)$, and $D(x)$ are the simulation prediction, experimental measurement, and discrepancy between the two, respectively, which are functions of laser power level x, and e is the statistical random error. GPR is a constrained regression modeling process where models are forced to interpolate all data points. GPR can provide modeling flexibility with sequential sampling compared to classical polynomial regression model. If new data points are available, there is no need to change the previously built model, and it can be updated with the new data.

The distribution of discrepancy is obtained from the data at the laser power levels from 0 to 200 mW. The GPR model is built using DACE (Design and Analysis of

Computer Experiments) with Matlab [159]. Figure 100 shows the GPR model for discrepancy. Zero order polynomial is used for regression, and Gaussian function is chosen for correlation model. Correlation function parameter is 1.668. Based on the GPR model of $D(x)$, the value of discrepancy $D(\mathrm{x} = 400)$ at 400 mW is estimated. Then the value of $Exp(\mathrm{x} = 400) = 3.04\%$ is predicted. The actual experimental measurement of porosity at 400 mW is 3.22%, as shown in Figure 99. The model prediction matches experimental results well.

From the cKMC simulation and GPR discrepancy model, the laser power level can be optimized based on desired thickness or porosity. The prediction capability is essential for simulation based process design and optimization. In this GPR model, there are only 5 data points. More experimental data can increase the accuracy of the GPR prediction results. Likewise, in this simulation model, the complex process is simplified and modeled with few species and events for the sake of computational efficiency. For example, in this model, it is regarded that there is only one size for agglomerated or disintegrated particle. However, agglomerated or disintegrated particles have different sizes. More species and events could be defined for complexity. Sophisticated models will have accurate results, but computational cost will increase at the same time. This simplified coarse-grain and low-fidelity simulation model is suitable for quick prediction of the trend. Although this model uses different material with an indirect laser sintering method, the developed model can be used to predict morphologies of the printed films by the NLP process.

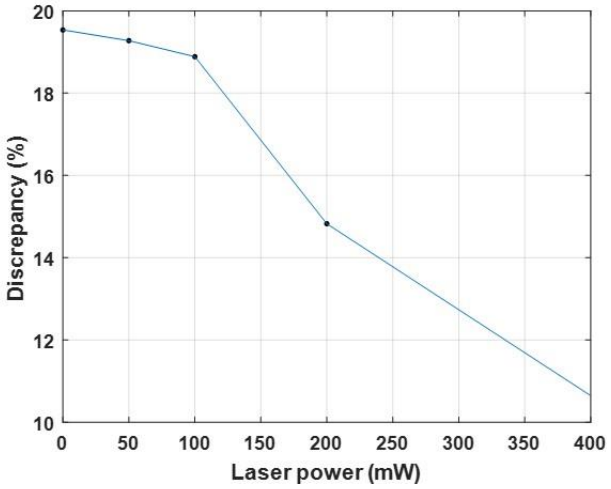

Figure 100. GPR model for discrepancy [45]

CHAPTER 6. APPLICATIONS

Three applications were developed with the deposited patterns printed with the NLP process on flexible substrates, which take advantages of the NLP process to facile the fabrication process. First, copper particles were printed on PET substrate using different oxidation levels and pattern widths to control the hydrophobicity of the surface. The NLP process can control both pattern widths and oxidation levels at the same time. This is introduced in Section 6.1. In addition, kirigami electronics on paper were developed in Section 6.2. These can be fabricated easily using laser cutting and printing within one system. This is available using different levels of laser energy. By changing the cutting design, stretchable and bendable electronics were demonstrated. Furthermore, durable strain sensor was developed by printing a strain sensor with conductive lines. The NLP process is capable of adjusting the electrical and mechanical properties of the printed patterns by changing the levels of laser energy. Therefore, performance of the strain sensor and conductive line can be controlled. When the strain sensor and conductive lines are printed together, the soldering area can be located in the area which is less affected by the bending motion. Therefore, the durability of the sensor increases. The detail fabrication process and results are discussed in Section 6.3.

6.1 Hydrophobic/Hydrophilic surface

It is widely known that hydrophobicity changes with the oxidation degree in case of copper material. Cu_2O is known for hydrophobic, and CuO is known for hydrophilic material [126]. The NLP process can adjust the composition of the printed materials using laser as discussed in Section 4.3.2. The oxidation degree of the copper particles with different levels of laser irradiation was examined with XRD analysis as shown in Figure 40. Moreover, different widths of the patterns can change the hydrophobicity of the surface [125-127]. Figure 101 shows the copper patterns on PET film with different pattern widths. The distance between lines was varied from 100 to 400 μm. Figure 102 shows the test setup for measuring contact angle of a water drop. Smartdrop from the Femtofab company was used. The needle approaches and drops 1 μl of water on top of the surface. A high speed camera was used to capture the geometry of the water drop and calculate the contact angle.

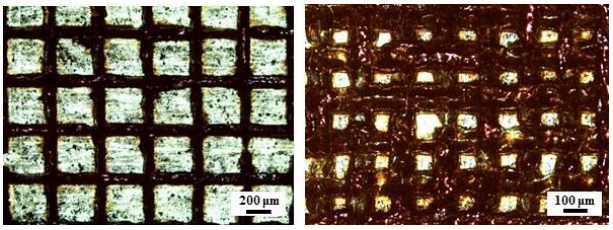

Figure 101. Copper patterns on PET substrate (400, 100 μm)

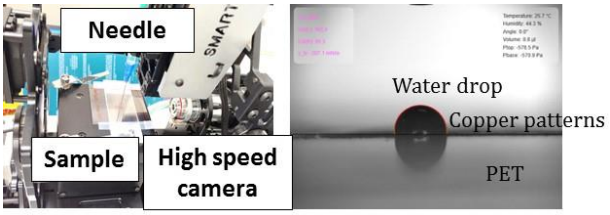

Figure 102. Contact angle measurement system

Figure 103 shows that contact angle was changed with different widths of the patterns and oxidation degrees. Yoon *et al*. [125] reported that when the pattern width changes from 100 to 500 μm, contact angle increases with a larger pattern width but begins to decrease from a certain criteria around 300 μm. It is assumed that small patterns make water drop float between the patterns. However, patterns smaller than certain size hinder the water droplet from forming a spherical shape. In this research, patterns with the width of 100 μm have a smaller contact angle than that of 400 μm except for the highest laser energy irradiated sample. As discussed earlier in Figure 40, when laser energy level increases, Cu_2O becomes CuO with more oxidation. However, when the energy density is higher than 5.86 J/cm^2, Cu_2O appears again. Since Cu_2O is hydrophobic, and CuO is hydrophilic material, contact angle should increase again with the higher laser energy irradiation above 5.86 J/cm^2. This trend was shown in the sample with 100 μm pattern width. In 400 μm patterned sample, the contact angle of the highest laser energy irradiated sample was similar to that of the middle energy irradiated sample. The contact angle of PET substrate was 80°. It can be concluded that by changing the width and oxidation degree of the copper patterns, the wetting property of the surface can be controlled. The NLP process is capable of changing oxidation degree and pattern width at the same time. In order to evaluate the effect of pattern width and laser energy explicitly, patterns should be printed more precisely with various laser conditions.

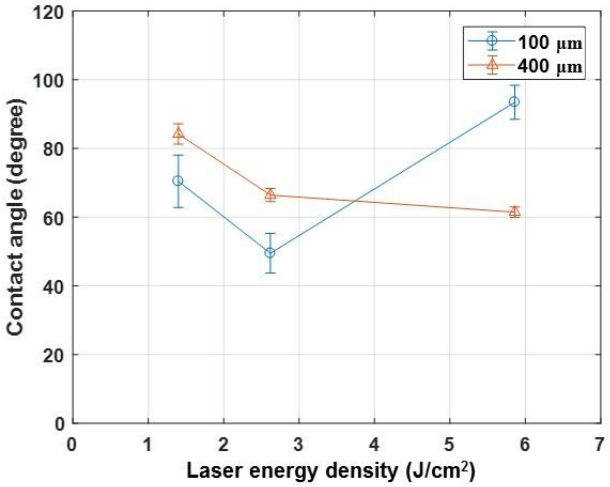

Figure 103. Contact angle difference with regard to laser power and pattern size

6.2 Kirigami flexible/stretchable electronics

Paper is a lightweight, eco-friendly, and low cost material. In addition, it is flexible and foldable. There are many potential applications including display, sensor, solar cell, and memory device. In the NLP process, cutting and printing can be performed within one system without referencing between two processes. Therefore, this process can be used to cut the printed patterns before packaging in the industrial applications without position reference issues. New applications can be developed with kirigami and origami of paper. In this research, kirigami electronics were fabricated. Figure 104 shows the fabrication process of kirigami electronics using bending and stretching motion of paper. Figure 104 (a) shows the paper cut on the same side. Bending motion was applied. In Figure 104 (b), paper was cut on the opposite side, therefore stretching motion was available. The distance between the cuttings was 500 μm. The paper was cut leaving 500 μm distance for

deformation. This area works as a connection part when paper is deformed. If the remaining distance is bigger than 500 μm, deformation is not available. However, if the distance is too small, samples were easily broken. This is an optimized value for the board paper with the thickness of 0.32 mm. If the thickness or the material of the substrate changes, this value will be changed. After the cutting, printing was done on the paper with the laser energy level of 5.86 J/cm^2. Even though there were changes on the aerodynamic flow because of the cuttings on the substrate, printing was successful. If the printing is done before cutting, there will be damages on the silver printings because of the high laser energy used in order to cut the paper. Wires were attached with the silver paste. After that, deformation was made and conductivity was tested. In this application, UV resin was not used for coating. Even though samples were not fully packaged as the examples shown in Section 4.4.1, they were stable and same performances were shown with the repeated tests of five times.

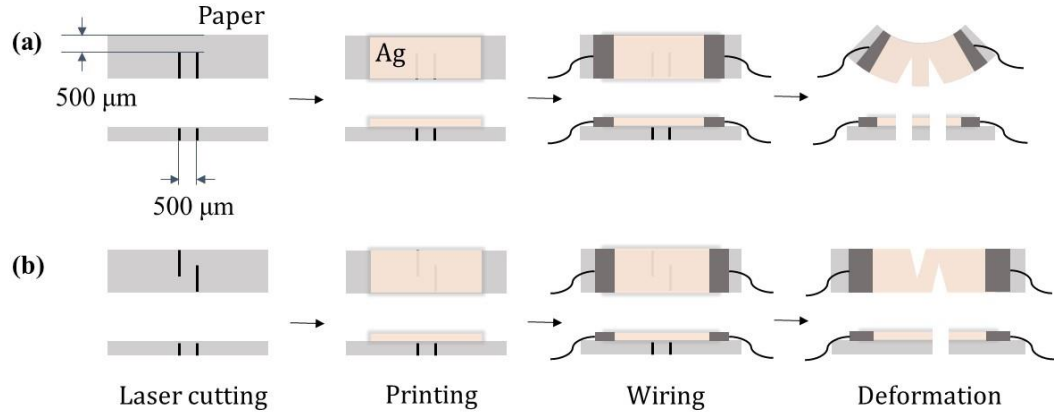

Figure 104. Fabrication process for kirigami flexible/stretchable electronics (a) cut in the same side and (b) cut in the opposite side

Conductivity of the sample was tested with the LED light after the bending and stretching motion. Figure 105 shows the results before and after deformation, and Figure 106 shows the illustration how they are deformed. Figure 105 (a) shows the bending motion. The sample was conductive even after the bending over 90°. As illustrated in Figure 106 (a), only the connected part deformed. Since the connected parts were folded in the outer folding direction as described in Section 4.4.1, resistance increased. However, the sample was still conductive. Figure 105 (b) shows the stretching motion of the kirigami electronics. As illustrated in Figure 106 (b), not only the connected parts but also the beam in the middle deformed. In this case, the connected part on the right was folded in the inner folding direction, whereas the connected part on the left was folded in the outer folding direction. Likewise, the beam located in the middle was deformed in both convex and concave bending directions. Ideally, the increase and decrease in the resistance are summed up to zero. Therefore, conductivity of the sample is expected to be the same even after the deformation. These results show the feasibility that the NLP process is capable of cutting and printing within the system. Therefore, flexible electronics using kirigami can be fabricated. Quantified characterization on the relationship between deformation and conductivity is needed in future research. In addition, in this example, only two lines were cut. However, if the number of cutting increases, the range of deformation will be larger. In addition, complicated geometry can be designed and cut to create complex deformation. Laser can cut complicated and curved patterns easily.

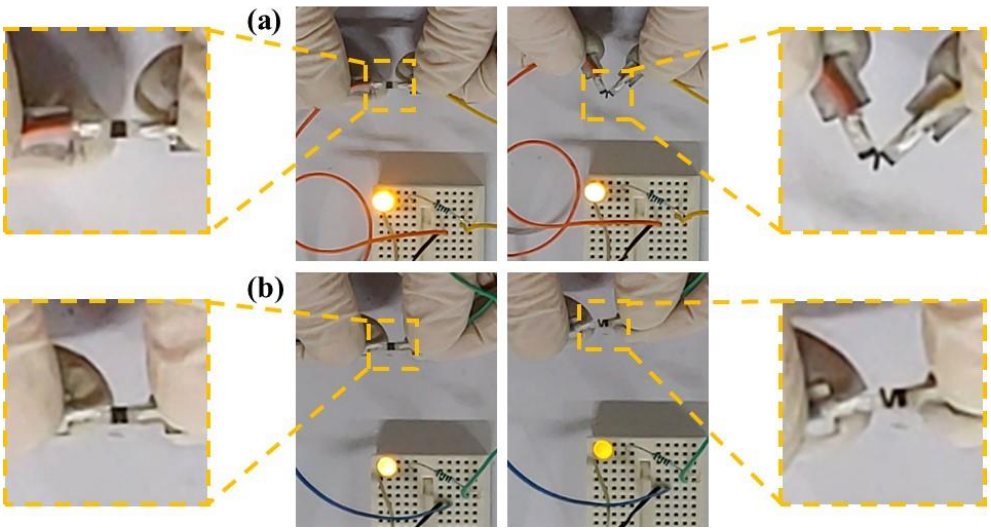

Figure 105. Conductivity test of fabricated electronics using kirigami of paper with (a) bending and (b) stretching

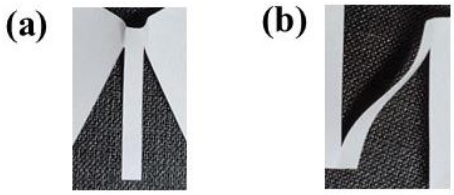

Figure 106. Illustration of the deformation in (a) bending and (b) stretching motion

6.3 Conductive line integrated strain sensor

The NLP process can control the property of the printed patterns. As discussed in Section 4.4, laser power changes the porosity of the patterns. The porosity is decreased with the irradiation of the high level of laser energy. Therefore, changes of resistivity are less sensitive to the bending and folding. The patterns can be utilized as a conductive line or sensor which has a wide sensing range. On the other hand, the porosity level is high with the irradiation of low level of laser energy. Therefore, the resistivity is sensitive to the bending or folding. These patterns can be utilized as a highly sensitive strain or pressure sensor. In strain sensor applications, unstable soldering is an issue. To prevent the thermal damage, the soldering of the strain sensor printed with direct printing methods is normally done with silver paste. However, the repeated bending tests cause the detachment or the disconnection of the soldering part. Figure 107 shows the detachment when the soldering is done near the bending area after several repeated tests. As marked in yellow circles, the soldering parts are unstable and can be easily detached after the repeated bending tests causing malfunction of the strain sensor.

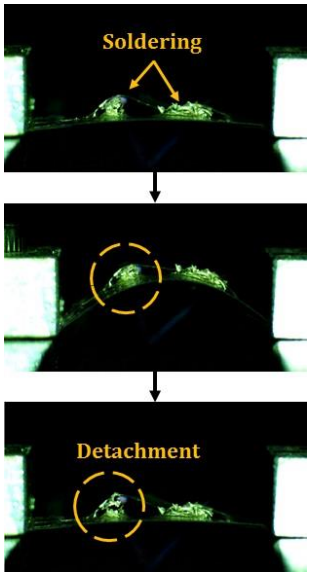

Figure 107. Unstable soldering issue near the bending area

Therefore, if the conductive lines are printed together with the strain sensor, soldering can be done far from the bending area. This detachment problem can be solved. Figure 108 shows the schematic diagram and optical image of the copper strain sensor printed with the conductive lines on PET substrate. Figure 108 (a) shows the printed strain sensor with the geometry of 1×4 mm^2. Figure 108 (b) shows the stain sensor and conductive lines printed together. The conductive lines were printed on the edge of the strain sensor with the overlap of 1 mm distance. The connected part marked with a red box was observed under optical microscope. There was a difference in the brightness of regions in the sample. The printed area of the conductive lines was darker compared to the area of the strain sensor with denser structures. The strain sensor was printed with the low laser energy of 1.40 J/cm^2 and the conductive lines were printed with the high laser energy of 5.86 J/cm^2.

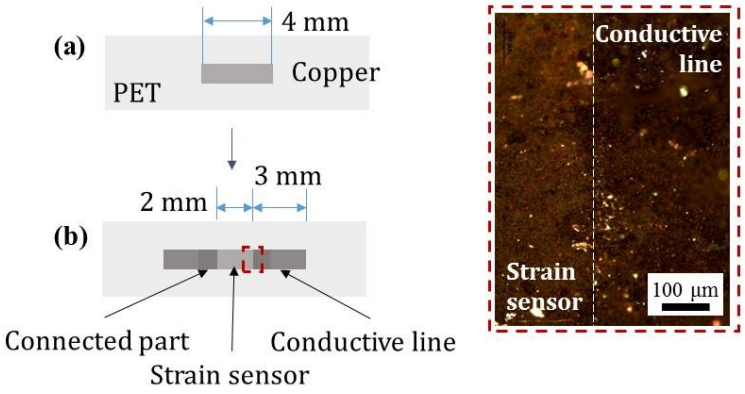

Figure 108. Conductive line integrated strain sensor

Figure 109 shows the bending test of the strain sensor and the strain sensor printed with conductive lines. The soldering was done on the area which is less affected by bending in case (b). The stage traveled for the distance of 2000 μm with the velocity of 100 μm/s. After each loading and unloading cycle, 500 ms was posed for stabilization. This was repeated 100 times.

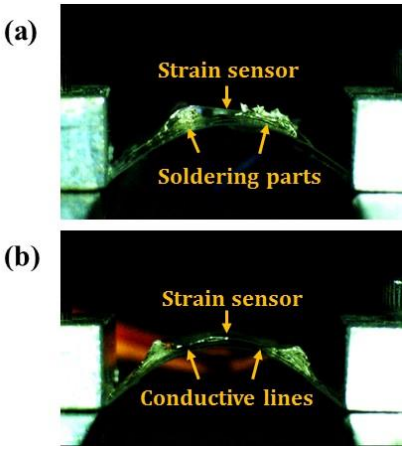

Figure 109. Bending test of (a) strain sensor and (b) conductive line integrated strain sensor

Figure 110 shows the results of the repeated bending tests. In the strain sensor, soldering parts were unstable after 30 bending cycles and completely detached after 90 cycles. However, if it is printed with conductive lines, steady performance is observed even after 100 cycles. The performances are the same in both cases when they were in the stable states. Further work needs to be done to improve the performance of the strain sensor such as designing the patterns as shown in Figure 111 or optimizing the process parameters.

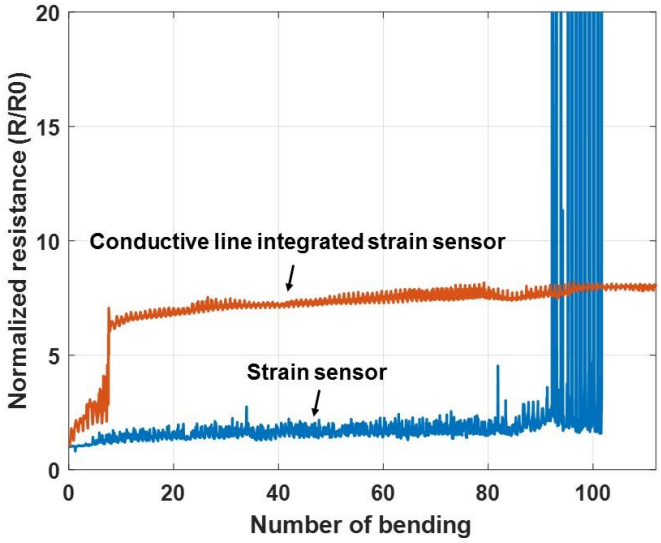

Figure 110. Change of normalized resistance with bending in strain sensor and conductive line integrated strain sensor

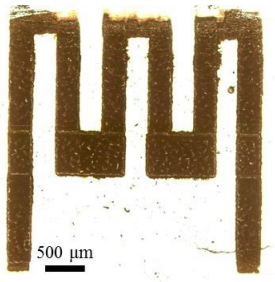

Figure 111. Printed strain gauge pattern with the NLP process

In summary, laser power can be controlled for the purposes of selective deposit, cut, and material property tuning of the prints. If the laser power is below 0.76 J/cm^2, particles are not printed. With a high laser energy level between 0.76 and 5.86 J/cm^2, the chemical and electromechanical properties can be tuned. With the laser energy higher than 5.86 J/cm^2, printing was also successful. But damages were found in the flexible substrate. With a laser energy level higher than 15 J/cm^2, cutting can be achieved. Since this process can control the laser energy easily, by combining these effects in printing, various applications can be developed. In addition, since the process time is fast by printing patterns line by line, applications with large feature scales with microscale resolution can be developed.

CHAPTER 7. CONCLUSION

In this research, a high throughput direct writing process for flexible electronics was developed, where nanoparticles are sintered with laser while they are selectively deposited. This process can successfully print copper and silver patterns with 50 μm resolution on paper and PET substrate. At the same time, properties of the patterns can be improved and localized to the scale of the laser beam focal size. Mechanical and chemical properties of the patterns can be localized by controlling the laser conditions.

A low level of laser energy was used to prevent the damage on the substrate. As reviewed in Chapter 2, most of the additive processes with laser use high laser power to partially or fully melt the particles. This could result in thermal damage or energy inefficiency. In this newly developed process, selective deposition was available under the laser condition as low as 1.40 J/cm^2. Particles can be affected by low laser energy and low temperature condition because of the size effect. Small particles with a diameter under 100 nm have higher efficiency of laser energy absorption than that of larger particles with a diameter of tens of micrometers. In addition, it uses low aerosol pressure in atmospheric condition, which reduces the cost of the process. Nanoparticle deposition with aerosol jetting method normally uses inert gas or vacuum condition which is expensive. The NLP process does not require vacuum condition or any specific inert gas. In addition, since the process deposits patterns line by line, its process time is relatively fast. Compared to AFN printing which is a dry particle printing process which can print patterns, process time for printing the area of 1 cm^2 reduced from 500 to 200 seconds. Therefore, large area

deposition is available with fast process time. It shows the possibility of low cost and large area deposition for appropriate technology.

This newly developed process was evaluated by analyzing printing performances with different printing parameters and laser conditions. Properties of the printed patterns were analyzed with various characterization methods. The process-structure-property relationship was studied for electrical and mechanical properties of the patterns printed with different process parameters. Low laser energy irradiation results in high porosity structure as observed in SEM, where particle contact is weak. It has high resistance. In addition, the change of resistance is sensitive to the bending and folding. Mechanical property of crack propagation was examined with cycle tests. This process can have controlled or localized properties as well as durable printed results because of the laser sintering effect.

A multiscale model was built to predict adhesion in the NLP process. An analytical model was combined with a MD model to study the effect of particle impact and laser thermal effect simultaneously. Adhesion was predicted with different particle sizes and laser conditions. Results of the model were validated with the experiment results. Furthermore, a cKMC model was built to predict the morphological changes of the printed patterns. The simulation model is calibrated with experimental data. Different laser irradiation conditions on alumina particles are studied, which result in different thickness and porosity of the deposited layers. A Gaussian process regression modelling approach is also developed for model validation with the consideration of observation bias and discrepancy. Simulation results are in good agreement with the experimental results. Although this model uses different material and different laser irradiation method, the

developed simulation and discrepancy models can be used to predict film properties in the NLP process.

Three applications were developed to emphasize the unique advantage of the newly developed process. It can print patterns with controlled chemical compositions which have different hydrophobic and hydrophilic property. The wettability of the surface can be changed by two factors, patterning with different widths and under different laser conditions. The effect on the contact angle of water droplet was analyzed. If various patterns with different chemical compositions can be designed properly and printed in one system with the NLP process, it can be utilized as microfluidics applications. Furthermore, the process can print and cut the flexible electronics within one system. The paper substrate was cut with laser of high power, and conductive lines were printed to fabricate kirigami electronics. This can lead to interesting applications such as sensors and electronic papers where laser can cut curves or complicated patterns more precisely than traditional cutter or scissors. It can be also used to cut the printed patterns before packaging in industrial applications without position reference issues. Furthermore, the process can print patterns with designed properties with controlled laser energy irradiation. A strain sensor with integrated conductive line was developed to make the sensor durable with repeated bending tests. The performance of the sensor was tested and compared. If designed properly, it can have high performance and good durability.

The novel contributions of this research are listed as follows.

- A new hybrid process for micro/nano patterning was developed combining NPDS and laser. This process uses a slit nozzle for jetting the aerosol of nanoparticles and uses laser

in a vertical direction through the nozzle selectively to print patterns. This process adopts the principle of a commercial desktop laser printer in NPDS for the first time. A direct patterning of dry nanoparticles in 50 μm resolution under atmospheric condition and with the use of laser condition as low as 1.40 J/cm^2 was available. At the same time, properties of the patterns can be improved and localized to the scale of the laser beam focal size. Since the process deposits patterns line by line, its process time is relatively fast. These advantages make the system unique when fabricating applications by simplifying the fabrication process and extending the possibilities of the performance. Examples of hydrophobic and hydrophilic surface, kirigami electronics, and strain sensor integrated with conductive line were fabricated within one system for the first time.

- A multiscale deposition and adhesion model is developed. This combined model provides a multiscale framework from atomic to mesoscale. This new model can predict the deposition mechanism considering both impact and thermal effect below the particle melting point. In addition, the morphological changes of the deposited films as the effects of laser were studied with the novel cKMC model. By using coarse grained cKMC, deposition, diffusion, and laser treatment are integrated in a single simulation model. The proposed multiscale approach has the unique advantage of predicting laser treatment effect with diffusion and deposition of particles in an efficient way.

The process developed in this work can be further extended in future research. For example, the large area deposition will be available with increased nozzle size and adjusted process parameters. In addition, by decreasing the laser focal size or changing the laser beam shape, the resolution or the feature size of the printing can be improved. Pre-heating of the substrate and controlling the timing for laser irradiation can be tested. In this research,

only copper and silver particles are printed. Other functional metal particles or ceramic particles can be used for printing with different printing and laser conditions. For example, $BaTiO_3$ particles which have a piezoelectric property or NiTi particles which show a shape memory effect can be used as printing materials to develop interesting applications. Multi-materials or multi-layers can be also printed. In addition, if the laser condition is controlled continuously, functionally graded materials which have different properties within one layer or between layers can be printed. Furthermore, other types of stretchable or flexible substrate materials can be tested. In the analysis, the laser effect on the substrate materials of paper and PET needs to be studied further. The electromechanical properties need to be studied more systematically to establish complete process-structure-property relationship. In addition, in the developed multiscale model, assumptions were made. These assumptions need to be examined more thoroughly to improve the accuracy of the model. For example, the effect of the laser in the velocity of the particles can be investigated. Heat conduction between the particles and convection can be considered. Moreover, the developed applications can be improved further. If the patterns are designed properly and printing conditions are tuned, printed hydrophobic and hydrophilic patterns can be used in microfluidics applications. The performance of the kirigami electronics and durable sensor applications can be enhanced. Other applications such as pressure sensors, energy storage devices, or electrodes can be developed using advanced printing materials.

REFERENCES

1. Zheng, Y., et al., *Direct Desktop Printed-Circuits-on-Paper Flexible Electronics.* Scientific Reports, 2013. **3**: p. 1786.

2. Ko, S.H., et al., *All-inkjet-printed flexible electronics fabrication on a polymer substrate by low-temperature high-resolution selective laser sintering of metal nanoparticles.* Nanotechnology, 2007. **18**(34): p. 345202.

3. Xu, S., et al., *Stretchable batteries with self-similar serpentine interconnects and integrated wireless recharging systems.* Nature communications, 2013. **4**: p. 1543.

4. Jung, Y.H., et al., *High-performance green flexible electronics based on biodegradable cellulose nanofibril paper.* Nature communications, 2015. **6**: p. 7170.

5. Chang, W.Y., et al., *A Large Area Flexible Array Sensors Using Screen Printing Technology*. Journal of Display Technology, 2009. **5**(6): p. 178-183.

6. Cheng, S., et al., *Foldable and Stretchable Liquid Metal Planar Inverted Cone Antenna.* IEEE Transactions on Antennas and Propagation, 2009. **57**(12): p. 3765-3771.

7. Lee, G.-Y., *Multi-material direct printing by Pulsed-Nano Particle Deposition System (P-NPDS)*, in *School of Mechanical and Aerospace Engineering, Ph.D. Thesis*. 2013, Seoul National University.

8. Chun, D.M., et al., *Nano particle deposition system (NPDS) for ceramic and metal coating at room temperature and low vacuum condition*, in *Smart Manufacturing Application, ICSMA 2008. International Conference on. IEEE*. 2008. p. 383-386.

9. Akedo, J., *Room Temperature Impact Consolidation (RTIC) of Fine Ceramic Powder by Aerosol Deposition Method and Applications to Microdevices.* Journal of Thermal Spray Technology, 2008. **17**(2): p. 181-198.

10. Lee, G.Y., et al., *Aerodynamically focused nanoparticle (AFN) printing: novel direct printing technique of solvent-free and inorganic nanoparticles.* ACS applied materials & interfaces, 2014. **6**(19): p. 16466-71.

11. Chiolerio, A., et al., *Inkjet printing and low power laser annealing of silver nanoparticle traces for the realization of low resistivity lines for flexible electronics.* Microelectronic Engineering, 2011. **88**(8): p. 2481-2483.

12. Ahn, S.H., et al., *Laser-assisted nano particle deposition system and its application for dye sensitized solar cell fabrication.* CIRP Annals-Manufacturing Technology, 2012. **61**(1): p. 575-578.

13. Olakanmi, E.O. and M. Doyoyo, *Laser-Assisted Cold-Sprayed Corrosion- and Wear-Resistant Coatings: A Review.* Journal of Thermal Spray Technology, 2014. **23**(5): p. 765-785.

14. Chu, W.S., et al., *Hybrid manufacturing in micronano scale; A Review.* International journal of precision engineering and manufacturing-green technology, 2014. **1**(1): p. 75-92.

15. Akedo, J. and M. Lebedev, *Microstructure and Electrical Properties of Lead Zirconate Titanate (Pb(Zr52Ti48)O3) Thick Films Deposited by Aerosol Deposition Method.* Japanese journal of applied physics, 1999. **38**(9S): p. 5397.

16. Akedo, J., et al., *Jet molding system for realization of three-dimensional micro-structures.* Sensors and Actuators A: Physical, 1998. **69**(1): p. 106-112.

17. Akedo, J., *Aerosol deposition method (ADM): a novel method of PZT thick films producing for microactuators.* Recent Res. Develp. Mat. Sci., 2001. **2**: p. 51-77.

18. Hanft, D., et al., *An overview of the aerosol deposition method; process fundamentals and new trends in materials applications.* J. Ceram. Sci. Technol 2015. **6**(3): p. 147-182.

19. Lee, D.W., et al., *Growth Process of α-Al2O3 Ceramic Films on Metal Substrates Fabricated at Room Temperature by Aerosol Deposition.* Journal of the American Ceramic Society, 2011. **94**(9): p. 3131-3138.

20. Hoshina, T., et al., *Size effect of nanograined BaTiO3 ceramics fabricated by aerosol deposition method.* Japanese Journal of Applied Physics, 2010. **49**(9S): p. 09MC02.

21. Cho, S.H. and Y.J. Yoon, *Multi-layer TiO2 films prepared by aerosol deposition method for dye-sensitized solar cells.* Thin Solid Films, 2013. **547**: p. 91-94.

22. Papyrin, A., et al., *Cold spray technology*. 2006: Elsevier.

23. Stoltenhoff, T., Kreye, H. and Richter, H.J., *An analysis of the cold spray process and its coatings.* Journal of Thermal Spray Technology, 2002. **11**(4): p. 542-550.

24. Champagne, V.K., *The Cold Spray Materials Deposition Process: Fundamentals and Applications*. 2007: Elsevier.

25. Gärtner, F., et al., *The Cold Spray Process and Its Potential for Industrial Applications.* Journal of Thermal Spray Technology, 2006. **15**(2): p. 223-232.

26. Chun, D.M., et al., *Nano-particle deposition system (NPDS): Low energy solvent-free dry spray process for direct patterning of metals and ceramics at room temperature.* International Journal of Precision Engineering and Manufacturing, 2012. **13**(7): p. 1107-1112.

27. Chun, D.-M., *Development of nano particle deposition system (NPDS) for room temperature deposition of metals and ceramics and its applications*, in *School of Mechanical and Aerospace Engineering, Ph.D. Thesis*. 2010, Seoul National University. p. 133.

28. Kim, C.-S., *Nanoscale 3D Printing Process using Nano Particle Deposition System and Focused Ion Beam*, in *School of Mechanical and Aerospace Engineering, Ph.D. Thesis*. 2013, Seoul National University.

29. Chun, D.M., et al., *TiO2 coating on metal and polymer substrates by nano-particle deposition system (NPDS).* CIRP Annals-Manufacturing Technology, 2008. **57**(1): p. 551-554.

30. Song, W., et al., *Deposition of Al2O3 powders using nano-particle deposition system.* Surface Review and Letters, 2010. **17**(02): p. 189-193.

31. Song, W., et al., *Nanoparticle Deposition of Al2O3 Powders on Various Substrates.* Materials transactions, 2009. **50**(11): p. 2680-2684.

32. Jung, K., et al., *Nickel Line Patterning Using Silicon Supersonic Micronozzle Integrated with a Nanoparticle Deposition System.* Japanese Journal of Applied Physics, 2010. **49**(5S1): p. 05EC09.

33. Jung, K., et al., *Coating of Ni powders through micronozzle in a nano particle deposition system.* Metals and Materials International, 2010. **16**(3): p. 465-467.

34. Chun, D.M., et al., *Multilayer deposition of ceramic and metal at room temperature using nanoparticle deposition system (NPDS) and planarization process.* The International Journal of Advanced Manufacturing Technology, 2013. **72**(1-4): p. 41-46.

35. Chun, D.M. and S.H. Ahn, *Deposition mechanism of dry sprayed ceramic particles at room temperature using a nano-particle deposition system.* Acta Materialia, 2011. **59**(7): p. 2693-2703.

36. Jung, K., et al., *Computational Fluid Dynamics Analysis of Fabricated Micronozzle for Supersonic Particle Deposition.* Surface Review and Letters, 2010. **17**(01): p. 45-49.

37. Kim, M.S., et al., *Room temperature deposition of TiO2 using nano particle deposition system (NPDS): Application to dye-sensitized solar cell (DSSC).* International Journal of Precision Engineering and Manufacturing, 2011. **12**(4): p. 749-752.

38. Kim, M.S., et al., *Dry-Spray Deposition of TiO2 for a Flexible Dye-Sensitized Solar Cell (DSSC) Using a Nanoparticle Deposition System (NPDS)* Journal of nanoscience and nanotechnology 2012. **12**(4): p. 3384-3388.

39. Choi, D., et al., *Investigation of dry-deposited ion storage layers using various oxide particles to enhance electrochromic performance.* Solar Energy Materials and Solar Cells, 2018. **174**: p. 599-606.

40. Kim, H., et al., *Effect of particle size and amorphous phase on the electrochromic properties of kinetically deposited WO 3 films.* Solar Energy Materials and Solar Cells, 2018. **177**: p. 44-50.

41. Park, S.I., et al., *Low-cost fabrication of WO 3 films using a room temperature and low-vacuum air-spray based deposition system for inorganic electrochromic device applications.* Thin Solid Films, 2015. **589**: p. 412-418.

42. Park, S.I., et al., *A review on fabrication processes for electrochromic devices.* International Journal of Precision Engineering and Manufacturing-Green Technology, 2016. **3**(4): p. 397-421.

43. Choi, J.-O., *Development of hybrid process using laser and dry particle deposition system,* in *Department of Mechanical and Aerospace Engineering, Ph.D. Thesis*. 2016, Seoul National University.

44. Ahn, S.H., et al., *Effect of laser-excited ceramic nanoparticles on hardness and porosity of dry-sprayed coating.* CIRP Annals, 2017. **66**(1): p. 519-522.

45. Song, J.H., et al., *Controlled kinetic Monte Carlo simulation of laser improved nano particle deposition process.* Powder Technology, 2018. **325**: p. 651-658.

46. Shahzad, K., et al., *Additive manufacturing of zirconia parts by indirect selective laser sintering.* Journal of the European Ceramic Society, 2014. **34**(1): p. 81-89.

47. Booth, G.S., R.L. Jones, and P.L. Threadgill, *Recent development in welding technology*, in *16th International Offshore and Polar Engineering Conference*. 2006: San Francisco, California.

48. Griffith, M.L., et al. *Free form fabrication of metallic components using laser engineered net shaping (LENS)*. in *Solid Freeform Fabrication Proceedings*. 1996. Solid Freeform Fabrication Symposium, Austin.

49. Das, S., *Physical Aspects of Process Control in Selective Laser Sintering of Metals.* Advanced Engineering Materials, 2003. **5**(10): p. 701-711.

50. Gibson, I. and D. Shi, *Material properties and fabrication parameters in selective laser sintering process.* Rapid Prototyping Journal, 1997. **3**(4): p. 129-136.

51. Zeng, K., D. Pal, and B. Stucker. *A review of thermal analysis methods in Laser Sintering and Selective Laser Melting*. in *Proceedings of Solid Freeform Fabrication Symposium*. 2012. Austin, TX.

52. Morgan, R., et al., *Analysis of cold gas dynamically sprayed aluminium deposits.* Materials Letters, 2004. **58**(7-8): p. 1317-1320.

53. Bray, M., Cockburn, A. and O'Neill, W., *The laser-assisted cold spray process and deposit characterisation.* Surface and Coatings Technology, 2009. **203**(19): p. 2851-2857.

54. Bray, M., S. Celotto, and W. O'Neill. *Development of a laser assisted material spraying process*. in *Proceedings of the International Congress on Applications of Laser and Electro-Optics (ICALEO 06)*. 2006. Arizona, USA: LIA.

55. Koivuluoto, H., et al., *Structures and Properties of Laser-Assisted Cold-Sprayed Aluminum Coatings.* In Materials Science Forum, 2017. **879**: p. 987-989.

56. Peyre, P., et al., *Analytical and numerical modelling of the direct metal deposition laser process.* Journal of Physics D: Applied Physics, 2008. **41**(2): p. 025403.

57. Thompson, S.M., et al., *An overview of Direct Laser Deposition for additive manufacturing; Part I: Transport phenomena, modeling and diagnostics.* Additive Manufacturing, 2015. **8**: p. 36-62.

58. Pan, H. and F. Liou, *Numerical simulation of metallic powder flow in a coaxial nozzle for the laser aided deposition process.* Journal of Materials Processing Technology, 2005. **168**(2): p. 230-244.

59. Zekovic, S., R. Dwivedi, and R. Kovacevic, *Numerical simulation and experimental investigation of gas–powder flow from radially symmetrical nozzles in laser-based direct metal deposition.* International Journal of Machine Tools and Manufacture, 2007. **47**(1): p. 112-123.

60. Choi, J. and Y. Chang, *Characteristics of laser aided direct metal/material deposition process for tool steel.* International Journal of Machine Tools and Manufacture, 2005. **45**(4-5): p. 597-607.

61. Chung, J., et al., *Damage-free low temperature pulsed laser printing of gold nanoinks on polymers.* Journal of Heat Transfer, 2005. **127**(7): p. 724-732.

62. Bieri, N.R., et al., *An experimental investigation of microresistor laser printing with gold nanoparticle-laden inks.* Applied Physics A, 2005. **80**(7): p. 1485-1495.

63. Kim, M.K., et al., *Laser sintering of inkjet-printed silver nanoparticles on glass and PET substrates*, in *Nanotechnology (IEEE-NANO), 2010 10th IEEE Conference*. 2010, IEEE. p. 520-524.

64. Gao, M., et al., *The Effect of Deposition Patterns on the Deformation of Substrates During Direct Laser Fabrication.* Journal of Engineering Materials and Technology, 2013. **135**(3): p. 034502.

65. Dahneke, B., *The capture of aerosol particles by surfaces.* Journal of colloid and interface science, 1971. **37**(2): p. 342-353.

66. Rogers, L.N. and J. Reed, *The adhesion of particles undergoing an elastic-plastic impact with a surface.* Journal of Physics D: Applied Physics, 1984. **17**(4): p. 677.

67. Aleksandrov, V.M., I.G. Kadomtsev, and L.B. Tsaryuk, *Axisymmetric contact problems for elastoplastic bodies.* Trenie Iznos, 1984. **1**(1): p. 16-26.

68. Biryukov, D.G. and I.G. Kadomtsev, *Dynamic Elastoplastic Interaction between an Impactor and a Spherical Shell.* Journal of applied mechanics and technical physics, 2002. **43**(5): p. 777-781.

69. Qin, Z. and R.H. Pletcher, *Particle impact theory including surface asperity deformation and recovery.* Journal of Aerosol Science, 2011. **42**(12): p. 852-858.

70. Brach, R.M. and P.F. Dunn, *A Mathematical Model of the Impact and Adhesion of Microspheres.* Aerosol Science and Technology, 1992. **16**(1): p. 51-64.

71. Ogawa, H., *Molecular Dynamics Simulation on the Single Particle Impacts in the Aerosol Deposition Process.* Materials transactions, 2005. **46**(6): p. 1235-1239.

72. Ogawa, H., *Atomistic Simulation of the Aerosol Deposition Method with Zirconia Nanoparticles.* Materials transactions, 2006. **47**(8): p. 1945-1948.

73. Ogawa, H., *Molecular Dynamics Simulation on the Modification of Crystallographic Orientation in Fragmented Particles in the Aerosol-Deposition Process.* Materials transactions, 2007. **48**(8): p. 2067-2071.

74. Carrillo, J.M.Y., E. Raphael, and A.V. Dobrynin, *Adhesion of nanoparticles.* Langmuir, 2010. **26**(15): p. 12973-12979.

75. Wang, Y. and I. Horváth, *Computer-aided multi-scale materials and product design.* Computer-Aided Design, 2013. **45**(1): p. 1-3.

76. Gilmore, C.M. and J.A. Sprague, *Molecular-dynamics simulation of the energetic deposition of Ag thin films.* Physical Review B, 1991. **44**(16): p. 8950-8957.

77. Hassani, A., et al., *The influence of the surface orientation on the morphology during homoepitaxial growth of Nickel by molecular dynamics simulation.* Surface Review and Letters, 2017. **24**(02): p. 1750019.

78. Schneider, M., A. Rahman, and I.K. Schuller, *Role of relaxation in epitaxial growth: A molecular-dynamics study.* Physical review letters, 1985. **55**(6): p. 604-606.

79. Gawlinski, E.T. and J.D. Gunton, *Molecular-dynamics simulation of molecular-beam epitaxial growth of the silicon (100) surface.* Physical Review B, 1987. **36**(9): p. 4774-4781.

80. Kang, J.H., K.S. Kim, and K.W. Kim, *Molecular dynamics study on the effects of stamp shape, adhesive energy, and temperature on the nanoimprint lithography process.* Applied Surface Science, 2010. **257**(5): p. 1562-1572.

81. Min, K., et al., *Computational approaches for investigating interfacial adhesion phenomena of polyimide on silica glass.* Scientific Reports, 2017. **7**(1): p. 10475.

82. Akedo, J., *Aerosol Deposition of Ceramic Thick Films at Room Temperature: Densification Mechanism of Ceramic Layers.* Journal of the American Ceramic Society, 2006. **89**(6): p. 1834-1839.

83. Liau, L.C.K. and C.Y. Lin, *Vacancy defect distribution of colloidal particle deposition in a sedimentation process investigated using Kinetic Monte Carlo simulation.* Colloids and Surfaces A: Physicochemical and Engineering Aspects, 2011. **388**(1-3): p. 70-76.

84. Lam, P.M., S.J. Liu, and C.H. Woo, *Monte Carlo simulation of pulsed laser deposition.* Physical Review B, 2002. **66**(4): p. 045408.

85. Koparde, V.N. and P.T. Cummings, *Molecular dynamics simulation of titanium dioxide nanoparticle sintering.* The Journal of Physical Chemistry B, 2005. **109**(51): p. 24280-24287.

86. Hawa, T. and M.R. Zachariah, *Coalescence kinetics of bare and hydrogen-coated silicon nanoparticles: A molecular dynamics study.* Physical Review B, 2005. **71**(16): p. 165434.

87. Tsuruta, K., et al., *Early stages of sintering of silicon nitride nanoclusters: a molecular-dynamics study on parallel machines.* EPL (Europhysics Letters), 1996. **33**(6): p. 441.

88. Hawa, T. and M.R. Zachariah, *Molecular dynamics simulation and continuum modeling of straight-chain aggregate sintering: Development of a phenomenological scaling law.* Physical Review B, 2007. **76**(5): p. 054109.

89. HA, A., et al., *Molecular Dynamics Simulation of Sintering and Surface Premelting of Silver Nanoparticles.* Materials Transactions, 2013. **54**(6): p. 884-889.

90. Henz, B.J., T. Hawa, and M. Zachariah, *Molecular dynamics simulation of the kinetic sintering of Ni and Al nanoparticles.* Molecular Simulation, 2009. **35**(10-11): p. 804-811.

91. Song, P. and D. Wen, *Molecular dynamics simulation of the sintering of metallic nanoparticles.* Journal of Nanoparticle Research, 2010. **12**(3): p. 823-829.

92. Zeng, P., et al., *Nanoparticle sintering simulations 1*. Materials Science and Engineering: A, 1998. **252**(2): p. 301-306.

93. Ding, L., R.L. Davidchack, and J. Pan, *A molecular dynamics study of sintering between nanoparticles.* Computational Materials Science, 2009. **45**(2): p. 247-256.

94. Kadau, K., et al., *Molecular-Dynamics Study of Mechanical Deformation in Nano-Crystalline Aluminum.* Metallurgical and materials transactions A, 2004. **35**(9): p. 2719-2723.

95. Wolf, D., et al., *Deformation of nanocrystalline materials by molecular-dynamics simulation: relationship to experiments?* Acta Materialia, 2005. **53**(1): p. 1-40.

96. Pan, H., S.H. Ko, and C.P. Grigoropoulos, *The Solid-State Neck Growth Mechanisms in Low Energy Laser Sintering of Gold Nanoparticles: A Molecular Dynamics Simulation Study.* Journal of Heat Transfer, 2008. **130**(9): p. 092404.

97. Koparde, V.N. and P.T. Cummings, *Sintering of titanium dioxide nanoparticles: a comparison between molecular dynamics and phenomenological modeling.* Journal of Nanoparticle Research, 2008. **10**(7): p. 1169-1182.

98. Buesser, B., A.J. Grohn, and S.E. Pratsinis, *Sintering Rate and Mechanism of TiO2 Nanoparticles by Molecular Dynamics.* The Journal of Physical Chemistry C, 2011. **115**(22): p. 11030-11035.

99. Zhu, H., *Sintering processes of two nanoparticles: A study by molecular dynamics simulations.* Philosophical Magazine Letters, 1996. **73**(1): p. 27-33.

100. Raut, J.S., R.B. Bhagat, and K.A. Fichthorn, *Sintering of aluminum nanoparticles: a molecular dynamics study.* Nanostructured materials, 1998. **10**(5): p. 837-851.

101. Plimpton, S., et al., *Crossing the mesoscale no-man's land via parallel kinetic Monte Carlo*. 2009: Sandia Report

102. Tikare, V., E.A. Olevsky, and M.V. Braginsky, *Combined Macro-Meso Scale Modeling of Sintering. Part II: Mesoscale Simulations.* NATO SCIENCE SERIES SUB SERIES III COMPUTER AND SYSTEMS SCIENCES, 2001. **176**: p. 94-104.

103. Holm, E.A. and C.C. Battaile, *The computer simulation of microstructural evolution.* Journal of the Minerals, 2001. **53**(9): p. 20-23.

104. Olevsky, E.A., et al., *Modelling of anisotropic sintering in crystalline ceramics.* Philosophical Magazine, 2005. **85**(19): p. 2123-2146.

105. Tikare, V., et al., *Numerical simulation of anisotropic shrinkage in a 2D compact of elongated particles.* Journal of the American Ceramic Society, 2005. **88**(1): p. 59-65.

106. Tikare, V., et al., *Numerical simulation of microstructural evolution during sintering at the mesoscale in a 3D powder compact.* Computational Materials Science, 2010. **48**(2): p. 317-325.

107. Braginsky, M., V. Tikare, and E. Olevsky, *Numerical simulation of solid state sintering.* International journal of solids and structures, 2005. **42**(2): p. 621-636.

108. Tikare, V., M. Braginsky, and E.A. Olevsky, *Numerical Simulation of Solid-State Sintering: I, Sintering of Three Particles.* Journal of the American Ceramic Society, 2003. **86**(1): p. 49-53.

109. Molla, T.T., et al., *Multi-scale modeling of shape distortions during sintering of bi-layers.* Computational Materials Science, 2014. **88**: p. 28-36.

110. Garcia Cardona, C., V. Tikare, and S.J. Plimpton, *Parallel simulation of 3D sintering.* International Journal of Computational Materials Science and Surface Engineering, 2010. **4**(1): p. 37-54.

111. Hara, S., A. Ohi, and N. Shikazono, *Sintering analysis of sub-micron-sized nickel powders: Kinetic Monte Carlo simulation verified by FIB–SEM reconstruction.* Journal of Power Sources, 2015. **276**: p. 105-112.

112. Olevsky, E.A., V. Tikare, and T. Garino, *Multi-Scale Study of Sintering: A Review.* Journal of the American Ceramic Society, 2006. **89**(6): p. 1914-1922.

113. Bjørk, R., et al., *The sintering behavior of close-packed spheres.* Scripta Materialia, 2012. **67**(1): p. 81-84.

114. Bjørk, R., et al., *The effect of particle size distributions on the microstructural evolution during sintering.* Journal of the American Ceramic Society, 2013. **96**(1): p. 103-110.

115. Harding, J.H. and D.J. Harris, *Simulation of grain-boundary diffusion in ceramics by kinetic Monte Carlo.* Physical Review B, 2001. **63**(9): p. 094102.

116. Mukherjee, D., C.G. Sonwane, and M.R. Zachariah, *Kinetic Monte Carlo simulation of the effect of coalescence energy release on the size and shape evolution of nanoparticles grown as an aerosol.* The Journal of chemical physics, 2003. **119**(6): p. 3391-3404.

117. Westerhoff, F., R. Zinetullin, and D.E. Wolf, *Kinetic Monte-Carlo simulations of sintering.* arXiv preprint cond-mat, 2005. **0503336**.

118. Bjørk, R., et al., *Strain in the mesoscale kinetic Monte Carlo model for sintering.* Computational Materials Science, 2014. **82**: p. 293-297.

119. Lim, T.H., et al., *Real-time TEM and kinetic Monte Carlo studies of the coalescence of decahedral gold nanoparticles.* ACS nano, 2009. **3**(11): p. 3809-3813.

120. Lim, T.H., *Real-time TEM and kinetic Monte Carlo studies of the coalescence of decahedral gold nanoparticles.* ACS nano, 2009. **3**(11): p. 3809-3813.

121. Asp, K. and J. Ågren, *Phase-field simulation of sintering and related phenomena −A vacancy diffusion approach.* Acta Materialia, 2006. **54**(5): p. 1241-1248.

122. Wang, Y.U., *Computer modeling and simulation of solid-state sintering: A phase field approach.* Acta Materialia, 2006. **54**(4): p. 953-961.

123. Labudovic, M., D. Hu, and R. Kovacevic, *A three dimensional model for direct laser metal powder deposition and rapid prototyping.* Journal of materials science, 2003. **38**(1): p. 35-49.

124. Pinkerton, A.J. and L. Li, *An analytical model of energy distribution in laser direct metal deposition.* Proceedings of the Institution of Mechanical Engineers, Part B: Journal of Engineering Manufacture, 2004. **218**(4): p. 363-374.

125. Yoon, H.S., et al., *Direct printing of anisotropic wetting patterns using aerodynamically focused nanoparticle (AFN) printing.* Applied Surface Science, 2017. **396**: p. 1450-1457.

126. Chun, D.M., C.V. Ngo, and K.M. Lee, *Fast fabrication of superhydrophobic metallic surface using nanosecond laser texturing and low-temperature annealing.* CIRP Annals-Manufacturing Technology, 2016. **65**(1): p. 519-522.

127. Chun, D.M., et al., *Fabrication of transparent superhydrophobic surface on thermoplastic polymer using laser beam machining and compression molding for mass production.* CIRP Annals-Manufacturing Technology, 2014. **63**(1): p. 525-528.

128. Moradi, S., et al., *Femtosecond laser irradiation of metallic surfaces: effects of laser parameters on superhydrophobicity*. Nanotechnology, 2013. **24**(41): p. 415302.

129. Ta, D.V., et al., *Nanosecond laser textured superhydrophobic metallic surfaces and their chemical sensing applications.* Applied Surface Science, 2015. **357**: p. 248-254.

130. Yang, Y.L., et al., *Study on wetting properties of periodical nanopatterns by a combinative technique of photolithography and laser interference lithography.* Applied Surface Science, 2010. **256**(11): p. 3683-3687.

131. Simpson, J.T., S.R. Hunter, and T. Aytug, *Superhydrophobic materials and coatings: a review.* Reports on Progress in Physics, 2015. **78**(8): p. 086501.

132. Liu, Y., et al., *Fabrication of biomimetic super-hydrophobic surface on aluminum alloy.* Journal of materials science, 2014. **49**(4): p. 1624-1629.

133. Malshe, A., et al., *Bio-inspired functional surfaces for advanced applications.* CIRP Annals, 2013. **62**(2): p. 607-628.

134. Siegel, A.C., et al., *Foldable Printed Circuit Boards on Paper Substrates.* Advanced Functional Materials, 2010. **20**(1): p. 28-35.

135. Hwang, D.G. and M.D. Bartlett, *Tunable Mechanical Metamaterials through Hybrid Kirigami Structures.* Scientific Reports, 2018. **8**(1): p. 3378.

136. Gao, B., et al., *Bioinspired Kirigami Fish-Based Highly Stretched Wearable Biosensor for Human Biochemical-Physiological Hybrid Monitoring.* Advanced Materials Technologies, 2018. **3**(4): p. 1700308.

137. Amjadi, M., et al., *Stretchable, skin-mountable, and wearable strain sensors and their potential applications: a review.* Advanced Functional Materials, 2016. **26**(11): p. 1678-1698.

138. Palacio, M.L. and B. Bhushan, *Bioadhesion: a review of concepts and applications.* Phil. Trans. R. Soc. A, 2012. **370**(1967): p. 2321-47.

139. Bachmann, L. and M.Z. Denise, *Laser Physics and Laser Tissue Interaction*. Lasers in Dentistry, Practical text book. 2010. 1-14.

140. Brown, M.S. and C.B. Arnold, *Fundamentals of laser-material interaction and application to multiscale surface modification*. Laser precision microfabrication. 2010: Springer, Berlin, Heidelberg. 91-210.

141. Connelly, A. *BET surface area*. 2017 [cited 2019 1.22]; Laboratory Techniques, Science]. Available from: https://andyjconnelly.wordpress.com/2017/03/13/bet-surface-area/.

142. Bai, S., et al., *Laser-Assisted Reduction of Highly Conductive Circuits Based on Copper Nitrate for Flexible Printed Sensors.* Nano-Micro Letters, 2017. **9**(4): p. 42.

143. Pustovalov, V.K., *Modeling of the processes of laser-nanoparticle interaction taking into account temperature dependences of parameters.* Laser Physics, 2011. **21**(5): p. 906-912.

144. Manikandan, G., G. Murugan, and K. Raghukandan, *Effect of Grain Size upon the Thermal Behavior of Copper and Diamond Powders using Differential Scanning Calorimetry (DSC).* Indian Journal of Science and Technology, 2016. **9**(48).

145. Doremus, R., S.C. Kao, and R. Garcia, *Optical absorption of small copper particles and the optical properties of copper.* Applied optics, 1992. **31**(27): p. 5773-5778.

146. Mishin, Y., et al., *Structural stability and lattice defects in copper: Ab initio, tight-binding, and embedded-atom calculations.* Physical Review B, 2001. **63**(22): p. 224106.

147. *Application Data Sheet: Mechanical Properties of Copper and Copper Alloys at Low Temperatures, Copper Development Association Inc.* 2018 [cited 2018 11.15]; Available from: https://www.copper.org/resources/properties/144_8/.

148. Champion, Y., et al., *Near-perfect elastoplasticity in pure nanocrystalline copper.* Science, 2003. **300**(5617): p. 310-311.

149. Suryanarayana, C. and F.H. Froes, *The structure and mechanical properties of metallic nanocrystals.* Metallurgical Transactions A 1992. **23**(4): p. 1071-1081.

150. Zheng, B., et al., *Phase boundary effects on the mechanical deformation of core/shell Cu/Ag nanoparticles.* Journal of Materials Research, 2009. **24**(7): p. 2210-2214.

151. Carlton, C.E. and P.J. Ferreira, *What is behind the inverse Hall–Petch effect in nanocrystalline materials?* Acta Materialia 2007. **55**(11): p. 3749-3756.

152. Sanders, P.G., J.A. Eastman, and J.R. Weertman, *Elastic and tensile behavior of nanocrystalline copper and palladium.* Acta materialia, 1997. **45**(10): p. 4019-4025.

153. Gupta, S., K. Sharma, and N.S. Saxena, *Temperature Dependent Mechanical Analysis of Chalcogenide (CdS, ZnS) Coated PET Films.* ISRN Polymer Science, 2013.

154. Bitter, J.G.A., *A study of erosion phenomena part I.* Wear, 1963. **6**(1): p. 5-21.

155. Wang, Y., *Controlled kinetic Monte Carlo simulation for computer-aided nanomanufacturing.* Journal of Micro and Nano-Manufacturing, 2016. **4**(1): p. 011001.

156. Georgia Tech Multiscale Systems Engineering Repository, a.a. *https://github.com/GeorgiaTechMSSE*. [cited 2018.

157. Ortega, A., *The kinetics of solid‐state reactions toward consensus—Part I: Uncertainties, failures, and successes of conventional methods.* International Journal of Chemical Kinetics, 2001. **33**(6): p. 343-353.

158. Humphrey, W., A. Dalke, and K. Schulten, *VMD: visual molecular dynamics.* Journal of molecular graphics, 1996. **14**(1): p. 33-38.

159. Lophaven, S.N., H.B. Nielsen, and J. Søndergaard, *DACE-A Matlab Kriging toolbox*. IMM, Informatics and Mathematical Modelling. 2002, The Technical University of Denmark.